

# **Laser beam welding of high-alloyed aluminium-zinc alloys**

Vom Promotionsausschuss der  
Technischen Universität Hamburg-Harburg  
zur Erlangung des akademischen Grades

Doktor-Ingenieurin (Dr.-Ing.)

genehmigte Dissertation

von  
Josephin Enz

aus  
Berlin

2017

Erster Gutachter:  
Prof. Dr.-Ing. Norbert Huber,  
Institut für Werkstofforschung, Helmholtz-Zentrum Geesthacht

Zweiter Gutachter:  
Prof. Dr.-Ing. Klaus Dilger,  
Institut für Füge- und Schweißtechnik, Technische Universität Braunschweig

Datum der Disputation:  
09.11.2016

---

# Laser beam welding of high-alloyed aluminium-zinc alloys

**Josephin Enz**

Institute of Materials Research, Materials Mechanics, Joining and Assessment,  
Helmholtz-Zentrum Geesthacht,  
Max-Planck-Straße 1, 21502 Geesthacht, Germany.

## Abstract

The automotive industry is currently facing major challenges. In the course of the enacting of comprehensive environmental regulations for the fuel consumption and CO<sub>2</sub> emission of passenger vehicles in Europe and the world, the weight of future vehicles need to be considerably reduced. A weight reduction for automotive structures can be achieved by the substitution of heavy materials by lighter and stronger materials, the implementation of new designs and manufacturing technologies or ideally by a combination of both.

High-alloyed Al-Zn alloys are promising candidates for the use as structural light-weight materials for the automotive industry. This is mainly due to their very high strength-to-density ratio in comparison to conventionally used steels and aluminium alloys. Laser beam welding is an efficient method for producing joints with high weld quality and is established in the industry since many years. However, it is well known that aluminium alloys with a high Zn content or, more precisely, with a high Zn+Mg+Cu content are hard to fusion weld or even unweldable due to the formation of severe weld discontinuities. And currently, there is a lack of approaches for solving these weldability problems, which finally results in a disregard of these alloys by the automotive industry.

The present thesis aims at solving the laser weldability problems of these high-alloyed Al-Zn alloys. For this purpose a deep understanding of the theoretical fundamentals of laser weldability in terms of material properties and processes during laser beam welding was mandatory. By this means, typical reasons for weldability problems were derived and crucial influencing factors were identified. Based on the knowledge obtained, it was possible to develop two approaches for improving the laser weldability of high-alloyed Al-Zn alloys.

The first approach implies the use of an appropriate filler material - namely vanadium - additional to the conventional filler wire recommended for welding Al-Zn alloys. In this regard, vanadium enables the manipulation of the material properties of the weld metal. This first approach is feasible for different laser systems used for welding.

The second approach implies the use of a high-power fibre laser with a large beam diameter and a high beam quality. Here, the laser beam welding process itself is manipulated. This approach does not necessarily require a certain filler material.

The effectiveness of both developed approaches was verified by their application to diverse high-alloyed Al-Zn alloys. The assessment of the resulting weld properties finally also allowed assessing the capability of the approaches for industrial applications. Here, the second approach excels in its versatility and capability for large-scale productions.

---

# Laserstrahlschweißen von hochlegierten Aluminium-Zink-Legierungen

**Josephin Enz**

Institut für Werkstofforschung, Werkstoffmechanik, Fügen und Bewerten,  
Helmholtz-Zentrum Geesthacht,  
Max-Planck-Straße 1, 21502 Geesthacht, Deutschland.

## Zusammenfassung

Die Automobilindustrie steht derzeit vor großen Herausforderungen. Im Zuge der Erlassung umfangreicher Umweltschutzbestimmungen für Kraftstoffverbrauch und CO<sub>2</sub>-Ausstoß von Personenkraftfahrzeugen, sowohl in Europa wie auch weltweit, muss das Gewicht zukünftiger Fahrzeuge deutlich vermindert werden. Eine Gewichtsreduzierung von Fahrzeugstrukturen kann durch die Substitution schwerer Werkstoffe durch leichtere und höher festere, sowie die Einführung neuer Design- und Fertigungskonzepte - oder idealerweise eine Kombination der beiden - erreicht werden.

Hochlegierte Al-Zn-Legierungen sind aufgrund ihrer hohen Festigkeit und geringen Dichte im Vergleich zu herkömmlichen Al-Legierungen und Stahl vielversprechende Kandidaten für die Verwendung als leichter Strukturwerkstoff in der Automobilindustrie. Das Laserstrahlschweißen ist eine effiziente Methode zur Herstellung hochwertiger Schweißverbindungen und ist seit vielen Jahren in der Industrie etabliert. Al-Legierungen mit einem hohen Zinkgehalt bzw. mit einem hohen (Zn+Mg+Cu)-Gehalt gelten aufgrund der Bildung von schwerwiegenden Schweißfehlern im Allgemeinen als nur schwer schmelzschweißbar bzw. sogar unschweißbar. Derzeit gibt es keine Ansätze zur Lösung dieser Schweißbarkeitsprobleme, die letztendlich zu einer Missachtung dieser Legierung durch die Industrie führt.

Die vorliegende Arbeit hat zum Ziel, die Schweißbarkeitsprobleme dieser vielversprechenden hochlegierten Al-Zn-Legierungen zu lösen. Dazu war zunächst ein umfangreiches Verständnis über die theoretischen Grundlagen der Laserschweißbarkeit im Sinne von Materialeigenschaften und Prozessen während des Laserstrahlschweißens erforderlich. Somit konnten die Ursachen für typische Schweißprobleme ermittelt werden sowie die entscheidenden Einflussfaktoren identifiziert werden. Basierend auf diesem Wissen war es anschließend möglich, Lösungsansätze zur Verbesserung der Laserschweißbarkeit hochlegierter Al-Zn-Legierungen zu entwickeln.

Der erste Lösungsansatz beinhaltet die Verwendung eines geeigneten Schweißzusatzes - nämlich Vanadium - zusätzlich zum für Al-Zn-Legierungen empfohlenen konventionellen Zusatzdraht. Die Verwendung von Vanadium ermöglicht die Beeinflussung der Materialeigenschaften der Schmelze. Dieser erste Ansatz ist geeignet für verschiedene Laserschweißsysteme.

Der zweite Lösungsansatz beinhaltet die Verwendung eines Hochleistungs-Faserlasers mit großem Strahldurchmesser sowie hoher Strahlqualität. Hierbei wird der Laserschweißprozess selbst beeinflusst. Der zweite Ansatz erfordert keinen besonderen Schweißzusatzwerkstoff.

Die Leistungsfähigkeit beider Ansätze wurde durch ihre Anwendung an verschiedene hochlegierte Al-Zn-Legierungen überprüft. Die Beurteilung der resultierenden Schweißnahteigenschaften erlaubte schließlich eine Bewertung der Tauglichkeit für industrielle Anwendungen. Hierbei zeichnete sich insbesondere der zweite Lösungsansatz durch seine Vielseitigkeit und Tauglichkeit für eine Großproduktion aus.

# Contents

<b>1. Introduction</b>	<b>1</b>
1.1. Motivation . . . . .	1
1.2. Objectives . . . . .	3
1.3. Scientific approach . . . . .	3
1.4. Structure . . . . .	4
<b>2. Aluminium-zinc alloys</b>	<b>6</b>
2.1. Classification . . . . .	6
2.2. Chemical composition and heat treatment . . . . .	6
2.3. Mechanical properties . . . . .	8
2.4. Corrosion properties . . . . .	9
<b>3. Welding of aluminium-zinc alloys: State-of-the-art</b>	<b>11</b>
3.1. Conventional arc welding . . . . .	11
3.2. Solid-state welding . . . . .	11
3.3. Beam welding . . . . .	12
<b>4. Theoretical considerations of laser weldability</b>	<b>14</b>
4.1. Definition of laser weldability . . . . .	14
4.2. Melting, vaporisation and plasma formation . . . . .	17
4.3. Temperature distribution . . . . .	19
4.4. Pressure conditions in the keyhole . . . . .	21
4.5. Surface tension and viscosity . . . . .	24
4.6. Absorption . . . . .	26
4.7. Beam irradiance . . . . .	27
4.8. Solidification . . . . .	30
4.9. Porosity formation . . . . .	33
4.10. Weld imperfections . . . . .	34
<b>5. Approaches for improving the laser weldability</b>	<b>36</b>
5.1. Earlier approaches for different materials: State-of-the-art . . . . .	36
5.2. First approach: The use of an additional filler material . . . . .	38
5.3. Second approach: The use of an initially large beam diameter . . . . .	38
<b>6. Experimental methodology</b>	<b>41</b>
6.1. Materials . . . . .	41
6.2. Laser beam welding . . . . .	42
6.3. Experimental procedures . . . . .	45
6.3.1. Analysis of the welding behaviour . . . . .	45
6.3.2. Temperature measurement . . . . .	45
6.3.3. Hydrogen analysis . . . . .	46
6.3.4. Visual testing . . . . .	46
6.3.5. Radiographic testing . . . . .	46
6.3.6. Microstructural analysis . . . . .	47

6.3.7. Phase analysis . . . . .	47
6.3.8. Mechanical testing . . . . .	48
6.3.9. Corrosion testing . . . . .	49
<b>7. Proof of concept</b>	<b>50</b>
7.1. Base materials . . . . .	50
7.2. Worst case welding . . . . .	54
7.3. Variation welding . . . . .	61
7.4. Enhanced welding: First approach . . . . .	65
7.5. Enhanced welding: Second approach . . . . .	83
7.6. Relevance for the industry . . . . .	94
<b>8. Conclusions</b>	<b>97</b>
<b>9. Bibliography</b>	<b>99</b>
<b>A. Appendix</b>	<b>109</b>
A.1. Temperature distribution during laser beam welding . . . . .	109
A.2. Laser beam parameters . . . . .	110
A.3. Laser beam welding parameters . . . . .	111
A.4. JCPDS identification numbers . . . . .	111
A.5. Binary phase diagrams . . . . .	111

# List of symbols and abbreviations

$\alpha$	thermal diffusivity
$\Delta a$	crack length
$\Delta K$	stress intensity factor range
$\Delta N$	number of load cycles
$\epsilon_f$	strain to fracture
$\gamma$	surface tension
$\gamma_x$	activation coefficient of the alloying element $x$
$\lambda$	wavelength of the laser beam
$\mu$	viscosity
$\phi$	polar coordinate
$\rho$	density
$\Theta$	total angular spread
$A_l$	absorption factor of the laser
$A_v$	material coefficient
$b$	confocal parameter
$B_v$	material coefficient
$C$	material constant
$c_p$	specific heat capacity
$C_v$	material coefficient
$d$	beam diameter
$d_k$	keyhole diameter
$D_v$	material coefficient
$E$	line energy
$f + \Delta f$	focal length (distance between lens and beam waist)
$g$	gravitational acceleration
$I_{th\ k}$	threshold irradiance for keyhole welding

$I_{th\ m}$	threshold irradiance for melting/welding
$k$	thermal conductivity
$K_0$	Bessel function
$k_e$	extinction coefficient
$M$	atomic mass
$m$	material constant
$M^2$	beam quality factor
$n$	order of the Bessel function
$n_a$	absorption coefficient
$n_x$	mole fraction of the alloying element $x$
$p_a$	ambient pressure
$p_c$	capillary pressure
$p_d$	dynamic pressure
$p_h$	hydrostatic pressure
$p_k$	keyhole pressure
$P_l$	laser power
$p_v$	vapour pressure
$p_{x\ a}$	vapour pressure of the alloying element $x$ in the binary Al alloy
$p_{x\ p}$	vapour pressure of the pure metal $x$
$Q$	heat
$r$	polar coordinate
$R^2$	coefficient of determination
$r_k$	radius of the keyhole
$R_l$	reflection factor of the laser
$t$	time
$T_l$	transmission factor of the laser
$T_m$	melting temperature
$t_s$	sheet thickness
$T_v$	vaporisation temperature
$v$	welding speed

$v_w$	filler wire feed rate
$w$	mass fraction
$w(z)$	beam radius at the (focal) position $z$
$w_0$	beam radius at the waist
$x$	Cartesian coordinate
$y$	Cartesian coordinate
$z$	Cartesian coordinate
$z_{R0}$	Rayleigh length
Al	aluminium
Ar	argon
BM	base material
BSE	back-scattered electron
CO <sub>2</sub>	carbon dioxide
Cr	chromium
Cu	copper
D	design
DOE	diffractive optical element
EAA	European Aluminium Association
EBW	electron beam welding
EDX	energy-dispersive X-ray spectroscopy
FCP	fatigue crack propagation
Fe	iron
FL	fusion line
FSW	friction stir welding
FZ	fusion zone
GMA	gas metal arc welding
GP	Guinier-Preston zone
GTA	gas tungsten arc welding
HAZ	heat affected zone
He	helium

HV	Vickers hardness
HZG	Helmholtz Zentrum Geesthacht
ICCT	International Council on Clean Transportation
ISO	International Organization for Standardization
JCPDS	Joint Committee on Reference Powder Diffraction Standards
KLA	knife-line attack
LBW	laser beam welding
Li	lithium
M	material
Mg	magnesium
MIG	metal inert gas welding
Mn	manganese
n/a	not available
Nd:YAG	neodymium-doped yttrium aluminium garnet
NDT	non-destructive testing
P	process
PA	flat welding position
PC	horizontal welding position
PF	vertical up welding position
PFZ	precipitate free zone
PMZ	partially melted zone
PWA	post-weld ageing
PWHT	post-weld heat treatment
RRA	retrogression and re-ageing
RT	room temperature
SCC	stress corrosion cracking
SE	secondary electron
SEM	scanning electron microscopy
Si	silicon
sss	supersaturated solid solution

T-L	long transverse-longitudinal
Ti	titanium
TIG	tungsten inert gas welding
TMAZ	thermomechanical affected zone
TR	technical report
UTS	ultimate tensile strength
V	vanadium
w/	with
w/o	without
Y	yttrium
Yb	ytterbium
YS	yield strength
Zn	zinc



# 1. Introduction

## 1.1. Motivation

In the recent years the economic and political pressure on the automotive industry to reduce fuel consumptions and carbon dioxide ( $\text{CO}_2$ ) emissions of passenger vehicles constantly grew. For Europe - the front-runner in vehicle emission targets - a carbon dioxide reduction from 130 grams per kilometre in 2015 to 95 gram per kilometre in 2020 is currently sought by the International Council on Clean Transportation (ICCT), as depicted in Fig. 1.1 [1, 2]. On the other hand, the average weight of vehicles shows an increasing trend since the 1970s, despite its negative effect on the fuel consumption. This weight increase can be explained by the added safety and comfort equipment as well as the customer demand for higher performance levels and bigger cars [3, 4].

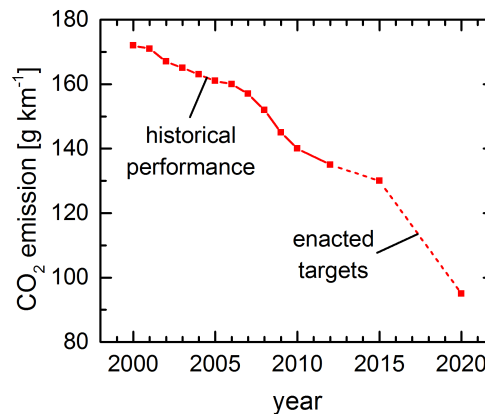


Figure 1.1.: European carbon dioxide regulations for passenger vehicles normalized to the New European Driving Cycle (according to ICCT [1]).

But in order to reduce the exhaust pipe carbon dioxide emissions a reduction of the vehicle weight is mandatory, since this provides one of the highest fuel saving potentials besides the use of novel propulsion concepts [2]. A weight reduction can be achieved by the substitution of heavier materials by lighter and stronger materials, the introduction of new design and manufacturing concepts or ideally by a combination of both [4].

Aluminium alloys are already substituting steel in many automotive applications. The main reason for this is their high strength-to-density ratio, besides their easy availability and machinability. Aluminium alloys possess a density, which is approximately one-third of that of steel, whereas their strength is maximal one-half of that of steel. Consequently, the specific strength of some aluminium alloys, such as Al-Zn alloys, can even exceed the values for ultra-high strength steels, as it can be seen in Fig. 1.2. The low ductility of the high-strength aluminium alloys is unfavourable for cold forming, but may be compensated by fast warm forming with only negligible effect on the strength of the final part, as described in the work of Uffelmann [5].

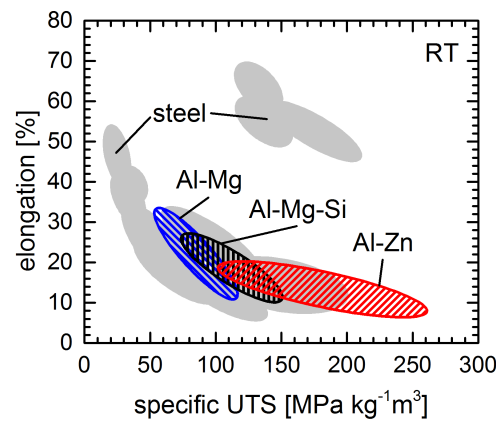


Figure 1.2.: Comparison of the elongation and specific ultimate tensile strength (at room temperature) of steels and Al alloys for the automotive industry (according to Nieuwerburgh [6]).

The average amount of aluminium in European passenger vehicles increased considerably in the last 25 years and is expected to even further increase in the next years [4, 7]. The development of the aluminium quantity in vehicles in Europe - the vanguard in this area - is depicted in Fig. 1.3 [8]. In this regard, aluminium is currently used in the car body, chassis, suspension and power train [8]. In the Al-maximised car study of Wallentowitz et al. [9] it was shown that an intensive use of aluminium in a compact car can lead to a weight reduction of up to 36 % (which corresponds in the present case a weight of 444 kilogrammes) without changing the functionality and performance of the vehicle. This was achieved in two steps: Primary weight savings, which imply the substitution of existing materials by aluminium alloys, and secondary weight savings, which imply additional downsizing of certain car components [3, 9]. In this regard, it is assumed that a weight reduction of 100 kilogrammes of an average European passenger vehicle lead to the saving of 0.35 litres of fuel per 100 kilometres and 9 grams of carbon dioxide per kilometre at the exhaust pipe of the car [8]. This means that the 'Alu-maximised car' would easily fulfil the European carbon dioxide emission standards of ICCT for 2020 [1].

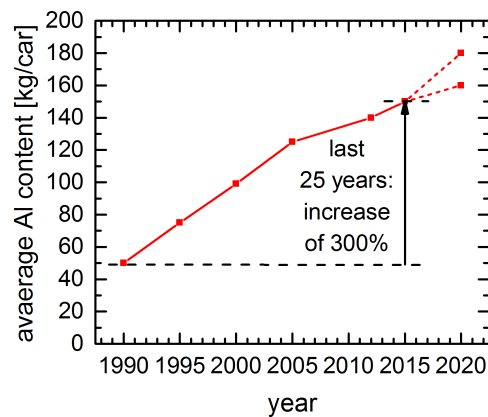


Figure 1.3.: Trend of the average amount of aluminium in European vehicles (according to EAA [4]).

Typically and extensively used aluminium alloys for automotive applications are mainly the non heat-treatable Al-Mg but also the heat-treatable Al-Mg-Si alloys [3, 5, 10]. These alloys feature a medium to high strength in combination with good formability as well as a good corrosion resistance and weldability. Although the heat-treatable Al-Zn alloys are accounted to the aluminium alloys with the highest strength, there is no widespread use of these alloys. The reason for this disregard of the industry lies in the fact that Al-Zn alloys exhibit distinct weldability problems such as the formation of porosity and hot cracks, which predominately arise during fusion welding of thin sheets and restrict the application possibilities [11–13].

From the middle of the 1980s to the beginning of the 1990s the first lasers, mainly CO<sub>2</sub> lasers followed by Nd:YAG lasers, were used for the welding of automotive applications in series production in Europe [14, 15]. Later, laser sources with higher laser powers and higher efficiencies, such as fibre lasers, were developed. And nowadays, laser beam welding belongs to the most efficient welding methods among the fusion welding processes. This can be explained by the high viable welding speeds, the beneficial depth-to-width ratio of the welds and the low heat exposure of the part. This is facilitated by high laser beam powers in combination with small laser beam dimensions, which result in a high energy density. Furthermore, laser beam welding also enables light-weight part designs due to the small weld dimensions and the low distortion as well as the improved accessibility for contact-free welding. This may lead to further weight reductions of the vehicles.

In summary it can be said that there is a large potential for reducing the weight of vehicles and thereby to meet the challenges of future car regarding fuel consumptions and emissions by the use of Al-Zn alloys as light-weight and high-strength materials in combination with laser beam welding as an efficient joining method for the manufacturing of automotive parts. But for exploiting this potential, the laser weldability problems of Al-Zn alloys have to be negotiated firstly. And finally, Al-Zn alloys may gain recognition by the industry as a promising structural material.

## 1.2. Objectives

The objectives of the thesis arise from the high potential of Al-Zn alloys due to their low density and high strength on the one hand and their severe weldability problems on the other hand, as mentioned earlier. Currently, there is a lack of appropriate approaches for solving these weldability problems, which precludes a widespread industrial application of Al-Zn alloys, although there is a considerable interest of the industry.

The first objective is to gain deeper understanding of the theoretical fundamentals of the existing laser weldability problems of Al-Zn alloys. In this regard, the material properties and processes during the laser beam welding are of great importance.

The second objective is the development of a laser welding process that significantly reduces or even avoids these weldability problems by using the obtained knowledge about the laser weldability. This may lead to a greater range of application.

Finally, the present thesis may also contribute to the development of further approaches for improving the weldability of Al-Zn alloys in the future.

## 1.3. Scientific approach

The scientific approach of the thesis to reach the target objectives is depicted in form of a schematic in Fig. 1.4.

At the beginning of the research the typical appearance of the laser weldability problems of Al-Zn alloys are identified. For this purpose, a 'worst-case' scenario welding is performed

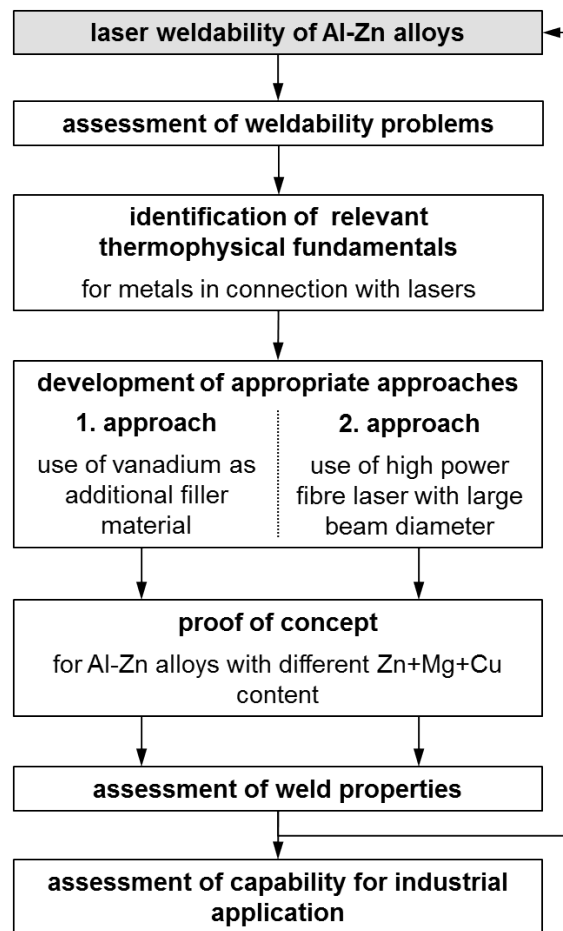


Figure 1.4.: Schematic diagram of the scientific approach of the present thesis.

on diverse Al-Zn alloys in order to determine the influence of the chemical composition on the weldability. The type of weld defects as well as their size and amount in the weld seam are determined. The theoretical fundamentals of laser weldability are investigated with the help of an extensive literature research and the computation of thermophysical properties. By this it is possible to identify the material properties and the processes during laser beam welding that are influencing the weldability. Thus, it is also possible to assign the weld discontinuities to the different causes. Subsequently, the obtained knowledge can be used to develop appropriate approaches to improve the laser weldability of Al-Zn alloys. These approaches can be based on either the manipulation of material properties (first approach) or the control of the laser welding process (second approach). The developed approaches are validated by their application to diverse high-alloyed Al-Zn alloys. By this it is possible to assess the effectiveness of each approach even for high-alloyed Al-Zn alloys. The properties of the resulting welds are determined, which finally allows to assess the capability of the developed approaches for an industrial application.

## 1.4. Structure

The structure of the present thesis is defined by the scientific approach for improving the laser weldability of Al-Zn alloys as outlined in Fig. 1.4. The thesis is complemented by an introduction to Al-Zn alloys.

Chapter 2 gives a general introduction to Al-Zn alloys and their properties. This includes the chemical composition and typical temper conditions as well as the resulting mechanical properties and corrosion resistance of these alloys.

In Chapter 3 the state-of-the-art of welding Al-Zn alloys, which are generally supposed to be hard-to-weld or even unweldable, is explained. In this context, the results for conventional arc welding as well as solid-state and beam welding procedures applied to diverse Al-Zn alloys are presented.

In Chapter 4 the fundamentals of laser weldability with regard to Al-Zn alloys are explained in detail, in order to gain full understanding of the material properties and processes during laser beam welding. For this purpose the most relevant thermophysical properties of metals are identified and calculated based on literature values. Since there is a lack of information for these kind of properties of complex alloys, only pure metals - as constituents of the alloys - are taken into consideration. The influence of each thermophysical parameter on the laser weldability is described in theory.

In Chapter 5 the obtained knowledge is used to develop two approaches for improving the laser weldability of Al-Zn alloys. The first approach exploits the manipulation of the material properties by the use of an additional filler material, whereas the second approach exploits the control of the laser welding process by the use of a high-power laser with an enlarged beam diameter. The functionality of each approach is described in detail. Moreover, the functionality of other earlier approaches for improving the laser weldability for different materials - introduced by other authors - can be also explained with the help of this knowledge.

Chapter 6 gives an overview of the experimental methodology. The materials as well as the laser beam welding equipment used in this study are presented. The characteristics of the different welding scenarios are described. Moreover, each of the experimental procedure used for the analysis of the welding behaviour and the determination of resulting joint properties are explained.

In Chapter 7 the feasibility of the two approaches is assessed. For this purpose, they are applied to diverse Al-Zn alloys with differing Zn+Mg+Cu content and compared to the results of the 'worst-case' scenario welding, which are conducted for comparison purposes. In this regard, the high-alloyed Al-Zn alloys are of particular interest. Moreover, the feasibility of improving the weldability by welding parameter variation is investigated. The results of each welding scenario are presented and discussed. Finally, an assessment of the capability of both approaches for eligible industrial applications is performed in this chapter.

In Chapter 8 the findings of the present thesis are summarized and the resulting conclusions are given.

## 2. Aluminium-zinc alloys

This chapter is dedicated to the principal properties of Al-Zn alloys. The influence of the chemical composition and heat treatment on properties is also explained. By this it is possible to identify the advantages and disadvantages of these aluminium alloys, which define but also limit possible applications.

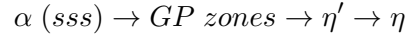
### 2.1. Classification

Al-Zn alloys - also called AA7xxx series alloys - belong to the system of age-hardenable aluminium alloys. This means that it is possible to change and improve the mechanical properties by a certain heat treatment. In general two sub-groups of Al-Zn alloys are distinguished: Cu-free and Cu-bearing Al-Zn alloys [16, 17], which basically differ in their mechanical properties, corrosion resistance and weldability [11]. Al-Zn alloys can be used for both casting and wrought products. But due to the limited castability, the bulk is generally available in form of wrought products [16, 17].

### 2.2. Chemical composition and heat treatment

The properties and consequently the use of aluminium alloys are generally defined by their chemical composition. Zinc is the main alloying element of Al-Zn alloy, but the alloying merely with zinc does not lead to a noticeable increase of strength. Only the combination of zinc and magnesium results in the formation of strengthening phases [11, 16, 18]. High Zn-to-Mg ratios result in a high strength and a good response to heat treatments, but show also high susceptibility to stress corrosion [17]. For this reason the amount of Zn+Mg is limited to 6-7 wt.% for Cu-free Al-Zn alloys. The alloying with copper enables the addition of higher amounts of Zn+Mg up to 9-10 wt.% so that even higher strength values can be achieved [16]. In this alloy system, zinc and magnesium are controlling the ageing process and copper is increasing the ageing rate by increasing the degree of supersaturation [18]. Copper also improves the resistance to stress corrosion. On the other hand, the alloying with copper results in a degradation of the general corrosion resistance as well as the weldability in terms of weld porosity and cracking [17, 18]. Thus, it can be concluded that the total amount of Zn+Mg+Cu defines the properties of Al-Zn alloys. Referring to Mondolfo [17], the highest strength is obtained for Al-Zn alloys with a Zn+Mg+Cu value above 10 wt.%. Currently, Al-Zn-Mg-Cu alloys with up to 12 wt.% zinc, 3.7 wt.% magnesium and 2.8 wt.% copper are commercially available [19]. Additional alloying with small amounts of chromium and manganese results in the highest strength available for aluminium alloys by preventing grain growth and recrystallization as well as by increasing the quench sensitivity [18, 20]. The effect of other minor alloying elements and impurities - such as silicon, iron and titanium - is described in detail in the work of Davis [18] and Mondolfo [17]. It is assumed that the amounts of these alloying elements are too small to have a noticeable effect [17]. The density of Al-Zn alloys is only reduced by magnesium. The alloying with all other common alloying elements leads to an increase of the density. Li, which is already used for reducing the density of other aluminium alloys, is up to now not used for Al-Zn alloys [19].

The properties of heat-treatable Al-Zn alloys can also be adjusted through a complex thermomechanical treatment, which implies a solution treatment, a quench to obtain a supersaturated solid solution and multi-step ageing treatment. The strongest contribution to the strength of aged Al-Zn-Mg-Cu alloys is achieved by precipitation hardening. The precipitation sequence, which dominates the strengthening of most of the Al-Zn alloys, is given by [21]:



In this regard, the most important phases - formed from the supersaturated solid solution  $\alpha$  (*sss*) - are the coherent Guinier-Preston (GP) zones, the semi-coherent  $\eta'$  phase and the incoherent  $\eta$  phase ( $\text{MgZn}_2$ ). Other sequences considering the  $T$  phase ( $\text{Mg}_3\text{Zn}_3\text{Al}_2$ ) and the  $S$  phase ( $\text{Al}_2\text{CuMg}$ ) are generally not contributing to the strengthening during typical heat treatments [11, 21–23]. The Al-Zn-Mg phase diagram assessed by Liang et al. [24] in Fig. 2.1 shows the concentration range of all relevant phases at 608 K. From this it becomes obvious that the  $\eta$  phase is mainly formed for high Zn-to-Mg ratios, whereas the  $T$  phase is formed for low Zn-to-Mg ratios.

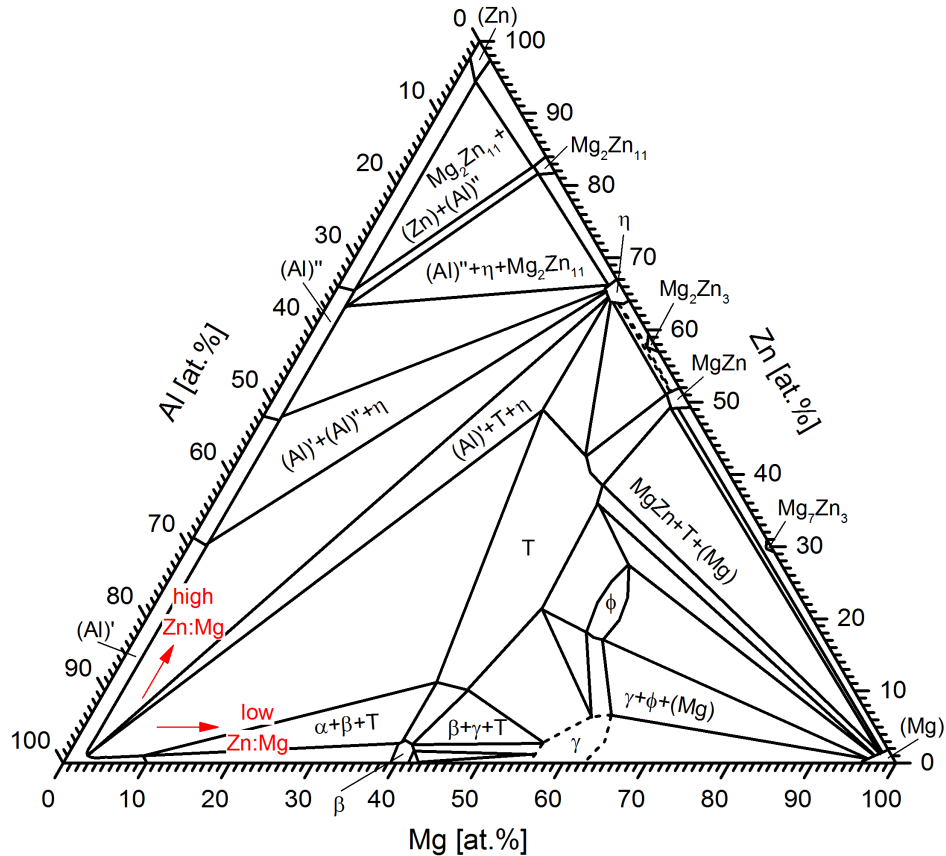


Figure 2.1.: Isotherm of the ternary Al-Zn-Mg phase diagram at 608 K (according to Liang et al. [24]).

High alloyed Al-Zn alloys are generally artificially aged either to a peak-aged, over-aged or under-aged condition [20]. The highest strength for Al-Zn alloys is obtained in the peak-aged (T6) condition. But this is always accompanied by low stress corrosion resistance, as shown in Fig. 2.2. For improving the corrosion resistance Al-Zn alloys are tempered to an over-aged (T7X) condition, which is always attended by a reduction of strength. The under-aged (T6X)

conditions show improved formability due to lower strength level. Here, the X stands for an additional temper digit that indicates subsequent temper processing for further influencing the resulting properties.

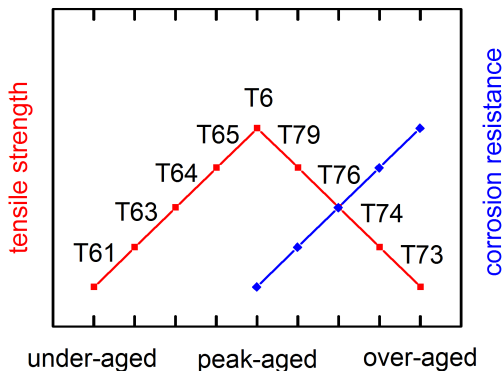


Figure 2.2.: Influence of the temper condition of high-strength Al-Zn alloys on the strength and corrosion behaviour (according to DIN EN 515 [25]).

Alternatively, retrogression and re-ageing (RRA) is used to reduce the stress corrosion susceptibility of Al-Zn alloys, while keeping the strength levels similar to the T6 condition. The first ageing step, corresponds to the T6 temper. The subsequent retrogression implies annealing for relatively short times followed by quenching. The second and final ageing step again corresponds to the T6 temper [26].

High alloyed Al-Zn alloys can also be strengthened by naturally ageing to a T3X or a T4X condition. But since these alloys hardly reach a stable condition at room temperature and exhibit significant changes in mechanical properties for numbers of years, these tempers are generally not applied [20, 27].

By post-weld heat treatment it is also possible to improve the strength of the heat affected zone (HAZ) of a weld. This implies either a complete post-weld solution heat treatment and ageing (PWHT) or post-weld ageing (PWA) only. The advantages of PWA are the lower temperatures and the absence of a quench, which may impose residual stresses and distortion. Al-Zn alloys also possess the ability to naturally age at room temperature in the HAZ, which require substantial longer ageing time of up to 14 days [28].

### 2.3. Mechanical properties

The group of Al-Zn alloys exhibits the highest strength of all aluminium alloys. As stated earlier, the mechanical properties are adjusted by the chemical composition in combination with thermalmechanical processing. In Table 2.1 the mechanical properties of wrought alloys with differing Zn+Mg+Cu content and cast alloys are specified for different temper conditions, according to the work of Mondolfo from 1976 [17]. The highest strength of up to 650 MPa is observed for alloys with a Zn+Mg+Cu content higher than 10 wt.% in an artificially aged condition, as explained in the previous section. Today, Al-Zn alloys with even better mechanical properties are known, such as C912 and AA7034. These two alloys can reach an ultimate tensile strength of 715 to 750 MPa, a yield strength of 689 to 730 MPa and a hardness of up to 226 HV in the peak-aged condition [29, 30]. The elongation to fracture is with 8 to 12 % as low as for the other high-strength Al-Zn alloys. For improving the formability

of these high-strength alloys either an initial under-aged temper condition or a warm forming process is strongly recommended [5]. The highest elongation to fracture  $\epsilon_f$  is observed for cast and low-alloyed wrought Al-Zn alloys in the as-cast or annealed condition.

Table 2.1.: Typical ranges for the mechanical properties of different Al-Zn alloys (according to Mondolfo [17]) with today's achievable values in parentheses [29, 30].

alloy	property	annealed or as-cast	naturally aged	artificially aged
wrought high strength (Zn+Mg+Cu $\geq$ 10 wt.%)	UTS [MPa]	250 – 350	450 – 550	550 – 650 (750)
	YS [MPa]	100 – 200	300 – 400	500 – 550 (730)
	$\epsilon_f$ [%]	10 – 20	10 – 15	5 – 10 (12)
	HV	50 – 60	120 – 130	150 – 170 (230)
wrought medium strength (Zn+Mg+Cu $\approx$ 7-9 wt.%)	UTS [MPa]	200 – 300	400 – 500	450 – 550
	YS [MPa]	80 – 150	250 – 350	300 – 400
	$\epsilon_f$ [%]	15 – 25	15 – 20	8 – 15
	HV	40 – 50	90 – 110	120 – 140
wrought low strength (Zn+Mg+Cu $\leq$ 6 wt.%)	UTS [MPa]	150 – 250	300 – 400	400 – 500
	YS [MPa]	60 – 120	200 – 300	300 – 400
	$\epsilon_f$ [%]	20 – 30	20 – 25	10 – 20
	HV	30 – 40	70 – 90	90 – 120
cast	UTS [MPa]	100 – 150	150 – 200	180 – 250
	YS [MPa]	50 – 100	80 – 150	120 – 200
	$\epsilon_f$ [%]	1 – 3	2 – 5	0 – 2
	HV	50 – 70	50 – 80	80 – 120

## 2.4. Corrosion properties

The corrosion resistance of Al-Zn alloys as well as the mechanical properties are dependent on their chemical composition and thermomechanical processing. The corrosion potential is of considerable importance, since corrosion is an electrochemical process with anodic and cathodic reactions (galvanic coupling). In this regard, the potential is influenced by the microstructural constituents in terms of composition of the solid solution and additional phases, spatial distribution and number density of additional phases [31, 32].

The addition of alloying elements, which are more noble and hence less active (cathodic) than aluminium, generally raise the corrosion potential, whereas more active (anodic) elements are decreasing the corrosion potential. The same is true for the formed precipitation phases. The Zn- and Mg-containing precipitates of Al-Zn alloys, the  $\eta$  and  $T$  phase, are anodic relative to the aluminium matrix. In contrast, the Cu-containing  $S$  phase is cathodic. The relation of the corrosion potential and the amount of alloying elements is shown in Fig. 2.3a. It can be concluded that large differences in the potential lead to localized corrosion. But also the size and distribution of the phases is influencing the corrosion behaviour. During the corrosion of small anodic and cathodic precipitates self-healing is prevailing. In contrast, coarse or agglomerated precipitates are deteriorating the corrosion resistance of an alloy. Hence, the influence of the thermomechanical processing can be explained. Over-ageing leads to a coarsening of the anodic  $\text{MgZn}_2$  precipitates and hence to a localised increase of the corrosion potential difference in case of Al-Zn-Mg-Cu alloys. This can be also observed in welded joints, where the heat affected zone undergoes a heat treatment during welding and becomes more anodic to the fusion zone and the unaffected base material (Fig. 2.3b). Thus, the

welding procedure that introduces the least heat input in the metal has the least influence on the microstructure and consequently results in the least degradation of the corrosion behaviour. Among the fusion welding processes the beam welding, such as laser beam welding and electron beam welding, is advantageous. The choice of an appropriate filler material may positively influence the corrosion behaviour. In this regard, the base and the filler material should have the same potential. If this is not practicable, the large base material should be anodic to the small weld metal [32]. Finally the corrosion resistance of the weld in terms of maximum temperature and cooling rate can also be improved by a post-weld heat treatment [28].

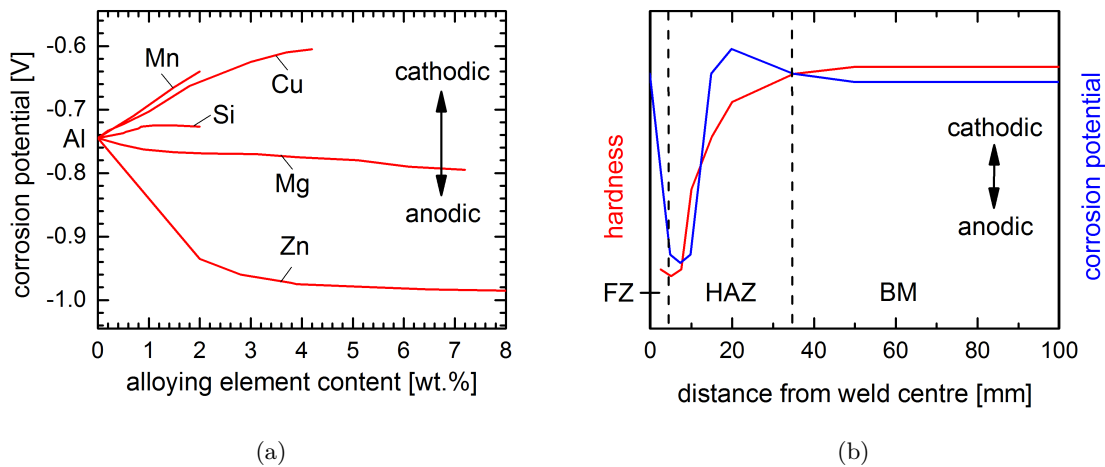


Figure 2.3.: Corrosion potential of binary Al alloys with different alloying element content (a) (according to Kaufman [33]) and an Al-Zn alloy welded with an Al-Mg filler wire (b) (according to Martukanitz [28]).

Al-Zn alloys containing no or only low amounts of copper as well as Al-Zn alloys in the peak-aged condition tend to be susceptible to stress corrosion cracking (SCC). SCC is a time-dependent intergranular fracture mode that requires the simultaneous presence of a susceptible alloy, a sufficient high tensile stress and a critical environment [31]. The two main theories for the mechanism of SCC are either cracking due to preferential corrosion along the grain boundaries by anodic dissolution or cracking along the grain boundaries enhanced by absorbed atomic hydrogen. But also the microstructure has an influence on the SCC behaviour. The short transverse direction of a rolled sheet shows a lower SCC resistance as the long transverse or longitudinal orientation [28, 31]. This means that for avoiding SCC no or only very little stress should be applied in this direction. As mentioned earlier, SCC susceptibility can be reduced by over-ageing or a corresponding PWHT, since critical tension loads due to residual stresses can arise during welding.

Another possibility to avoid corrosion of Al-Zn alloys could be the application of a protective layer. This and other corrosion prevention strategies are for example described in the work of Davis [32] and Scamans et al. [31].

## 3. Welding of aluminium-zinc alloys: State-of-the-art

In this chapter the state-of-the-art of welding Al-Zn alloys is surveyed. The complexities of welding these alloys are identified, particularly with regard to laser beam welding.

### 3.1. Conventional arc welding

Conventional arc welding processes, such as gas metal arc (GMA) welding and gas tungsten arc (GTA) welding, are well known and widely spread in the industry because of their high flexibility and easy handling. For both processes a filler wire is generally used. The resulting weld seams are characterized by a low aspect ratio (depth-to-width).

In the report of Romeyn [20] the possibilities of continuous and pulsed metal inert gas (MIG) welding as well as tungsten inert gas (TIG) welding of low-alloyed Cu-free and Cu-containing Al-Zn alloys, namely AA7019, AA7020 and AA7017, AA7039, were presented. Furthermore, the following welding problems typical for Al-Zn alloys were identified: hot cracking, joint softening mainly in the fusion zone (FZ) and to some extent in the heat affected zone (HAZ), poor weld zone ductility and susceptibility of the joint to stress corrosion cracking. Whereas weld seam porosity was not a severe problem.

The weldability of Cu-free and Cu-containing low-alloyed Al-Zn alloys, namely AA7020 and AA7022, by GMA welding using an Al-Mg filler wire was investigated by Ma [11]. It was stated that the Cu-containing AA7022 alloy showed a higher susceptibility to hot cracking in comparison to the Cu-free AA7020 alloy. In addition, the influence of the heat input on the hot cracking susceptibility was pointed out. A high heat input during welding as well as multi-pass welding generally results in increased hot cracking. Referring to Ma [11] the main reason for the formation of porosity during conventional welding is hydrogen dissolved in liquid aluminium. However, the amount of hydrogen can be significantly reduced by the removal of the surface oxide layer, a proper pre-cleaning and a proper shielding of the melt pool during welding.

Olabode [34] recently demonstrated the successful pulsed MIG welding of the low alloyed and medium strength Al-Zn alloys AA7020 and AA7025. The obtained joints showed no weld defects. The main advantage of using a pulsed MIG welding process was that there was no necessity for removing the oxide layer prior to welding, since it was decomposed during the welding process and does not cause porosity [35]. However, this welding process was not yet tested for high-alloyed Al-Zn alloys.

### 3.2. Solid-state welding

Friction stir welding (FSW) belongs to the solid-state welding processes, since no melting but a plasticizing of the material is required. This process is relatively novel and it is characterized by a low heat input, the absence of shielding gas and filler wire and an improved weldability of many hard-to-weld materials and material combinations. But on the other hand friction

stir welding also possesses a limited flexibility, a difficult handling and also a low aspect ratio of the resulting weld seams.

Rhodes et al. [36] and Mahoney et al. [37] described the friction stir welding of the Cu-containing Al-Zn alloy AA7075. The obtained weld seams showed no weld defects at all. A heat affected zone adjacent to the thermomechanical affected (TMAZ) zone was merely observed.

Dumont et al. [38] and Kamp et al. [39] successfully performed friction stir welding of the high-alloyed and Cu-containing Al-Zn alloy AA7449. And again, the absence of any weld defects can be explained by the prevention of melting during welding, since most of the weld defects are induced by melting of the material. Nevertheless, changes of the microstructure and the mechanical properties - due the exposure to temperature and high-level deformation - were observed in both studies. Here, the joint softening was considerable larger in TMAZ than in the weld nugget.

### 3.3. Beam welding

Beam welding processes, such as electron beam welding (EBW) and laser beam welding (LBW), are already well established in the industry. They are characterized by a low heat input (due to high energy densities in combination with high welding speeds), a high aspect ratio and a high flexibility (due to the contact-less welding). The handling of the LBW process is less complex, since no vacuum chamber as for EBW is required. However, laser beam welding is associated with process induced problems as for example keyhole instabilities during deep penetration welding, which do not occur during EBW, FSW and conventional welding.

Cu-free low alloyed and medium-strength Al-Zn alloys were successfully joined by auto-genous EBW under high vacuum. This was demonstrated for example by Çam et al. [40] and Deschamps et al. [41] for thin sheets using the low-alloyed AA7020. The obtained joints showed no considerable weld defects.

In the work of Arata et al. [42] the EBW of the high-strength Al-Zn alloy AA7075 under high vacuum is described. It was shown that very narrow and deep weld seams were obtained especially in comparison to other high-strength Al-Cu alloys. But the weld seams of AA7075 were always accompanied by a measurable loss of zinc and magnesium during welding, root porosity and a more irregular seam appearance. High welding speeds resulted in increased cracking in the fusion zone and the heat affected zone as well as in the formation of cold shuts. The best mechanical properties, comparable to that of the base material, were achieved for thick sections of up to 80 mm, whereas the welded thin sheets of 2 mm showed considerable worse properties.

Koy et al. [43] conducted EBW of the high-strength Al-Zn alloy AA7050 under medium ( $\approx 10^{-2}$  mbar) and high vacuum ( $\approx 10^{-4}$  mbar). It was shown that the vaporisation rate during welding of this alloy decreases with increasing sheet thickness. In this context, no difference between medium and high vacuum was detected. Only the outer weld appearance slightly deteriorates for the medium vacuum, whereas the weld seam dimensions seemed to remain constant [44]. In this regard, the Aluminium Automotive Manual of the European Aluminium Association (EAA) [45] recommends non-vacuum welding for the joining of thin sheets.

Allen et al. [46] performed autogenous laser beam welding and hybrid laser-MIG welding - using an Al-Mg filler wire - of an unnamed Al-Zn alloy. For this purpose two different laser sources (namely Nd:YAG and fibre laser) with differing power levels and beam diameters were used. Acceptable weld qualities were mainly achieved for the hybrid laser-MIG welded joints. In case of the autogenous laser welding, slightly better weld qualities were obtained by fibre

laser welding with high power levels and larger beam diameters. But since the exact chemical composition of the used Al-Zn alloy was not specified, the functionality of the approach for high-alloyed and Cu-containing Al-Zn alloys is not yet proven. The absence of hot cracks in the autogenously laser welded joints suggests that the used alloy belongs to the weldable low-alloyed Al-Zn alloys.

In the work of Katayama et al. [47] the high-power fibre laser welding of different aluminium alloys, including a low-alloyed Al-Zn alloy, was investigated. It was stated that those aluminium alloys containing zinc or magnesium resulted in deeper penetrations but also in an increased amount of weld porosity. An improvement of the weld quality - in terms of porosity, undercut and weld seam appearance - was only achieved by adjusting the incident beam angle as well as the shielding gas type and supply.

Verhaeghe [12] used a high-power fibre laser for the autogenous welding of thick sections of the Cu-containing Al-Zn alloy AA7150. In addition, hybrid fibre laser-MIG welding - using an Al-Mg filler wire - was conducted. It was shown that no defect free joints were achieved in the flat (PA) welding position - mainly because of severe burn-through. Solely in the horizontal (PC) and the vertical up (PF) position acceptable weld qualities were achieved. The different weld positions are depicted in Fig. 3.1. The influence of the laser beam size and the welding speed was also investigated. Finally, higher weld qualities were achieved for hybrid laser-MIG welding, large beam diameters (600  $\mu\text{m}$ ) and low welding speeds. Surprisingly no hot cracking - neither for autogenous laser welding nor for hybrid laser-MIG welding - was observed in the weld seams of this alloy, although the copper content of the used alloy is within the critical range for hot cracking. However, the approach was not tested on high-alloyed Al-Zn alloys.

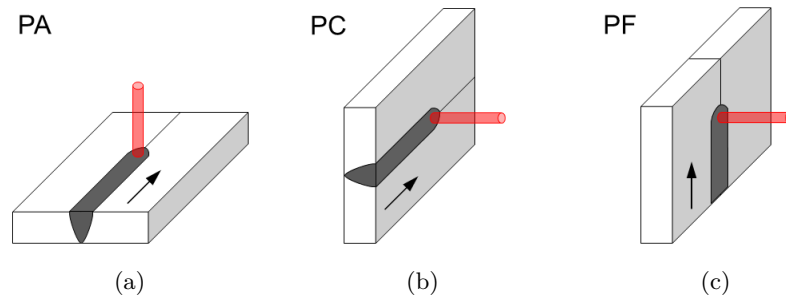


Figure 3.1.: Different weld positions for the butt joint welding: flat (a), horizontal (b) and vertical up (c).

Likewise, in the recent work of Zhang et al. [48] a fibre laser was used for the autogenous welding of a new high-alloyed, Cu-containing Al-Zn alloy. In spite of a welding parameter optimization, the resulting joints were characterized by a non-uniform outer appearance and an existing but reduced weld porosity. But since the used laser optical system was not described in detail, a repetition of these results is impossible.

In summary, the successful laser beam welding of high-alloyed and hard-to-weld Al-Zn alloys is so far not completely accomplished due to difficulties arising from the process-material-interactions. The amount of literature concerning this topic is also very limited. Solely Verhaeghe [12] and Zhang et al. [48] showed first approaches for overcoming the laser weldability problems of Al-Zn alloys. Furthermore, there is a lack of knowledge concerning reasons for the observed laser weldability problems of Al-Zn alloys.

The present thesis attempts to expand this state-of-the-art by identifying the theoretical fundamentals of laser weldability and introducing new approaches for solving these laser weldability problems of high-strength Al-Zn alloys.

## 4. Theoretical considerations of laser weldability

For improving the laser weldability of high-alloyed Al-Zn alloys and overcoming their weldability problems, as mentioned in the previous chapter, a full understanding of the material properties and processes during laser beam welding is required.

This chapter gives a brief introduction on the laser weldability and its main influencing factors. For this purpose the chemical and physical fundamentals of laser beam welding of metallic materials are identified and explained in detail relating to the high-alloyed Al-Zn alloys used in this study.

### 4.1. Definition of laser weldability

In general and referring to the technical report ISO/TR:581 [49], the weldability of a component consisting of a metallic material is defined as the ability to obtain metallic continuity by a given welding process using a suitable welding procedure. Hence, the weldability is influenced by three factors, namely material, design and production. Furthermore, the weldability is classified into three types, namely metallurgical, constructional and operative weldability, as indicated in Fig. 4.1.

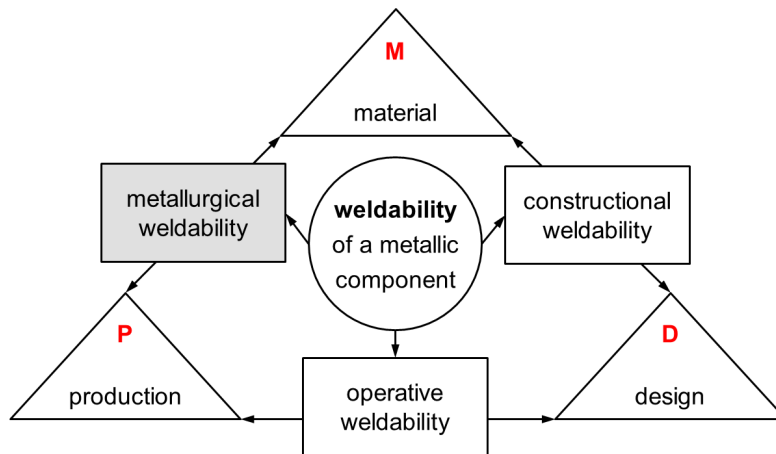


Figure 4.1.: The three main influencing factors of weldability and the classification of weldability types (according to ISO/TR:581 [49]).

Here, the interaction of material and procedure in Fig. 4.1 is called metallurgical weldability. Referring to ISO/TR 581 [49]: 'A material possesses metallurgical weldability if, in the course of the procedure adopted, the chemical, metallurgical and physical properties inherent in the material allow a weld to be made which satisfies the requirements of the application'. This means that the term (metallurgical) weldability cannot be generalized for each material or welding process. In the same technical report [49] it is also mentioned: 'The less the factors governed by the material have to be taken into account when determining the welding

procedure for a given construction, the better is the metallurgical weldability of a material within a material group'. This implies that the used welding process parameters should play as far as possible a subordinated role.

In the following, the term 'weldability' will be used in the sense of 'metallurgical weldability' of a material and the term 'laser weldability' will be used as 'metallurgical weldability' in connection with the procedure of 'laser beam welding'. The 'constructional weldability' (incorporating the design properties mainly influenced by the material) and 'operative weldability' (incorporating the production properties mainly influenced by the design) are not considered in this study.

In the work of Mondolfo [17] it was stated that the total amount of Zn+Mg+Cu is a feasible indicator for the weldability of Al-Zn alloys. All three of these elements are the main alloying elements of Al-Zn alloys, which are mainly defining their properties, as it was indicated in Table 2.1 in Section 2.3. Al-Zn alloys with a high total amount of Zn+Mg+Cu (above 9wt.%) will exhibit very high strength but only inferior weldability. In contrast, Al-Zn alloys with a total amount of Zn+Mg+Cu of 6 – 8wt.% will still exhibit high strength, but the weldability will be already improved. And a total below 6wt.% will result in reduced strength and further improved weldability. Additionally, the Zn-to-Mg ratio can also be taken into consideration for the assessment of weldability of Al-Zn alloys. In this connection, Al-Zn alloys with a total below 8wt.% show good weldability, especially if they are Cu-free and the Zn-to-Mg ratio is low [17]. From these findings it can be concluded that the weldability of Al-Zn alloys is particularly deteriorated by a high zinc content.

Lancaster [50], Beyer [51] and Kannatey-Asibu [52] studied the physical fundamentals of the processes during laser beam welding of metallic materials. The knowledge obtained in this study can be used for explaining the laser weldability of a material.

Sakamoto et al. [53], Hügel [54], Rapp et al. [55, 56] and Rapp [57] disclosed the relationship between threshold irradiances and the properties of aluminium alloys and the influences on the laser weldability. Later Leong et al. [58, 59] developed a model for the threshold irradiance for melting a metal with a focused laser beam moving with a constant velocity. From this model it became apparent that the laser weldability of a metallic material strongly depends on its thermophysical properties (in connection with the used laser type).

The relevant thermophysical properties of selected metals are specified in Table 4.1. Their influence on the laser weldability as well as their mutual interaction are explicated in detail in the following sections. The significant differences of the thermophysical parameters between the different metals, which are in part also the main alloying elements of high-alloyed Al-Zn alloys, are in evidence. This is a first indication for a differing laser beam welding behaviour of the pure metals. With the help of these information it is finally also possible to deduce the laser beam welding behaviour of high-alloyed Al-Zn alloys.

For the sake of completeness it has to be mentioned that numerous factors are affecting the weldability of a material. A selection of the most important influencing factors are summarized in the Ishikawa diagram (a cause-and-effect diagram) in Fig. 4.2. Four main groups can be classified: the material, the laser, the process and the environment. The elements of these groups may also interact. But, as already stated in the previous literature review, the most important factors on laser weldability seem to be the material specific thermophysical properties defining the laser-material interaction and the welding behaviour.

Table 4.1.: Thermophysical properties of different pure metals (according to Ho et al. [60], Alcock et al. [61], Leong et al. [59], Paradis et al. [62], Okada et al. [63] and Haynes [64]).

<b>thermophysical parameter</b>	<b>Al</b>	<b>Zn</b>	<b>Mg</b>	<b>Cu</b>	<b>V</b>	<b>Y</b>
melting temperature $T_m$ [K]	933	693	923	1357	2170	1799
vaporisation temperature $T_v$ [K]	2743	1180	1383	2868	3680	3203
vaporisation-melting ratio $T_v/T_m$ [-]	2.93	1.7	1.5	2.11	1.69	1.78
density $\rho$ [ $10^3 \text{ kg m}^{-3}$ ] of solid at 293 K	2.70	7.14	1.74	8.92	5.62	4.47
liquid at $T_m$	2.38	6.58	1.59	8.00	5.36	4.15
vapour pressure $p_v$ [Pa] at $T_m$	$10^{-6}$	23	360	$4.3 \cdot 10^{-2}$	$3.3 \cdot 10^{-3}$	0.32
1000 K	$12 \cdot 10^{-6}$	$12 \cdot 10^3$	1360	$1.5 \cdot 10^{-6}$	0	$5.6 \cdot 10^{-7}$
2000 K	900			380	$3.1 \cdot 10^{-4}$	4.1
3000 K					6.5	
viscosity $\mu$ [mPa s] at $T_m$	2.0	3.5	1.25	4.34	4.5	3.5
surface tension $\gamma$ [ $\text{Nm}^{-1}$ ] at $T_m$	0.91	0.78	0.56	1.30	1.95	0.87
thermal conductivity $k$ [ $\text{W m}^{-1} \text{K}^{-1}$ ] of solid at $T_m$	210	9	130	330	50	25
thermal diffusivity $\alpha$ [ $\text{cm}^2 \text{s}^{-1}$ ] of solid at $T_m$	0.68	0.32	0.65	0.79	0.11	0.11
absorption $A_l$ [%] at $T_m$ or 300 K* for						
1.06 $\mu\text{m}$ (Nd:YAG)	11	42	n/a	1.3*	45	n/a
10.6 $\mu\text{m}$ ( $\text{CO}_2$ )	3	10	3	5	5	n/a
threshold irradiance $I_{th}$ [ $\text{MWcm}^{-2}$ ] for						
Nd:YAG	0.42	0.0032	n/a	n/a	0.099	n/a
$\text{CO}_2$	1.5	0.016	0.95	2.4	0.89	n/a
with $d = 600 \mu\text{m}$ and $v = 4800 \text{ mm/min}$						

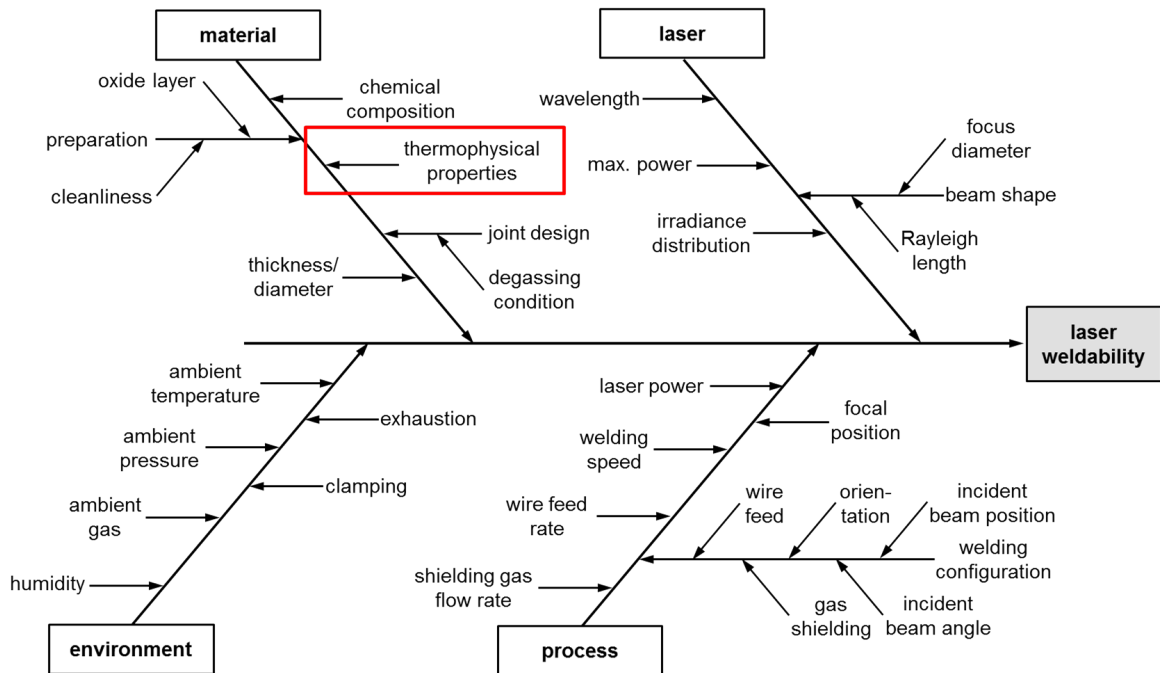


Figure 4.2.: Ishikawa diagram for the laser weldability.

## 4.2. Melting, vaporisation and plasma formation

Laser beam welding belongs to the fusion welding processes and thus, the melting of metallic material is obligatory for producing a welded joint. For the heat conduction laser welding - generally resulting in a relatively low penetration depth and a wide weld seam width - the local melting of the material is sufficient. However, for the deep penetration laser welding a local vaporisation of the material is required in order to form the keyhole. Without a doubt, the vaporisation is always accompanied by the limited melting of the surrounding material of the keyhole. By this, weld seams with a high depth-to-width ratio can be produced. A certain amount of melted material is always necessary to enable the joining of the sheets and to avoid cutting.

Typical melting and vaporisation temperatures of different pure metals are shown in Fig. 4.3. These metals are also typical alloying elements for aluminium alloys. It can be seen that aluminium belongs to the metals with a very low melting and vaporisation temperature. Only zinc and magnesium, which are the main alloying elements of Al-Zn alloys, have a lower melting and vaporisation temperature. But since only rarely pure metals are used in the industry, the influence of the chemical composition of the alloys has to be considered.

In Fig. 4.4a the influence of the alloying element content of binary aluminium alloys on the vaporisation temperature is shown [57]. With increasing amount of the volatile elements zinc and magnesium the vaporisation temperature is significantly decreased. For example, the addition of 10wt.% zinc to an aluminium alloy will result in a reduction of the vaporisation temperature of more than 1000K. This means that less heat is required for the formation a keyhole. In contrast, the effect of the alloying element copper on the vaporisation temperature of aluminium alloys is insignificant. Transition metals, such as vanadium, titanium, iron and yttrium, exhibit very high melting and vaporisation temperatures [65].

The vaporisation of material not only helps to form the keyhole, but also leads to a loss of the volatile elements during laser welding in the keyhole mode. The loss of elements can be

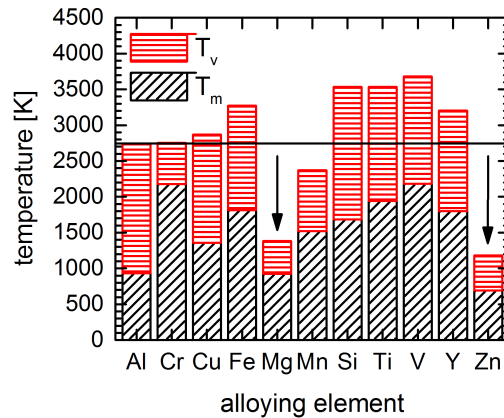


Figure 4.3.: Melting and vaporisation temperatures of different pure metals.

quantified by the vaporisation rate of the aluminium alloy during welding. This is illustrated in Fig. 4.4b [57]. It becomes apparent that in particular the content of zinc of a binary aluminium alloy has a major influence on the vaporisation rate, whereas magnesium and copper barely influence the vaporisation rate. As a result, fine particles - originating from the vaporisation - condensate on the work piece surface in form of a deposit [59]. This loss of elements may also be measurable in the chemical composition of the resulting weld seam.

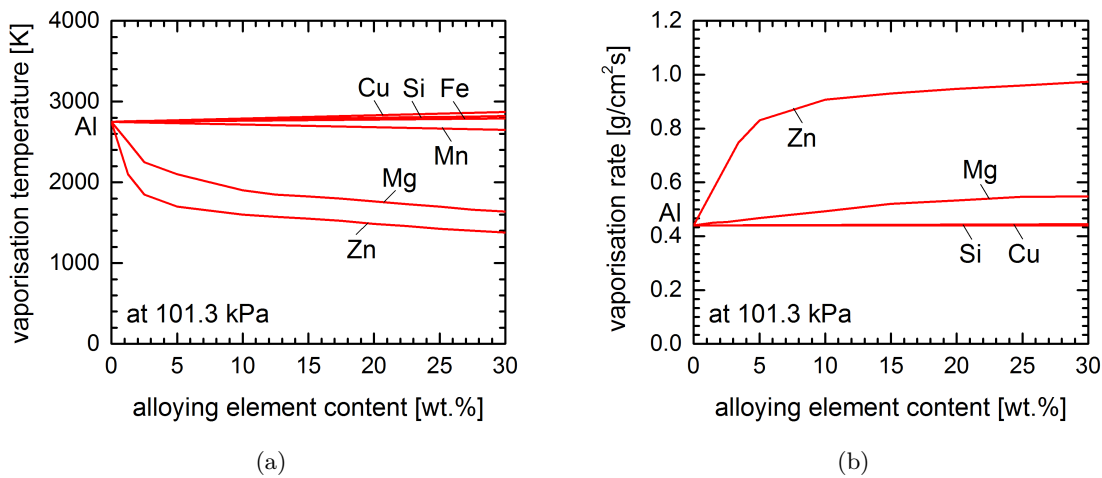


Figure 4.4.: Effect of the alloying element content of binary Al alloys on the vaporisation temperature (a) and the vaporisation rate (b) (according to Rapp et al. [57]).

Another disadvantageous effect is the occurrence of irregular vaporisation due to the depletion of the volatile elements zinc and magnesium on the keyhole surface, which generally leads to a temporary vapour pressure drop and hence to the collapse of the keyhole. These fluctuations of the keyhole become more distinctive for high vaporisations rates and small keyhole dimensions [12]. The influence of the pressure in the keyhole will be explained in Section 4.4.

Koy et al. [43] discovered a dependency of the vaporisation rate during beam welding on the sheet thickness. With increasing sheet thickness the tendency for vaporisation decreases and hence the weldability is slightly improved. The reason for this lies in the fact that thicker sheets can conduct heat more rapidly than thinner sheets.

In the work of Dausinger [66] it was asserted that not only the temperatures but also the ratio of vaporisation temperature to melting temperature is sufficient indicator for the resulting weld seam width (Table 4.1). The higher this ratio is, the larger is the resulting weld seam width [56, 66]. Further details of the derivation of this relation can be found in the work of Dausinger [66].

In addition, Sakomoto et al. [53], Dausinger [66] and Rapp et al. [56] showed that a lowered vaporisation temperature leads to a reduction of the threshold irradiance for achieving deep penetration melting, because the keyhole is formed more easily, as described in Section 4.7.

Rapp [57] disclosed the relationship between vaporisation rate and the tendency for spatter during laser beam welding. The higher the total vaporisation rate of a material during welding is, the higher is also the amount of spatter. Finally it can be concluded that the tendency for spatter strongly depends on the chemical composition and in particular on the zinc content of the aluminium alloy, as also further described in Section 4.5. Further details of the derivation of this relation are also described in the work of Rapp [57].

As a consequence of high energies during laser beam welding and hence the heating to temperatures above the vaporisation temperature, the formed vapour is partially ionized so that a laser-induced plasma is formed. This plasma can be observed during welding in form of a plume above the keyhole.

In the work of Arata et al. [67], Beyer [51] and Gao et al. [68] it was pointed out that strongly ionized plasma can lead to a partial shielding of the laser beam during welding and hence also to process instabilities - such as the collapsing of the keyhole. This strongly ionized plasma arises, when very high energies are applied to metals with low vaporisation temperatures and small ionization potentials, as in case of zinc and magnesium. Below the material-specific threshold energy the plasma is only weakly ionized and metal vapour dominated [68]. In this case, the plasma shielding effect is less distinctive.

The use of shielding gas, such as argon or helium, can suppress the negative effect of plasma by blowing it away from the keyhole, as shown by Kannatey-Asibu et al. [52] and Wang et al. [69]. Furthermore, helium possesses a higher ionisation potential, which impedes the excessive formation of plasma during laser beam welding. Alternatively, Luo et al. [70] demonstrated that the laser beam welding under sub-atmospheric pressure or vacuum leads to an even better suppression of the plasma plume. The type of laser - with a specific wavelength - used for welding has also an influence on the plasma shielding behaviour. CO<sub>2</sub> lasers with a wavelength of 10.6  $\mu\text{m}$  tend to be more affected by plasma absorption as for example Nd:YAG and fibre lasers with a shorter wavelength [51]. But depending on the used welding parameter even these lasers can be affected by plasma shielding if the energies are high enough [68].

### 4.3. Temperature distribution

Regarding the temperature distribution during laser beam welding it can be seen that the thermal conductivity and diffusivity of a metal are also influencing the laser beam welding behaviour. The temperature distribution in the joint during welding can either be measured or easily calculated e.g. by the use of the model of a moving line source. This model is described in detail in the Appendix A.1 of the thesis and in the work of Beyer [51].

The results for pure aluminium, which exhibits a very high thermal conductivity and diffusivity, and pure vanadium, which in contrast exhibits a low thermal conductivity and diffusivity, are shown in Fig. 4.5. The differences between both metals are considerable. The temperature field of aluminium is very broad and the peak temperature is low, whereas for vanadium the opposite is true. This means that for aluminium the resulting weld seam (fusion zone and heat affected zone) will be wider, but the keyhole opening will be more narrow.

Further, it can be concluded that the wider the keyhole opening is the better the degassing conditions will be and hence better weld qualities will result.

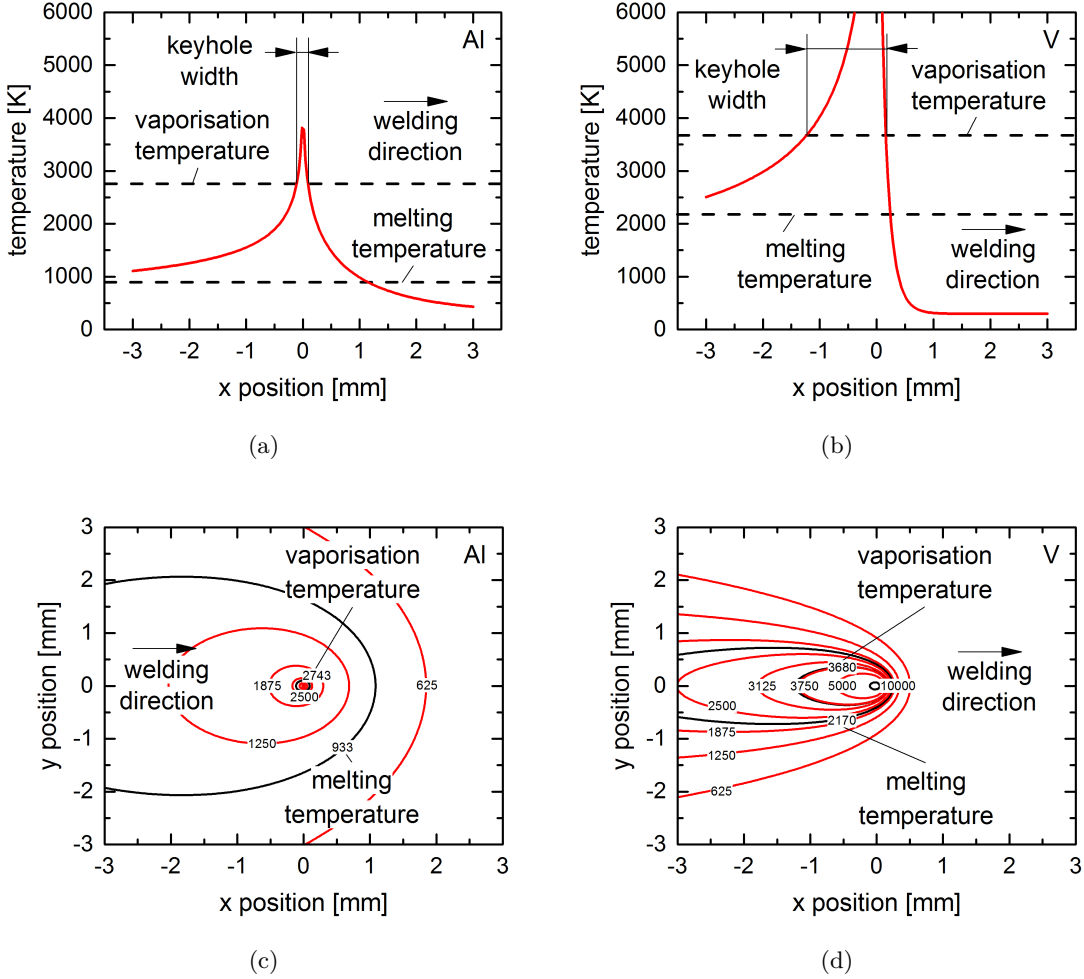


Figure 4.5.: Calculated temperature distribution (in K) during laser beam welding of aluminium (a)+(c) and vanadium (b)+(d) for constant welding parameters ( $P_l = 2.0$  kW and  $v = 3500$  mm/min) according to Eq. A.2 in the Appendix A.1.

The heat input in the material during the laser beam welding, and hence the approximate size of the melt pool and the keyhole, can also be estimated by the so-called line energy  $E$ , which is defined by the used laser power  $P_l$  per welding speed  $v$ .

$$E = \frac{P_l}{v} \quad (4.1)$$

With increasing line energy for a constant laser power the size of the melt pool - described by the melt isotherm - increases proportionally in  $x$  and  $y$  direction, as depicted in Fig. 4.6a. This means that with decreasing welding speeds the width of the fusion zone and heat affected zone increases. In case of a constant welding speed the expansion of the melt pool is not proportional in both directions (Fig. 4.6b). For a constant line energy the laser power has to be increased proportionally with the welding speed. Thus, the melt pool is mainly elongated in the welding direction  $x$ , as depicted in Fig. 4.7. The same assumptions are valid for the size of the keyhole - described by the vaporisation isotherm.

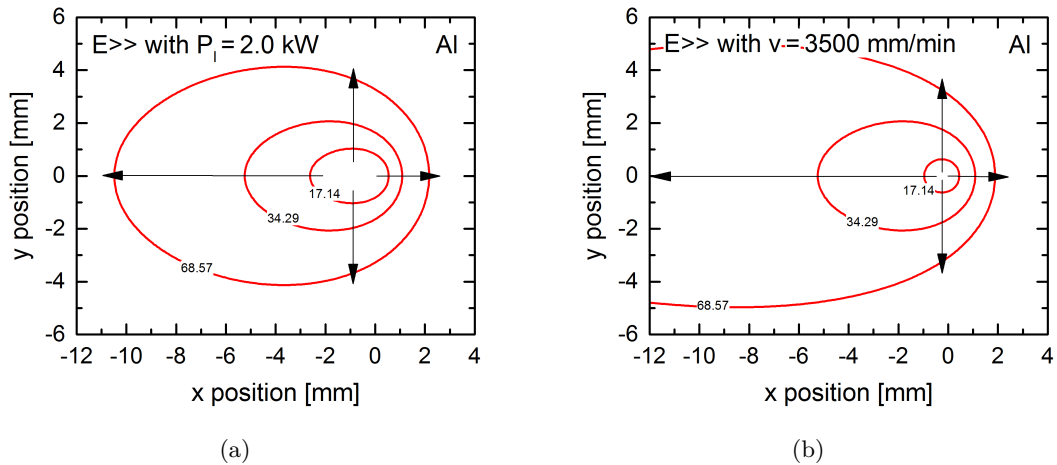


Figure 4.6.: Calculated melt pool dimensions of aluminium for increasing line energy (in J/mm) with a constant laser power (a) and with a constant welding speed (b) according to Eq. A.2 in the Appendix A.1.

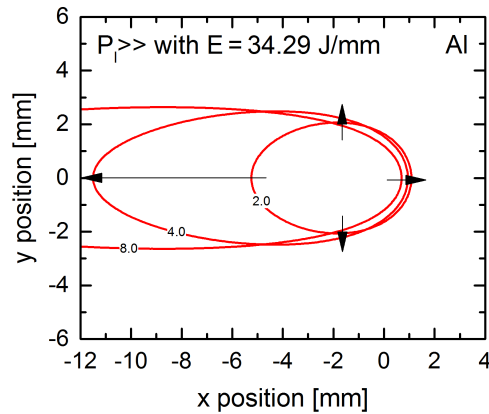


Figure 4.7.: Calculated melt pool dimensions of aluminium for a constant line energy with increasing laser power (in kW) according to Eq. A.2 in the Appendix A.1.

#### 4.4. Pressure conditions in the keyhole

In Section 4.2 the need of vaporisation for the formation of a keyhole during laser beam welding was already explicated. At the beginning of the deep penetration welding process, the material will be first melted and than locally vaporised at the surface. Due to the build-up of pressure during the vaporisation process the surface of the melting zone will be locally deformed so that a small depression is firstly generated. By further vaporisation this depression progressively deepens and a capillary starts to form. Consequently, interreflections occur within the capillary and the absorption is increased. This leads to a further increase of the vaporisation rate and thus to a deepening of the capillary. And finally, a deep penetrating keyhole will result [12, 51, 52]. The pressure due to vaporisation of the material, which is necessary for keeping the keyhole open during laser beam welding, is also called vapour pressure  $p_v$ . It mainly depends on the temperature  $T$  and the material coefficients  $A_v$ ,  $B_v$ ,  $C_v$  and  $D_v$ ,

as described in the work of Haynes [64] and Alcock et al. [61].

$$\log(p_v) = 5.006 + A_v + \frac{B_v}{T} + C_v \cdot \log(T) + \frac{D_v}{T^3} \quad (4.2)$$

The resulting vapour pressures for different metals in dependence of the temperature are shown in Fig. 4.8a. At the vaporisation temperature of the material the vapour pressure equates the ambient pressure.

By alloying zinc and magnesium to aluminium the vapour pressure is reduced. The resulting vapour pressure  $p_{x a}$  of the alloying element  $x$  in a binary aluminium alloy can be calculated by Raoult's law and the vapour pressure  $p_{x p}$  of the pure metal, as shown by Arata et al. [42].

$$p_{x a} = \gamma_x n_x p_{x p} \quad (4.3)$$

The activity coefficient  $\gamma_x$  is assumed to be equal to 1. The mole fraction  $n_x$  of the alloying element  $x$  can be calculated with the help of the mass fraction  $w$  (given by the chemical composition of the aluminium alloy) and the atomic mass  $M$  of the alloying element  $x$  and the base metal aluminium.

$$n_x = \frac{w_x/M_x}{w_x/M_x + w_{Al}/M_{Al}} \quad (4.4)$$

In Fig. 4.8b the vapour pressures of pure zinc and magnesium (solid lines) are compared to the vapour pressures of binary Al-Zn and Al-Mg alloys (dashed lines). The zinc and magnesium contents used for the calculation are representing the respective maximal content in typical high-strength Al-Zn alloys. The alloying of aluminium with 11wt.% zinc and 2.9wt.% magnesium leads to a decline of approximately 1 and 1.5 log cycles in comparison to pure zinc and magnesium, respectively. But these vapour pressures are still considerably higher than for pure aluminium or Al-Cu and Al-Si alloys.

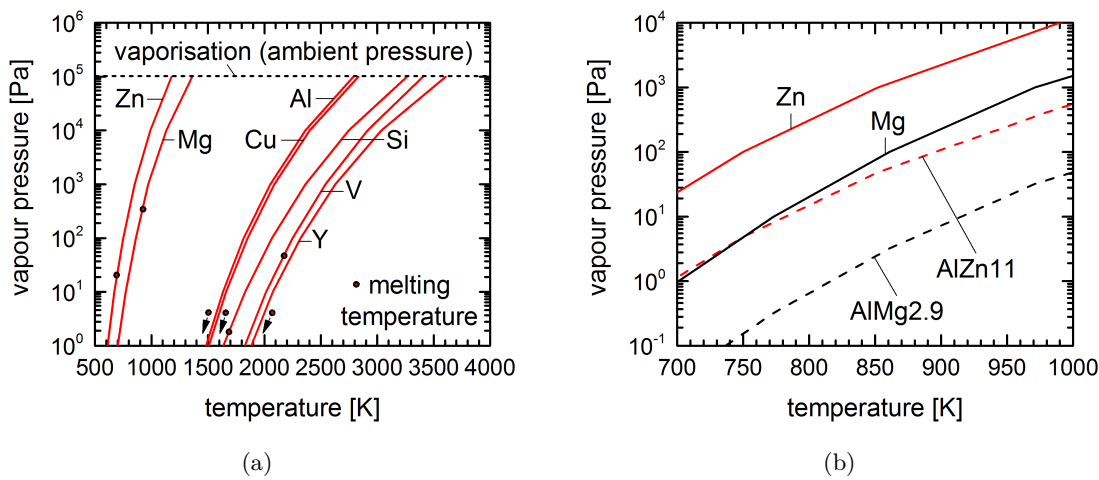


Figure 4.8.: Vapour pressure in dependence of the temperature for different pure metals (a) (calculated according to Eq. 4.2) and binary Al alloys (b) (calculated according to Eq. 4.3).

In the work of Beyer [51] it was stated that in the keyhole - with its predominant conditions (vapour flow off and saturation) - even higher vapour pressures can be reached, as shown in Fig. 4.9.

The vapour pressure of zinc and magnesium is very high even at low temperatures and a lower beam irradiance is needed. From this it can be concluded that these elements facilitate

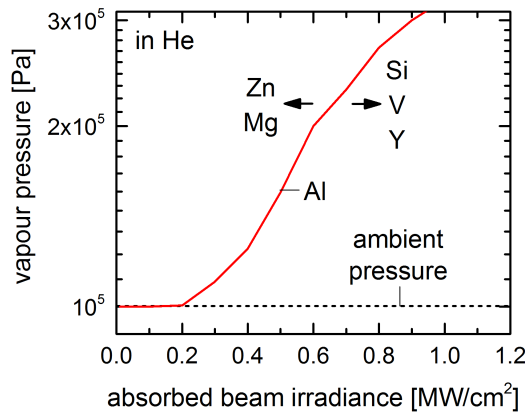


Figure 4.9.: Vapour pressure of aluminium in the keyhole in dependence of the absorbed beam irradiance (according to Beyer [51]).

the formation of the keyhole when alloyed to aluminium alloys. But on the other side, a severe problem is the irregular vaporisation due to the depletion of the volatile elements on the keyhole surface, which frequently occurs during the laser beam welding of high-alloyed aluminium. This generally leads to a temporary drop of the vapour pressure in the keyhole and hence to its collapse. In contrast, alloying of aluminium with metals like vanadium and yttrium lead to a shift to higher temperatures (Fig. 4.8a) and hence a higher beam irradiance is needed.

The counteracting pressure, which induces the closing of the keyhole during laser beam welding, is the so-called keyhole pressure  $p_k$ . Referring to the work of Beyer [51] and Kannatey-Asibu [52] it includes the capillary pressure  $p_c$ , dynamic pressure  $p_d$ , the hydrostatic pressure  $p_h$  and the atmospheric pressure  $p_a$ , as shown in Eq. 4.5.

$$p_k = p_c + p_d + p_h + p_a \leq p_v \quad (4.5)$$

The capillary pressure is defined by the keyhole diameter  $d_k = 2 \cdot r_k$ , which is assumed to be equal to the beam diameter  $d$ , and the surface tension  $\gamma$  of the melted material.

$$p_c = \frac{\gamma}{r_k} \approx \frac{2\gamma}{d} \quad (4.6)$$

The dynamic pressure depends on the density  $\rho$  of the melted material and the welding speed  $v$ .

$$p_d = \frac{\rho}{2} v^2 \quad (4.7)$$

The hydrostatic pressure strongly depends on the density  $\rho$  of the melted material and the thickness  $t_s$  of the sheet material. If the joint is not welded in the flat (PA) welding position, the welding position (defining the orientation of the melt pool in the gravitational field with the gravitational acceleration  $g$ ) has also an influence on the hydrostatic pressure.

$$p_h = \rho g t_s \quad (4.8)$$

The ambient pressure is assumed to be constant throughout the laser beam welding process, as long as no special device (as for example a vacuum chamber) for adjusting the pressure condition is used.

$$p_a = 101.325 \text{ kPa} = \text{const.} \quad (4.9)$$

Exemplary calculated results for the different pressures are shown in Fig. 4.10. The highest pressure values are achieved for the capillary pressure in case of low beam diameters. In contrast, the dynamic and hydrostatic pressures provide only insignificant contribution to the keyhole pressure, especially in case of low welding speeds and sheet thicknesses.

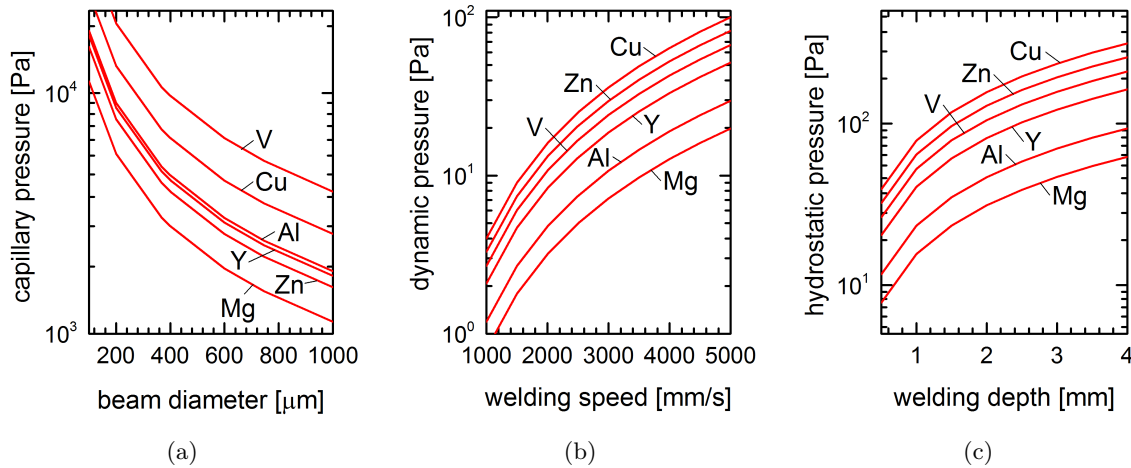


Figure 4.10.: Calculated capillary pressure (a), dynamic pressure (b) and hydrostatic pressure (c) for different pure metals (calculated according to Eq. 4.6 to 4.8 and Table 4.1).

In order to keep the keyhole during laser beam welding open, the vapour pressure should at least equate the keyhole pressure, as indicated in Eq. 4.5. The relation between the vapour pressure and the keyhole pressure for different pure metals (main alloying elements of Al-Zn alloys) is shown in Fig. 4.11. It can be easily seen that the difference between pressures is the largest for aluminium. This means that the metal tends to show weld pool instabilities. In case of magnesium both pressures are almost the same, which results in a stable welding process, although the vapour pressure is very high in comparison to aluminium. But since zinc and magnesium are only alloyed in lower proportions to aluminium, these high vapour pressures are also expected to be unstable during the welding process. The reason for this are temporary vapour pressures drops due to irregular vaporisation, as explained in Section 4.2.

In Fig. 4.12 the effect of counteracting of pressures and changing pressure conditions (due to irregular vaporisation) on the keyhole behaviour during laser beam welding is shown exemplarily. As a consequence of the resulting keyhole instabilities in terms of collapsing or necking of the keyhole, various weld defects may occur. In this regard typical weld defects are for example spatter, undercut, excess of penetration (spiking) and entrapped porosity in the weld seam.

## 4.5. Surface tension and viscosity

The surface tension and the viscosity of a liquid may also influence the weldability. As explained in Eq. 4.6 in the previous section, the surface tension has a considerable effect on the capillary pressure, which mainly affects the keyhole stability during laser beam welding. But in addition, the behaviour of the melt pool during laser welding is also defined by the surface tension and viscosity.

Both properties strongly depend on the chemical composition of the used aluminium alloys and the temperature. From Table 4.1 it can be seen that zinc and magnesium exhibit a low

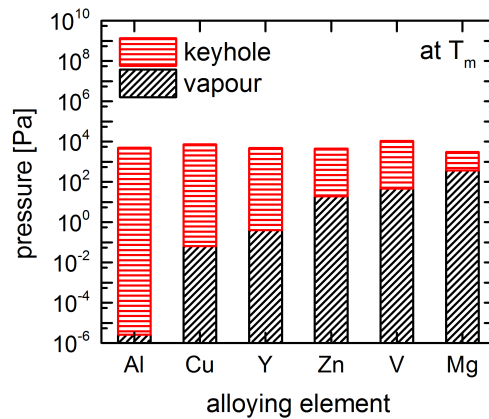


Figure 4.11.: Exemplary ratio of vapour pressure to keyhole pressure of different pure metals at their melting temperatures (calculated according to Eq. 4.2 and 4.5, with welding parameters  $d = 366 \mu\text{m}$ ,  $P_l = 2.0 \text{ kW}$ ,  $v = 3500 \text{ mm/min}$  and  $t_s = 2 \text{ mm}$ ).

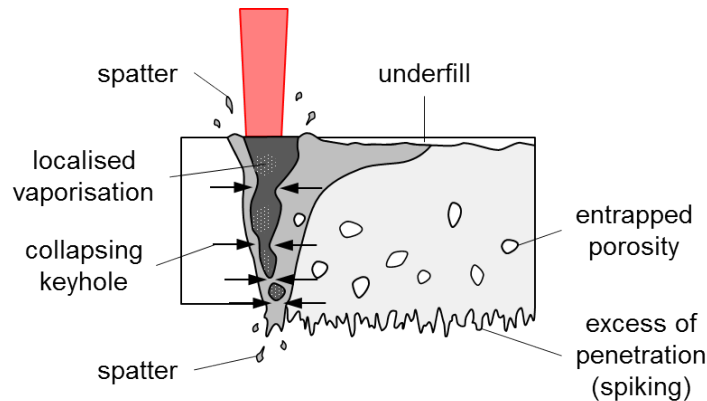


Figure 4.12.: Effect of unstable pressure conditions in the keyhole during laser beam welding on the resulting weld seam.

surface tension and magnesium also a low viscosity, in particular in comparison to aluminium. Both elements are contained in Al-Zn alloys in high concentrations. In Fig. 4.13a and Fig. 4.14a the influence of the alloying element content on the surface tension and viscosity is depicted. From this it becomes apparent that in particular high amounts of magnesium lead to a decline of both properties, whereas zinc has almost no influence. However, copper and probably also vanadium show a contrary behaviour due to the considerable higher values for the surface tension and viscosity, as it can be seen in Table 4.1. An increase of temperature results in a decrease of the surface tension and to greater extent of the viscosity, as shown in Fig. 4.13b and Fig. 4.14b.

The surface tension is the elastic tendency of liquids to acquire the least surface area possible. The viscosity of a liquid is the measure of its resistance to flow. On the occasion that a liquid material exhibits low surface tension and low viscosity, this may result in severe sagging of the melt pool in case of a large melt pool or the formation of drop-outs (spikes) and spatter at the root side of the weld seam in case of a small melt pool, as shown in Fig. 4.15. In both cases, the keyhole tends to collapse, which may result in the formation of porosity. For this reason this porosity is also called keyhole-induced porosity [12]. According to Leong

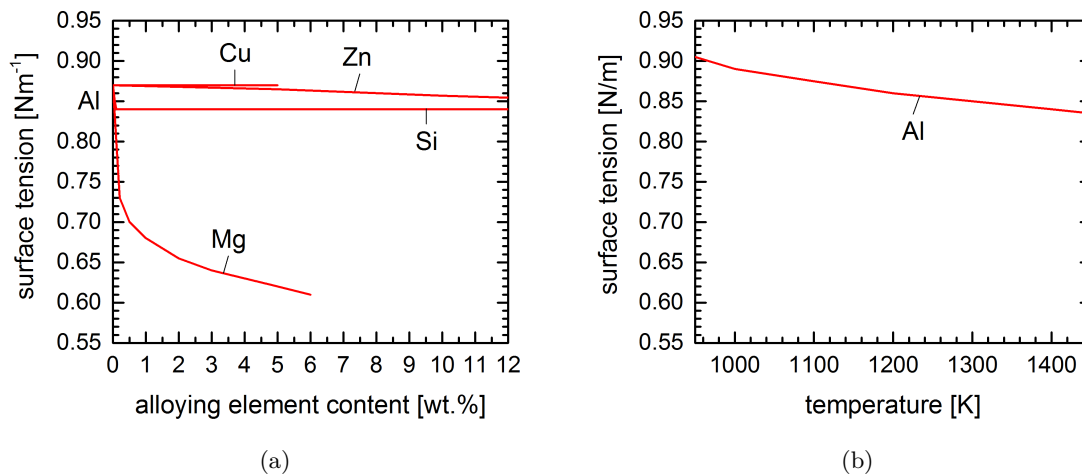


Figure 4.13.: Surface tension in dependence of the alloying element content of binary Al alloys (a) (according to Hatch [71]) and the temperature (b) (according to Lancaster [50]).

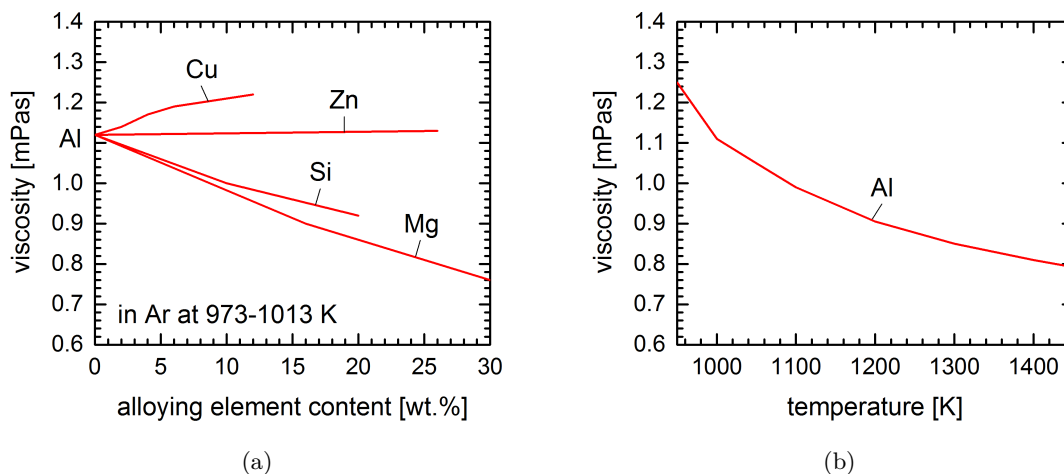


Figure 4.14.: Viscosity in dependence of the alloying element content of binary Al alloys (a) (according to Hatch [71]) and the temperature (b) (according to Mondolfo [17]).

et al. [59], this effect aggravates with decreasing sheet thickness, since the depth-to-width ratio of the weld seam decreases so that the melt pool appears larger in relation to the low sheet thickness.

Not only the outer appearance but also the fluid flow within the melt pool - during melting and solidification - is defined by the surface tension and viscosity [50]. In addition to that, the existence of surface active elements, such as oxygen, was reported, which may also locally influence the surface tension of the material [50, 72].

## 4.6. Absorption

The coupling of the laser beam with the material is mainly defined by the absorption of the material. The absorption  $A_l$  of the laser radiation is defined by the reflectivity  $R_l$  at the

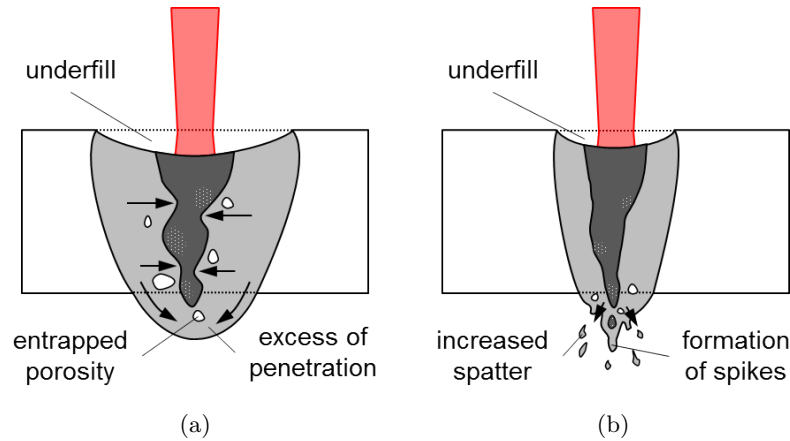


Figure 4.15.: Effect of low surface tension and viscosity on the resulting weld seam in case of an enlarged (a) and a downsized weld pool (b).

surface of a solid and the transmittance  $T_l$  through the material, as given in Eq. 4.10.

$$A_l + R_l + T_l = 1 \quad (4.10)$$

Assuming that the penetration of the laser radiation is very small in comparison to the thickness of the sheet material, the transmittance is set to  $T_l = 0$ . With the help of the Fresnel equations (Eq. 4.11) - considering the extinction coefficient  $k_e$  and absorption coefficient  $n_a$  - the absorption can be calculated (according to Beyer [51]).

$$A_l = 1 - \frac{(1 - n_a)^2 + k_e^2}{(1 + n_a)^2 + k_e^2} \quad (4.11)$$

The absorption  $A_l$  of pure aluminium and vanadium in dependence of the wavelength  $\lambda$  is shown in Fig. 4.16a. High wavelengths as for CO<sub>2</sub> lasers - with about  $10.6\mu m$  - are resulting in a very low absorption, whereas lower wavelengths as for Nd:YAG and fibre lasers - with approximately  $1.06\mu m$  seem to be more appropriate for laser beam welding of aluminium alloys. Other materials like vanadium show a significant better absorption in particular for the low wavelengths.

Besides the type of material and the wavelength of the laser, the absorption is also dependent for example on the angle of incidence, the polarisation of the radiation and the surface conditions of the material [51]. The influence of the temperature of a material on the absorption is shown in Fig. 4.16b. It can be seen that the absorption significantly increases, when the melting temperature of aluminium is reached, although it remains at a relatively low level [73]. But further increasing of the temperature will only result in a small increase of absorption. This means that once the laser welding process has been initialized the absorption is almost constant and sufficient for welding. In case of aluminium the high reflectivity of the material is often a considerable problem.

## 4.7. Beam irradiance

The weldability can be also expressed in terms of the laser beam irradiance. Leong et al. [58, 59] combined the most important thermophysical properties of a metal in dependence of the used laser source in the threshold irradiance. The threshold beam irradiance  $I_{th\ m}$  is given by the thermal conductivity  $k$  of the material, the melting temperature  $T_m$  of the material,

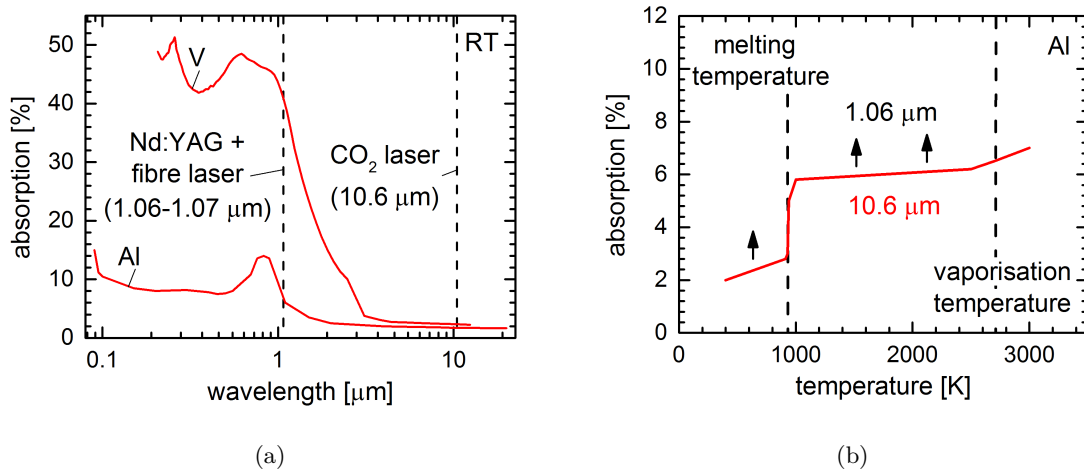


Figure 4.16.: Absorption of aluminium and vanadium as a function of wavelength (a) (calculated according to Beyer [51] and Guizzetti et al. [74]) and temperature (b) (according to Beyer [51]).

the ambient temperature  $T_0$ , the absorption  $A_l$  of the material for the wavelength  $\lambda$  of the used laser, the laser beam diameter  $d$  and the degree of interaction  $J_{max}$  (Eq. 4.12).

$$I_{th\ m} = \frac{k(T_m - T_0)}{A_l d J_{max}} \quad (4.12)$$

The degree of interaction  $J_{max}$  of the laser beam and the material is described by Eq. 4.13. The value ranges from 0.1 to 0.51 depending on the thermal diffusivity  $\alpha$  of the material, the beam diameter  $d$  and the welding speed  $v$ , as it can be seen in Fig. 4.17. For small beam diameters or low welding speeds the thermal diffusivity of the material dominates [58].

$$J_{max} = f\left(\frac{\alpha}{vd}\right) \quad (4.13)$$

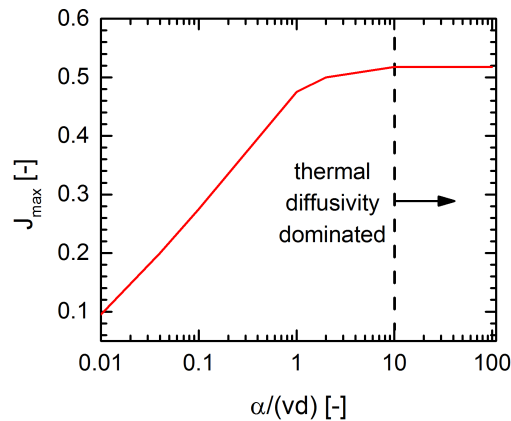


Figure 4.17.: Determination of the degree of interaction (according to Leong et al. [58, 59]).

The threshold irradiance defines the minimum beam irradiance, which is required for the melting or welding of the material. Here it has to be mentioned that for deep penetration laser

beam welding slightly higher beam irradiances are required. In Fig. 4.18 the influence of the metal, the laser beam diameter  $d$ , the absorption  $A_l$  and the welding speed  $v$  is exemplarily shown (referring to Eq. 4.12). It became apparent that the threshold irradiance is the highest for aluminium welded with a laser providing a small beam diameter, a low absorption - in case of a large wavelength - and high welding speeds. In this regard, the welding speed has the lowest influence on the threshold beam irradiance.

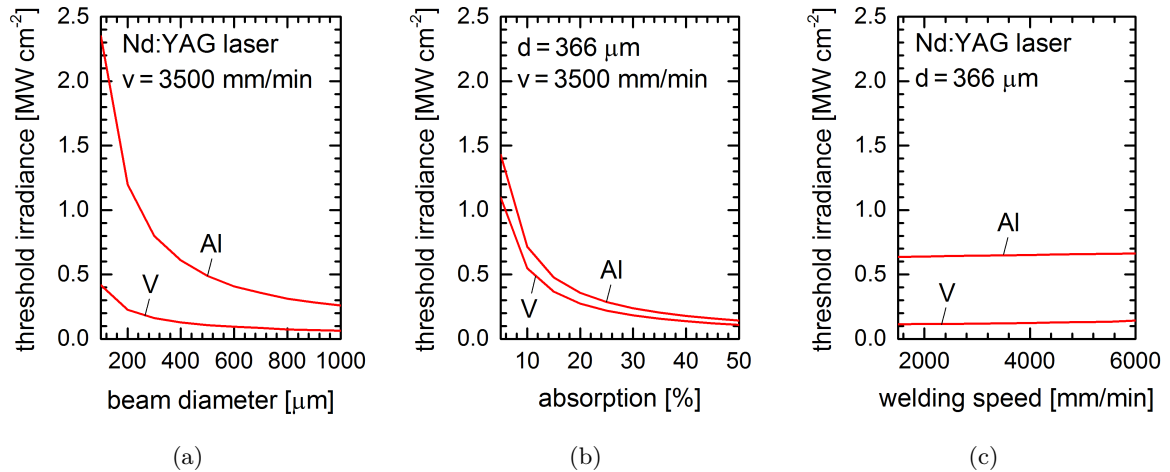


Figure 4.18.: Results of the analytical investigation of the influence of the beam diameter (a), the absorption (b) and the welding speed (c) on the threshold irradiance of aluminium and vanadium (calculated according to Eq. 4.12 and Table 4.1).

Referring to Leong et al. [58, 59], the presence of weld pool instabilities can be expected when high beam irradiances are applied to metals with low surface tension and low viscosity. Hence, only a narrow range of beam irradiance and process parameters may lead to reasonable welds.

Hügel [54] and Rapp et al. [56] deduced from the thermophysical properties of the material the threshold irradiance for keyhole welding. The resulting Eq. 4.14 for the threshold irradiance  $I_{th\ k}$  for long dwell times resembles the findings of Leong et al. [58, 59] in Eq. 4.12. However, in this case the vaporisation temperature  $T_v$  is used for the calculation.

$$I_{th\ k} = 4 \cdot \sqrt{\frac{2}{\pi}} \cdot \frac{kT_v}{A_l d} \quad (4.14)$$

In Fig. 4.19 the influence of the laser beam diameter and the absorption on the threshold irradiance is shown (referring to Eq. 4.14). The differences of the results - depicted in Fig. 4.18 and 4.19 - can be explained on the one hand by the equalization of melting and welding for Eq. 4.12 and on the other hand by the disregard of the exact dwell time (defined by the welding speed) for Eq. 4.14. Kawahito et al. [75] investigated the effect of the welding speed on the amount of absorbed energy during laser welding of aluminium. It was shown that an increase of the welding speed from  $1000\text{mm}/\text{min}$  to  $10000\text{mm}/\text{min}$  leads to a reduction of absorbed laser energy of approximately 14%. Nevertheless, both methods for the calculation of the beam irradiance can be used to estimate the real threshold beam irradiance for laser beam welding, whereas the first method represents an underestimation and the second method an overestimation.

In the work of Sakamoto et al. [53] the dependency of the beam irradiance on the welding depth was investigated. It was asserted that for a certain beam irradiance an abrupt rise of

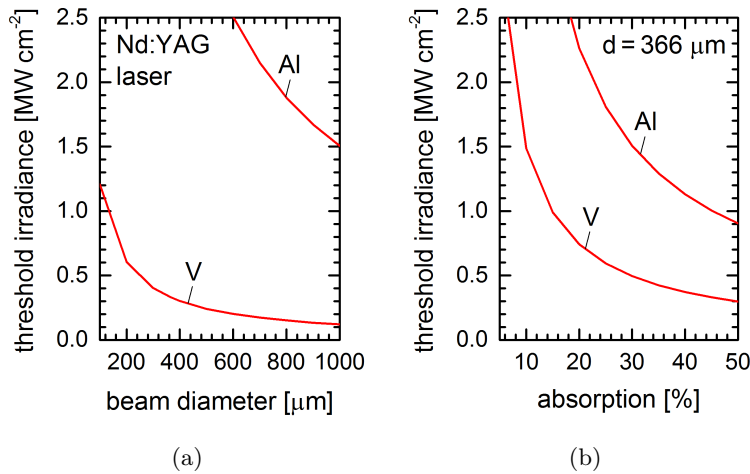


Figure 4.19.: Results of the analytic investigation of the influence of the beam diameter (a) and the absorption (b) on the threshold irradiance of aluminium and vanadium (calculated according to Eq. 4.14 and Table 4.1).

the welding depth was observed, as it can be seen in Fig. 4.20a. The reason for this is the formation of a deep penetrating keyhole - an evidence for the transition from heat conduction welding to keyhole welding. Further increase of the beam irradiance leads only to a slight increase of the welding depth. Furthermore, it was discovered that the threshold irradiance for keyhole welding strongly depends on the Zn+Mg content of the welded aluminium alloy, as shown in Fig. 4.20b. The explanation for this dependency was found in the low melting and evaporation temperature of zinc and magnesium, as explained in Section 4.2, rather than in their thermal conductivity. The influence of the welding speed is supposed to be very small.

From the calculated threshold irradiance  $I_{th}$  the required laser power  $P_l$  for a given laser beam diameter  $d$  can be deduced.

$$P_l = \frac{I_{th}\pi d^2}{4} \quad (4.15)$$

By defocussing of the laser beam (in positive or negative direction) the laser beam diameter is increased, as illustrated in Fig. 4.21a. In order to keep the beam irradiance constant, the laser power has to be increased referring to Eq. 4.15. In Fig. 4.21b the relation between laser power and beam diameter is depicted. The minimum beam diameter is defined by the laser optical system. However, too large defocussing of the laser beam above the Rayleigh length generally results in an inappropriate beam irradiance distribution, as demonstrated in Fig. 4.21c).

## 4.8. Solidification

Besides the melting and vapourisation of the material during laser beam welding - as described in Section 4.2 - the solidification of the melt also plays an important role for the weldability of a material, since this is one of the main factors affecting the hot cracking sensitivity, as shown in Fig. 4.22. The interactions of the material (chemical composition) and the process (thermal cycle during welding and cooling) control the solidification - in terms of solidification range and the resulting microstructure in the fusion zone. Of course, the way of solidification will also influence the thermomechanical response (stress and strain distribution) of the material during welding due to thermal expansion and shrinkage and restraint (Cross [76]).

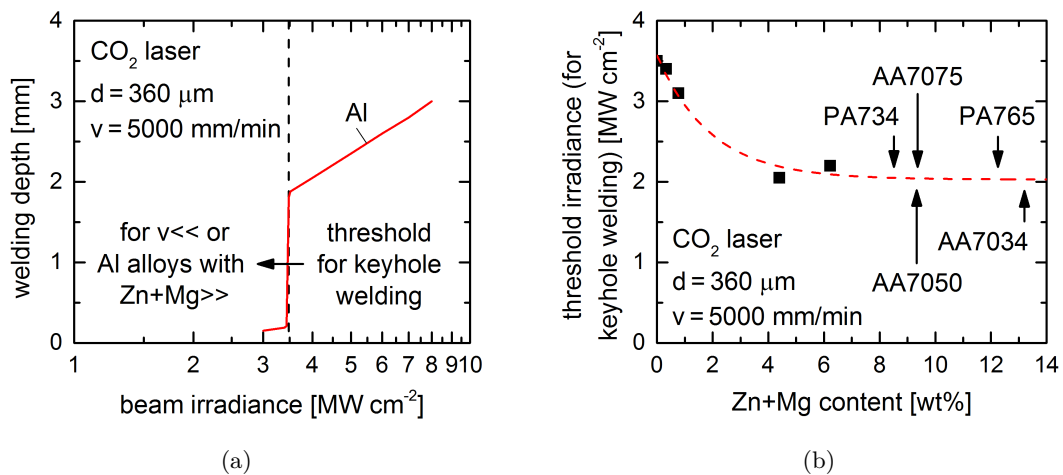


Figure 4.20.: Threshold irradiance for keyhole welding (a) and the influence of the Zn+Mg content on the threshold irradiance (b) (according to Sakamoto et al. [53]).

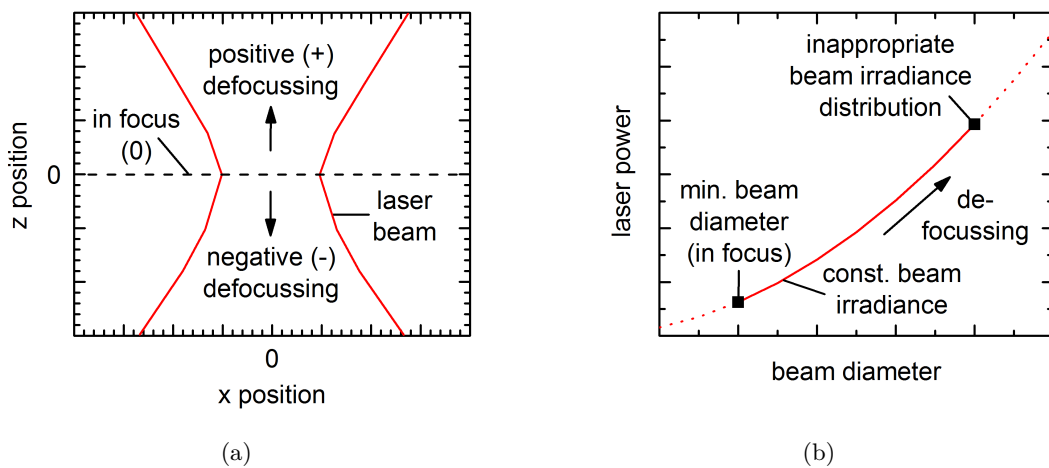


Figure 4.21.: Influence of large defocussing of the laser beam on the beam diameter (a), the required laser power for keeping the beam irradiance constant (b) and the irradiance distribution (c).

Generally, it is assumed that hot cracking sensitivity of an alloy correlates with the extent of the solidification range [57], as shown in Fig. 4.23a. The solidification temperature corresponds to the melting temperature of a pure metal. And the solidification range - the temperature range between the liquidus and solidus line in a phase diagram - of an alloy strongly depends on its chemical composition. The addition of the main alloying elements zinc, magnesium and copper leads to an increase of the solidification range, as it can be seen

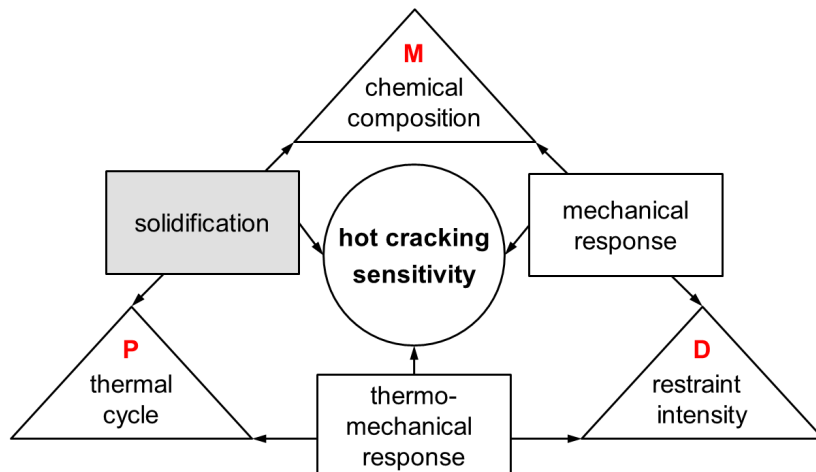


Figure 4.22.: Three main influencing factors affecting the hot cracking sensitivity of materials during welding (according to Cross [76]).

in the phase diagrams in Fig. A.3 to A.5 in the appendix of this thesis. In case of copper and magnesium a critical value exists, at which the cracking sensitivity is maximal, as indicated in Fig. 4.23b.

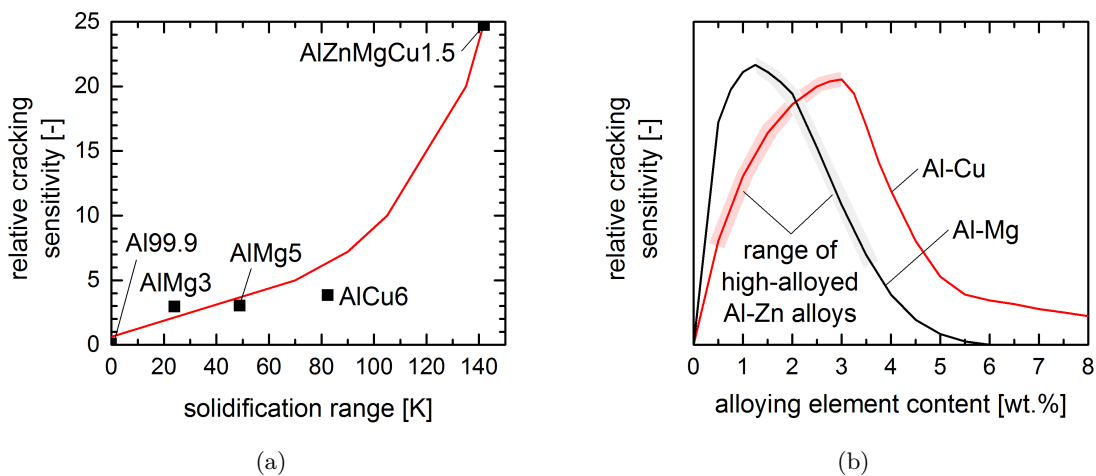


Figure 4.23.: Influence of the solidification range (a) (according to Rapp [57]) and the chemical composition (b) (according to Coniglio [77]) on the relative cracking sensitivity of Al alloys.

During the cooling of the melt a coherent network of primary solidified grains is formed. Due to the low amount of remaining melt between the solidified grains, the resulting structure possesses a certain strength but no ductility. This is the reason why the high strains are located mainly at the grain boundaries. The resulting stresses lead to local plastic deformation and to discontinuities, which cannot be healed by the remaining melt. This process ends, when the melt pool is completely solidified. The temperature range between the formation of the first grain network and the completed solidification is also called the coherence or brittle temperature range and is generally smaller than the solidification range. The hot cracking process is strongly linked to the cooling rate [57].

A distinction is made between solidification cracks in the fusion zone due to unfavourable

solidification conditions and liquidation cracks in the heat affected zone due to the liquidation of low melting eutectics at the grain boundaries.

Moreover, the solidification microstructure strongly influences the cracking sensitivity of the fusion zone. Here, typical influencing factors are the back-filling, the degree of dendrite coherency, the eutectic fraction, the grain shape, the grain structure and the grain size, as described in detail in the work of Coniglio [77], Coniglio et al. [78] and Cross [76].

The influence of zinc in particular on the hot cracking sensitivity of aluminium alloys is not well reported in literature. But due to the existence of Al-Zn alloys with very low hot cracking sensitivity the effect of zinc is supposed to be small. These Al-Zn alloys generally contain only low amounts of magnesium and no copper. The addition of magnesium has only a limited effect on hot cracking sensitivity although the solidification range is enlarged, whereas the addition of even small amounts of copper results in a significant increase of hot cracking. Because of the higher copper content in high-alloyed and high-strength Al-Zn alloys, these alloys exhibit a very high hot cracking sensitivity.

## 4.9. Porosity formation

The main factors affecting porosity formation during laser beam welding of aluminium alloys are shown in Fig. 4.24. Besides keyhole instabilities - explained in the previous sections - another reason for porosity in aluminium laser weld seams is the presence of hydrogen in the melt pool. Keyhole-induced porosity is generally caused by the interaction of the laser beam welding process and the chemical composition of the material, whereas the hydrogen-induced porosity is solely induced by the material and its prior processing.

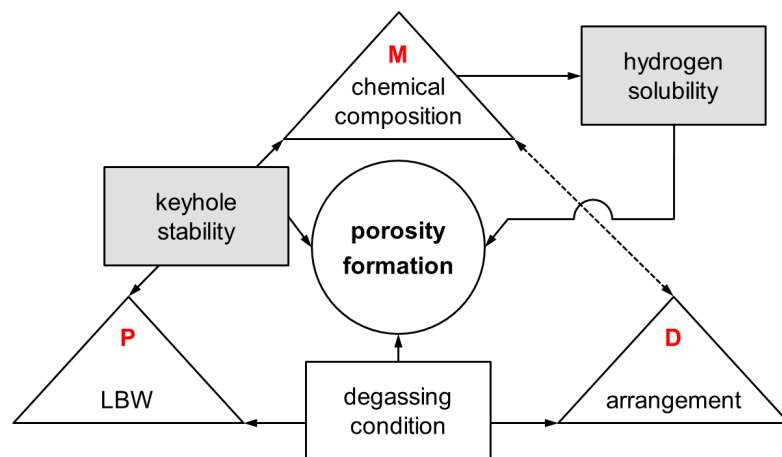


Figure 4.24.: Three main influencing factors affecting the porosity formation in materials during laser beam welding.

Hydrogen-induced porosity can be explained by the high solubility of hydrogen in liquid aluminium, as shown in Fig. 4.25a. This means that especially during welding the melted aluminium can easily solubilise a large amount of hydrogen. During solidification of the melt the solubility of hydrogen is extremely reduced. If the effective solubility limit of hydrogen is exceeded and degassing of the weld pool during solidification is impossible, gas porosity is formed [18]. For this reason the melt pool has to be protected from the ambient air, for example by the use of shielding gas during welding. But hydrogen can also originate from the base and filler material in form of an oxide layer and surface contaminations as well as

dissolved hydrogen in the bulk material. On the one hand, by removing of the surface layer and subsequent cleaning prior to the welding process it is possible to reduce the amount of hydrogen. On the other hand, the removal of the dissolved hydrogen is very difficult. One possibility is a degassing annealing of the material. But since most of the alloys are already supplied in a certain temper condition, this treatment is only applicable for filler materials where no specific temper condition is required. In addition, an annealing treatment is always very costly and time-consuming.

The solubility of hydrogen in aluminium alloys is strongly influenced by their chemical composition, as demonstrated by Anyalebechi [79]. In Fig. 4.25b the effect of content of zinc, magnesium and copper - the main alloying elements of Al-Zn alloys - on the hydrogen solubility of binary aluminium alloys is indicated. In this context, the hydrogen solubility is in particular influenced by the magnesium content, which significantly increases the solubility, whereas the zinc and copper content only slightly decrease the solubility.

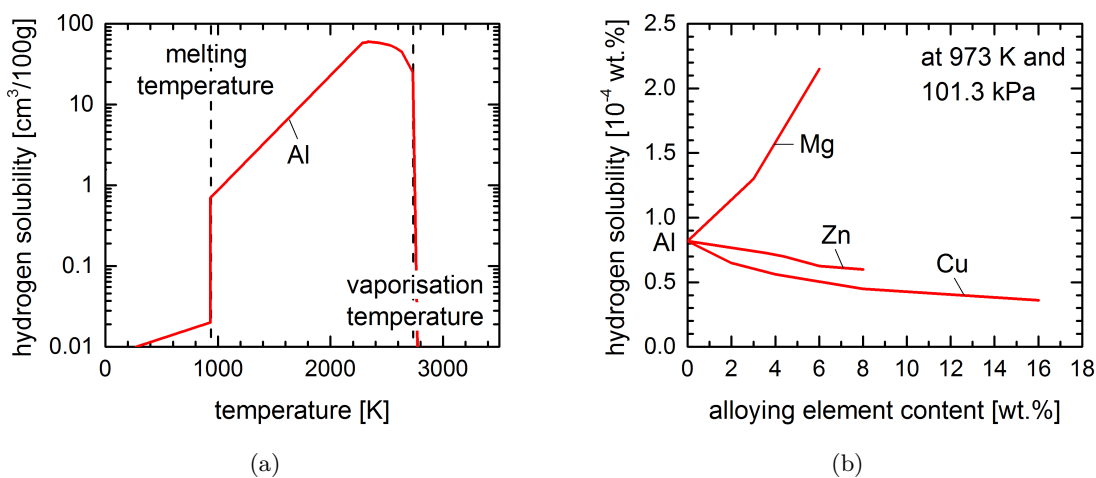


Figure 4.25.: Hydrogen solubility of aluminium in dependence of the temperature (a) and the alloying element content (b) (according to Anyalebechi [79]).

In order to assess the influence of hydrogen prior to welding, a measurement of the initial hydrogen content of the base and filler material is recommended. For the investigation of the reasons for porosity already occurred in the weld seam, a measurement of the resulting hydrogen content can be conducted. Furthermore and according to the work of Verhaeghe [12], hydrogen-induced porosity appears considerable smaller in diameter in comparison to keyhole-induced porosity. By this, it is possible to distinguish between keyhole- and hydrogen-induced porosity.

## 4.10. Weld imperfections

The general classification and characterization of weld imperfections for fusion welding processes is generally done according to the International Standards ISO 6520:2007 [80]. And for the assessment of the welds for the laser beam welding of weldable aluminium alloys in particular, the International Standard ISO 13919-2:2001 [81] is used. A selection of typical inner and outer weld defects - which can occur during laser beam welding - is illustrated in Fig. 4.26.

Moreover, weld imperfections exist, which exclusively occur during laser beam welding. Such laser specific imperfections are blowholes or dropouts. These are caused by excessive

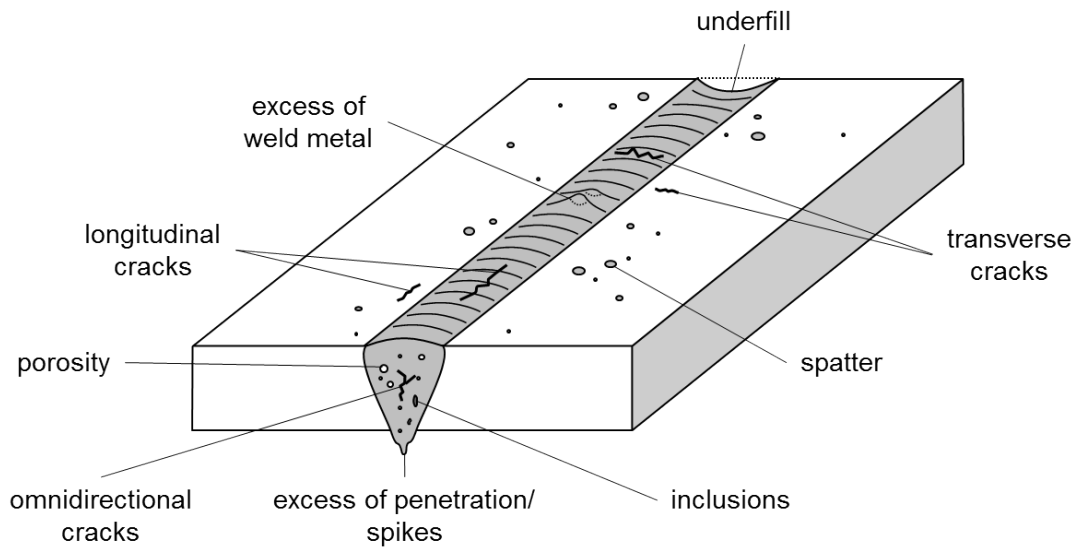


Figure 4.26.: Typical appearance of inner and outer weld defects.

vaporisation and weld metal expulsion during welding due to too high beam irradiances. Another laser specific imperfection is humping, which is partial periodic drop formation at the top surface of the weld. This is caused by capillary waves due the exceeding of a critical welding speed [51].

All these discontinuities can be detected by non-destructive and destructive testing. Common non-destructive test methods are for example visual testing, liquid penetrant testing and radiographic testing. The selection of the test method strongly depends on the physical characteristics of the material and the discontinuities of most interest, including their probable location, orientation, size and morphology [82]. Other non-destructive test methods and their working principle are described in detail for example by Crowe [82]. With the help of destructive testing it is possible to detect metallurgical weld imperfections, which is in general impossible for non-destructive testing, for example by metallographic testing. Furthermore, it is possible to assess the influence of all weld imperfections on the resulting mechanical properties - for example by hardness and tensile testing.

## 5. Approaches for improving the laser weldability

This chapter is dedicated to the different approaches for improving the laser weldability of high-alloyed Al-Zn alloys. At the beginning, various earlier approaches of other authors for improving the laser weldability of different materials are presented, which may also be applied to Al-Zn alloys. Subsequent, the newly developed approaches for the use for high-alloyed Al-Zn alloys are introduced. The approaches differ in their functionality, but not in their goal - to stabilize the keyhole during laser beam welding. The knowledge about the fundamentals of laser weldability, described in the previous Chapter 4, will be used to describe the functionality of these approaches.

### 5.1. Earlier approaches for different materials: State-of-the-art

In the past years diverse approaches have been developed for improving the laser weldability. But to simplify matters, the majority of them was only applied to steels, which are generally easier to weld in comparison to high-alloyed Al-Zn alloys. Since the functionality of the approaches base upon the fundamentals described in the previous Chapter 4, it is anticipated that they may also be applied to hard-to-weld Al-Zn alloys.

A very early approach for improving the laser weldability is the so-called multi-beam welding, which implies the use of an additional or split laser beam. Kannatey-Asibu [52], Trautmann et al. [83] and Kronthaler [84] described the possibility of such a multiple laser beam system to reduce the formation of defects such as porosity, spiking and incomplete penetration. Here, the second laser beam can fulfil different tasks. If the second laser beam has a lower irradiance and a broad distribution, it can be used to preheat the area in front (leading configuration), in behind (trailing configuration) or around the first laser beam, which generally has a higher irradiance and a narrow irradiance distribution. Thus, it is possible to increase the penetration depth - by increasing the heat input necessary for melting and vaporisation (Section 4.2) - or to influence solidification - by adjusting the thermal cycle (Section 4.8), as shown in Fig. 5.1a and Fig. 5.2. Otherwise, if the second laser beam has a high irradiance, a narrow irradiance distribution and moves very close to the first laser beam, it can be used to stabilize the keyhole during welding and to enlarge the keyhole - by increasing the vapour pressure and reducing the resulting keyhole pressure at the same time, in order to improve the balance between both (Section 4.4). Furthermore, the degassing conditions can be also improved by an enlarged keyhole, as shown in Fig. 5.1b. In this regard, typical process variations are for example the power level, the incident beam position, the initial beam profile, the focal position and the incident beam angle of each of the used lasers.

The recent development of innovative laser optics with so-called diffractive optical elements (DOEs) facilitate the shaping of the laser beam in terms of the beam irradiance distribution, as described in the work of Hansen et al. [85]. Thus, the keyhole shall be shaped and stabilized during the laser beam welding. In addition, it is possible to emulate the irradiance distribution of a dual laser beam welding process, as shown in Fig. 5.2, with the advantages described in the previous paragraph.

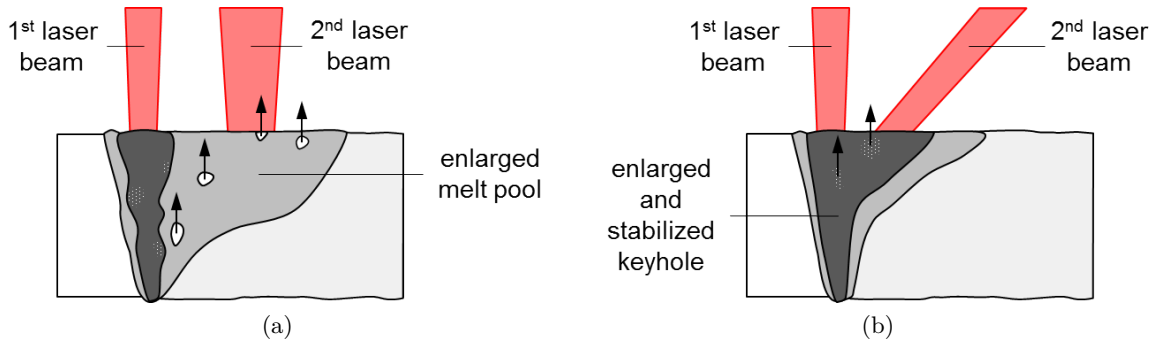


Figure 5.1.: Examples for improving the degassing behaviour by the use of a second laser beam for the enlargement of the melt pool (a) or the keyhole (b).

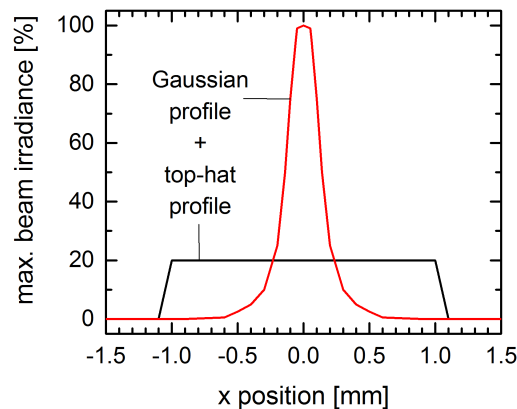


Figure 5.2.: Applicative combination of laser beam profiles for multiple or diffractive optical element laser beam welding.

Katayama et al. [86], Börner et al. [87, 88], Youhei et al. [89] and Reisgen et al. [90] investigated the effect of the ambient pressure on the laser weldability of aluminium alloys. It turned out that sub-atmospheric pressures (from  $\approx 10\text{mbar}$  to vacuum) lead to an improvement of the laser weldability. This can be explained by the fact that the keyhole pressure is reduced in order to improve the balance between vapour pressure and keyhole pressure (Section 4.4). The melting and vaporisation temperatures (Section 4.2) are reduced due to the low ambient pressure, which enables the use of a lower power level or a higher welding speed. Luo et al. [70] showed that the formation of shielding plasma plume diminishes and the laser welding process becomes more stable. Katayama et al. [86] pointed out that the liquid flow in the melt pool during vacuum laser welding is reversed and thus, also the degassing is improved. Finally, all this results in an improved keyhole stability during laser beam welding, with less porosity, spatter, plume and spiking. Furthermore, the aspect ratio of the resulting weld seam can be also increased. The weld seams of this laser welding technique resemble to great extent those of electron beam welding. Although, vacuum laser beam welding requires an higher manufacturing effort, first close-to-production test series were already performed, as shown by Reisgen et al. [90]. Schneider et al. [91] recently developed a mobile apparatus for the laser welding under locally reduced pressure conditions, which could improve the applicability of this approach to a certain extent.

## 5.2. First approach: The use of an additional filler material

The first approach presented in this thesis is based on a Patent [92, 93] of the Helmholtz-Zentrum Geesthacht (HZG). It implies the use of an appropriate filler material - additional to a conventional filler wire. From the theoretical considerations in Chapter 4 it can be reasoned that the transition metal vanadium is an appropriate candidate for a filler material for improving the weldability of Al-Zn alloys. The reasons for this are on the one hand its high vaporisation temperature (Fig. 4.3) and low vapour pressure (Fig. 4.8), which inhibits an early and irregular vaporisation and thus the formation of weldability problems. On the other hand, vanadium provides a high absorption (Fig. 4.16) and a low threshold beam irradiance for welding (Fig. 4.18 and 4.19) in combination with a high surface tension and viscosity, which generally denotes good weldability of a material.

Other potential filler materials with promising thermophysical properties generally fail due to merely one detrimental property. Such a material is for example the transition metal and rare earth element yttrium. At first glance, it possesses convenient thermophysical properties (Table 4.1) as for example a high vaporisation temperature and a low vapour pressure. But due to the low surface tension and viscosity the use of yttrium will always lead to weldability problems. This is exemplarily shown in Fig. 5.3 by the results of a preliminary study with yttrium. It can be seen that yttrium causes an excess of penetration at the root side as well as severe weld porosity, which even exceeds the level of the non-improved welds. Furthermore, the weld seam exhibits a very non-uniform appearance.

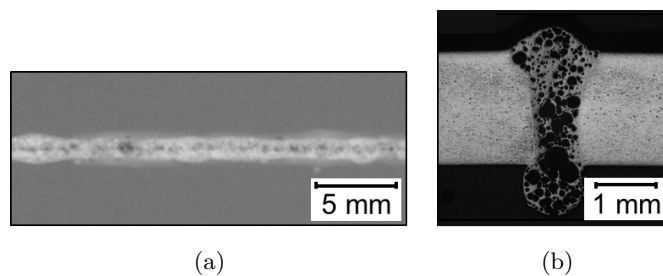


Figure 5.3.: Radiograph (a) and macrograph (b) of a joint laser beam welded with a 25  $\mu\text{m}$  yttrium foil and a conventional AA5087 filler wire.

The type of laser used for this first approach and thus all other laser-specific properties - such as beam diameter and Rayleigh length - play only a subordinated role and can be adjusted for a specific application. But since the absorption is low for almost all materials, the use of a  $\text{CO}_2$  laser should be refrained from. In order to demonstrate the capability of this approach, a commonly used medium power Nd:YAG laser was used for welding.

## 5.3. Second approach: The use of an initially large beam diameter

The second approach presented in this thesis implies the use of an appropriate laser for improving the weldability instead of an additional filler material. From the theoretical considerations in Chapter 4 it can be reasoned that a large keyhole has a beneficial effect on the weldability. The reason for this is the lowered capillary pressure (the largest fraction of the keyhole pressure), which induces the closing of the keyhole during laser beam welding, and the lowered threshold beam irradiance for welding, which improves the weldability even in case of higher surface tension and viscosity as for Al-Zn alloys. In addition, the degassing conditions may also be improved for larger keyholes.

For the realization of a large keyhole during laser welding an initially large laser beam is required. The enlargement of the laser beam diameter can be realized either by defocussing in case of a fixed optical set-up or by the adjustment of the optical set-up. Here, the beam diameter is defined by the used fibre diameter and laser optic - including a collimation and focussing unit. But since the beam irradiance reduces and the beam irradiance distribution changes with increasing defocussing especially above the Rayleigh length, the enlargement of the laser beam diameter solely by defocussing should be refrained from. Furthermore, too high defocussing leads to instabilities or even the disappearance of the keyhole - especially for Nd:YAG lasers, as stated by Pastor et al. [94, 95] and Verhaeghe [12]. The reduction of the beam irradiance due to defocussing can partly be compensated by the adjustment of the laser power to higher values.

Here, the beam irradiance distribution, which is sometimes also called laser beam profile, can also have an influence on the weldability. The two most common laser beam profiles - namely Gaussian and top-hat - are depicted in Fig. 5.4. In case of the Gaussian profile the maximum irradiance is concentrated in a small area in the centre of the beam, which generally leads to a very narrow keyhole. In contrast to that, the top-hat profile provides a large area, which almost correlates with the laser beam diameter, of constant maximum irradiance. This finally helps to form a large and stable keyhole during laser beam welding. As mentioned earlier, large defocussing of the laser beam generally results in a change of the beam profile shape from a top-hat profile to a more Gaussian-like profile. The beam profile is defined by the used laser optic. For the sake of completeness it has to be mentioned that of course other beam shapes are also possible, which can be achieved by DOEs, as mentioned in Section 5.1.

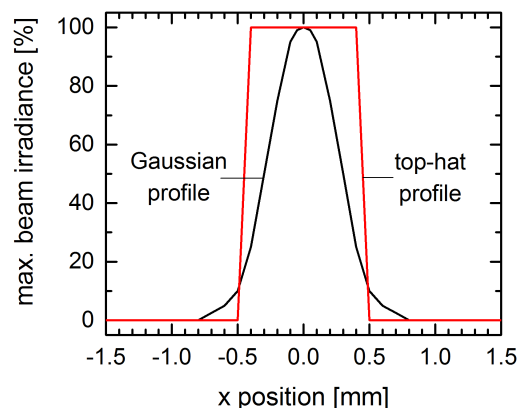


Figure 5.4.: Typical appearance of a Gaussian and a top-hat beam profile.

For ensuring deep penetration during welding with an enlarged beam diameter as well as a high laser power level are required, since the irradiance - which is in simple terms the energy per unit area - is reduced. Novel fibre lasers generally possess higher power levels in comparison to the commonly used Nd:YAG lasers, whereas the wavelength of both laser types are almost identical - with  $\lambda_{Nd:YAG} = 1.064\mu m$  and  $\lambda_{Yb:fibre} = 1.070\mu m$ .

Another advantage of fibre lasers is that they provide smaller and hence better beam parameter products even at high power levels in comparison to other laser sources [96, 97], as it can be seen in Fig. 5.5. The beam parameter product describes the beam quality in terms of focusability (Rayleigh length) and determines the amount of useful energy delivered to the material surface [98].

Another way of enlarging the keyhole dimensions (besides the enlargement of the laser beam itself) is the adjustment of the laser welding parameters. According to Section 4.3, it is

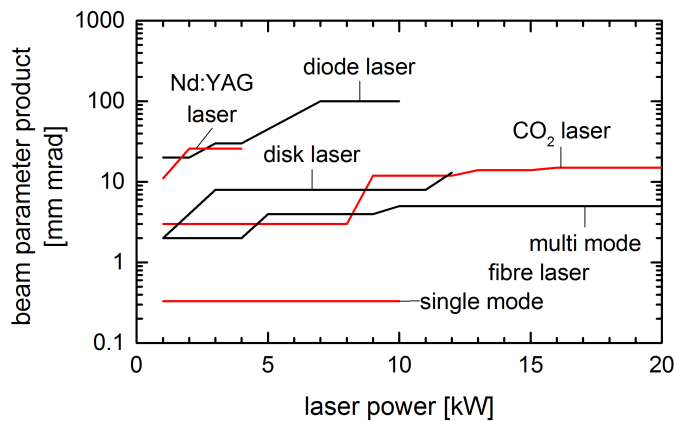


Figure 5.5.: Dependency of the laser power on the beam parameter product of different laser sources (according to Stiles [96]).

possible to keep the melt pool size constant and to elongate the keyhole in welding direction  $x$  by the proportional increase of the laser power and the welding speed. But for this purpose a high-power laser with a high beam quality is necessary, as for example a fibre laser. This method for the upscaling of keyhole dimensions is not only limited by the maximum available laser power but also by a maximum welding speed. For very high welding speeds interaction of the laser beam and the material becomes smaller (according to Section 4.7). Moreover, the keyhole tends to be more unstable due to the increase of the dynamic pressure and thus also to a disequilibrium of the vapour pressure and the keyhole pressure, as described in Section 4.4.

The laser-specific terms used in this section are described in detail in the Appendix A.2 of this thesis.

## 6. Experimental methodology

For assessing the feasibility of the developed approaches, described in the previous Chapter 5, they have to be applied to various Al-Zn alloys. A high Zn+Mg+Cu content is supposed to aggravate the weldability problems of Al-Zn alloys. For this reason, the effectiveness of both approaches is most interesting for high-alloyed and hard-to-weld Al-Zn alloys.

In this chapter the high-alloyed Al-Zn alloys used in this study are presented. Furthermore, the laser beam welding processes for the different welding scenarios are described. This includes the 'worst-case' and 'variation' welding scenarios for comparison purposes as well as the 'enhanced' welding scenarios for both approaches. The analytical methods used for the assessment of the resulting joints are also explicated in this chapter. They allow the determination of the outer appearance and the chemical, microstructural and mechanical properties.

### 6.1. Materials

The weldability of five different Al-Zn alloys was studied, which mainly differed in their zinc, magnesium and copper contents. For this purpose the commercial alloys AA7075, AA7050 and AA7034 as well as the pre-alloys PA734 and PA765 were used as base materials. Among these, the alloy AA7034 offered the highest zinc content as well as the highest Zn+Mg+Cu content with 14.3 wt.%. The exact chemical compositions and corresponding temper conditions are specified in Table 6.1. The temper condition of the base materials was either peak-aged (T6) or over-aged (T7X). The peak-aged condition provides the highest possible strength, whereas the over-aged condition represents a good compromise between strength and corrosion resistance. However, over-ageing generally results in a loss of strength of about 10-15% [99].

Table 6.1.: Chemical composition of the used Al alloys (in wt.%) - ordered by increasing Zn+Mg+Cu content.

alloy	temper	Si	Fe	Cu	Mn	Mg	Cr	Zn	Ti	Al
AA5087	-	0.24	0.4	0.05	1.1	5.2	0.25	0.25	0.15	Bal.
PA734	T79	0.03	0.04	2.13	0.01	1.64	–	6.77	0.02	Bal.
AA7075	T6	0.4	0.5	2.0	0.3	2.9	0.28	6.1	0.2	Bal.
AA7050	T76	0.12	0.15	2.6	0.1	2.6	0.04	6.7	0.06	Bal.
PA765	T79	0.05	0.1	0.61	0.14	2.72	0.15	9.47	0.02	Bal.
AA7034	T6	0.1	0.12	1.0	0.2	2.3	0.2	11.0	–	Bal.

The majority of the Al-Zn alloys were available as rolled sheets, whereas the alloys AA7034 and PA765 were only available as extruded profiles. Another special feature of AA7034 was the melt spinning processing of the material prior to the extrusion process, which provided a very fine grained and homogeneous microstructure. In order to achieve comparable results, all sheets were conformed to a thickness of 2.0 mm - if necessary - either by milling or by spark erosion. Prior to welding all specimens were ground in the welding zone and subsequently cleaned with alcohol in order to remove the oxide layer and other surface contaminations.

Al-Mg alloys are generally recommended as filler material for the welding of Al-Zn alloys. For this reason the alloys AA5087 was chosen as filler wire. The chemical composition is also given in Table 6.1. The used wire had a diameter of 1.0 mm. Concerning the first approach, described in Chapter 5, a 99.8% pure vanadium foil with a thickness of 40  $\mu\text{m}$  was used additionally to the conventional filler wire. In case of the second approach no additional filler material was used.

In a preliminary study different potential additional filler materials as well as various foil thicknesses were tested.

## 6.2. Laser beam welding

For the laser beam welding of both approaches two different laser types and configurations were used, which were chosen and adjusted for each of the approaches.

The laser beam welding for the first approach was performed using a 3-axial CNC machining centre (IXION ULM 804) - providing a high positioning accuracy - which was connected to a 2.2 kW Nd:YAG rod laser (ROFIN-SINAR DY022). The laser beam welding of the second approach was performed using the same machining centre, which was this time connected to an 8.0 kW Yb multi-mode fibre laser (IPG YLS-8000) and which possesses a more compact design (Fig. 6.1). The different characteristics of both laser systems - with different optical systems - are summarized in Table 6.2.

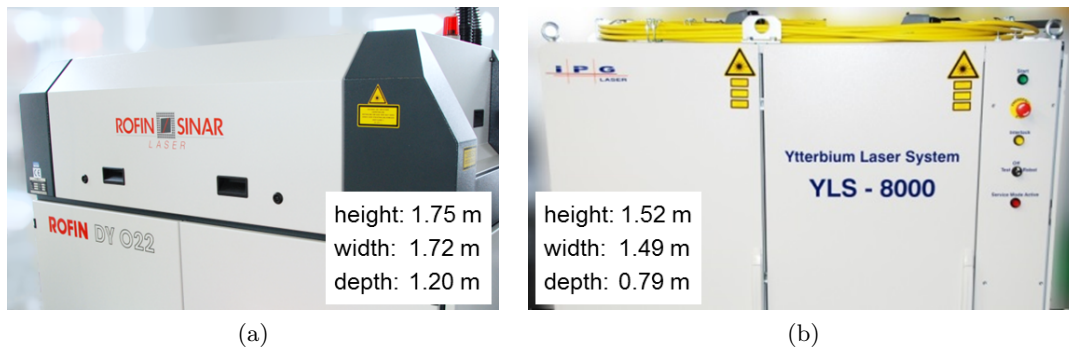


Figure 6.1.: Lasers used for the laser beam welding both approaches: Nd:YAG laser (a) and Yb fibre laser (b).

Table 6.2.: Summarized characteristics of the used laser systems for both approaches.

property	Nd:YAG laser	Yb fibre laser
maximum power [kW]	2.2	8.0
wavelength [ $\mu\text{m}$ ]	1.064	1.070
beam parameter product [mm mrad]	14.528	11.305
fibre diameter [ $\mu\text{m}$ ]	300	300
focal length [mm]	250	300
collimator length [mm]	200	150
laser spot diameter (in focus) [ $\mu\text{m}$ ]	366	746
Rayleigh length [mm]	4.63	24.554
irradiance distribution	Gaussian	top-hat

The wavelengths of both lasers are very similar so that it can be assumed that the interaction of the laser beam with the material is comparable, as described in Section 4.6.

The fibre laser possesses a higher beam quality in comparison to the Nd:YAG laser for the same fibre diameter of  $300\ \mu\text{m}$ . And due to the better focusability of the laser beam more energy is transferred to the material during welding, even if the same laser power would be available [98].

The differences in the beam shape of both lasers are shown in the results of the laser beam caustic measurement in Fig. 6.2. The beam of the Nd:YAG laser exhibits a very distinct hourglass shape (Fig. 6.2a). This means that the Rayleigh length is short. In contrast to that, the beam of the fibre laser shows a very large Rayleigh length (Fig. 6.2b). Thus, fibre laser welds are less affected by unintentional defocussing.

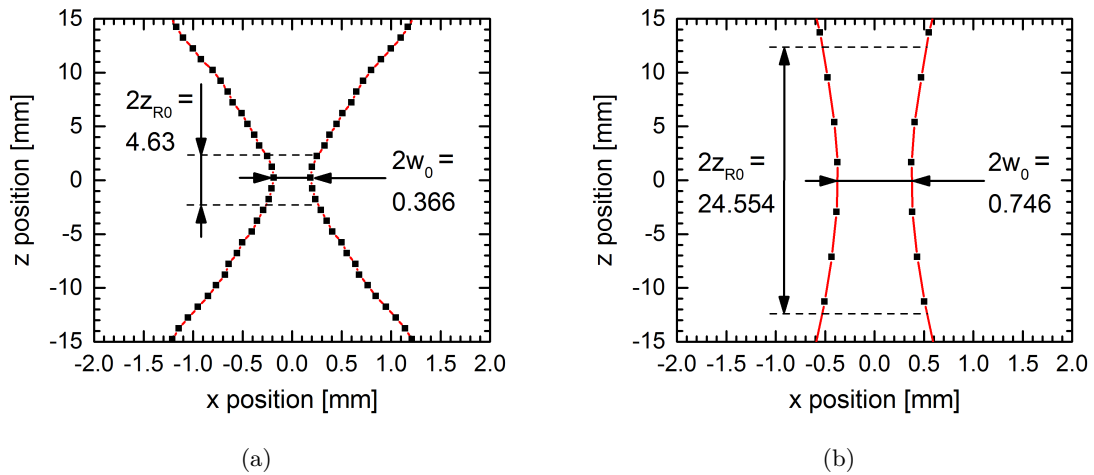


Figure 6.2.: Typical laser beam shape of the Nd:YAG laser (a) and the fibre laser (b).

The distribution of beam irradiance differs for each of the two laser types, as shown in Fig. 6.3. The Nd:YAG laser is characterized by a Gaussian-like distribution, for which the maximum irradiance is only reached at the centre of the beam. In contrast to that, the fibre laser provides a top-hat irradiance distribution, at which the maximum irradiance is kept constant at a very large area. This area almost corresponds with the cross sectional area of the laser beam so that the generation of a large and stable keyhole is enabled. By defocussing of the laser beam above the Rayleigh length the beam irradiance distribution changes drastically to a very inhomogeneous distribution, which deviates from the initial Gaussian or top-hat shape, as shown in Fig. 4.21 and explicated in Section 4.7. For this reason, larger defocussing is possible for used fibre laser without changing significantly the beam irradiance distribution.

Although helium gas is supposed to reduce the susceptibility to porosity [100], the reduction of the melt viscosity as well as the increase of the melt temperature may lead to a deterioration of the laser weldability. Thus, argon gas was used as shielding gas. The gas was supplied both from the front side by a dragging flat fan nozzle and from the root side with gas supply integrated in the clamping device, in order to provide a complete shielding of the melt pool during welding. Gas flow rates of 20 l/min (front) and 10 l/min (root) were chosen so that the shielding of the melt pool was sufficient, but without disturbance of the melt pool motion.

The conventional filler wire was supplied by a dragging wire feed. Thus, a constrained wire guidance by the joining edges of the sheets was enabled. The wire feed rate was chosen so that sufficient material was supplied to the melt. Too high feed rates may result in shadowing of the laser beam and also in insufficient melting of the added material for given welding parameter set. The vanadium foil required for the first approach was laser tack welded on the face of one of the sheets, in order to ensure the position of the foil during the entire

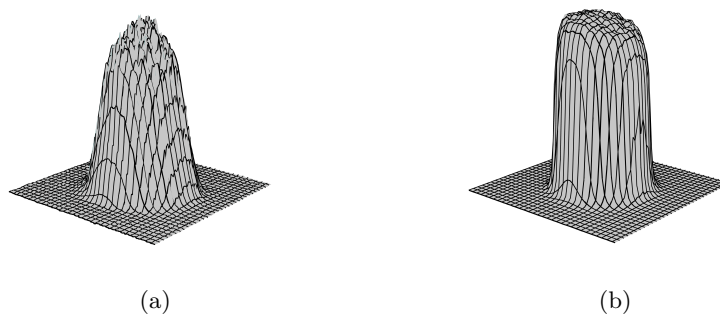


Figure 6.3.: Beam irradiance distribution of the Nd:YAG laser (a) and the fibre laser (b) in the focus position.

welding process. For assuring a good melting of the foil - with a considerable higher melting temperature - during welding, an exact positioning of the laser beam was required.

The laser beam welding configuration used for both approaches in this study is also depicted in Fig. 6.4.

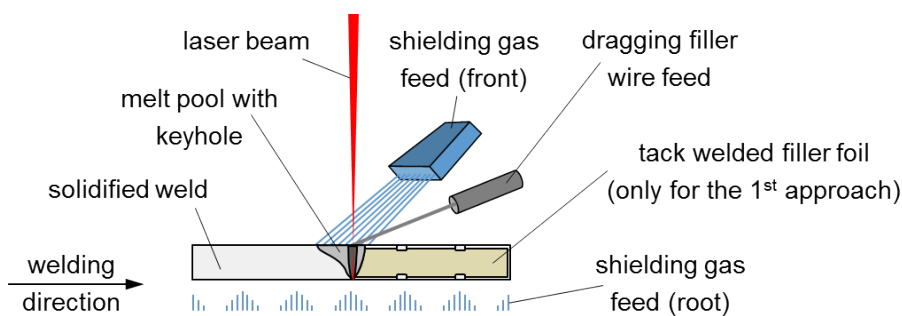


Figure 6.4.: Used configuration for laser beam welding of butt joints.

For adjusting and optimizing the welding results of each approach the following welding parameters were chosen to be varied: the laser power, the welding speed, the focal position and the feed rate of the filler wire (if intended to be used). It is supposed that these four welding parameters have the greatest influence on the weld results besides the factors intended to be used in the particular approach.

At the beginning a so-called 'worst-case' welding scenario was carried out, on the one hand in order to assess the initial laser weldability problems of the different Al-Zn alloys and on the other hand for comparative purposes with the two developed approaches. The scenario implied the use of a small beam diameter provided by the Nd:YAG laser and neither filler material nor shielding gas. Subsequently, a 'variation' welding scenario was carried out. In this scenario the capability of the welding parameter variation for improving the weldability was demonstrated for both laser systems. And finally the so-called 'enhanced' welding scenario for each of the approaches was carried out, which represented the optimized weld results. Therefore, the optimized welding parameters were determined for each of the approaches. The characteristics of each of the welding scenarios are summarized in Table 6.3. The welding parameter derived in this optimization process are given in Table A.1 in the Appendix A.3.

Table 6.3.: Summarized characteristics of the different welding scenarios.

scenario	Nd:YAG laser	Yb fibre laser	filler material	shielding gas
'worst-case'	X		w/o	w/o
'variation'	X		w/ and w/o	w/
'enhanced' (1 <sup>st</sup> approach)	X		w/	w/
'enhanced' (2 <sup>nd</sup> approach)		X	w/ and w/o	w/

### 6.3. Experimental procedures

In order to determine the properties of the laser beam welded joints diverse non-destructive and destructive testing methods are utilized. The benefit of non-destructive testing (NDT) lies in its ability to detect outer and inner discontinuities, to measure dimensions and to assess material characteristics without destructing the welded part. All methods used in this study are explained in the following.

#### 6.3.1. Analysis of the welding behaviour

The welding behaviour in matters of plasma plume formation and characteristics during the laser beam welding process was observed with the help of the high-speed camcorder JVC GC-PX100BE with a frame rate of up to 500 fps. The camera was mounted at a fixed distance to the incident position of the laser beam. Single photographs were extracted from the resulting video sequences.

#### 6.3.2. Temperature measurement

The transient temperature distribution during the laser beam welding of the butt joints was determined with the help of eight type K thermocouples and the data acquisition system HBM MGCPlus equipped with HBM ML801B multi channel modules. The sampling rate used for the measurement of the temperature was 100 Hz.

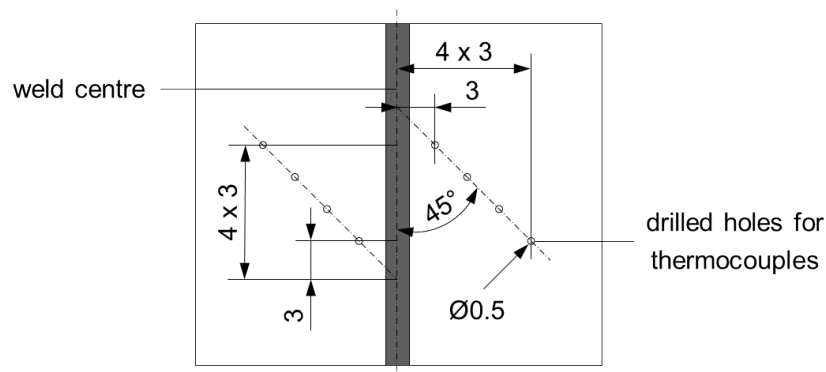


Figure 6.5.: Arrangement of the thermocouples for the measurement of the transient temperature distribution during laser beam welding.

The arrangement of the thermocouples in the specimen to be welded is depicted in Fig. 6.5. The used angular arrangement of the thermocouples prevented mutual shadowing during

the heat transfer. The arrangement was positioned in the middle of the specimen in order to avoid unfavourable effects of heat accumulation at the edges of the specimen.

### 6.3.3. Hydrogen analysis

In order to assess the influence of hydrogen on the laser weldability, the initial hydrogen content (surface and bulk) of the Al-Zn alloys and filler material as well as the hydrogen content of the resulting weld seams was measured by the use of the hydrogen analyser Leco RH-402. The working principle of this device is hot gas extraction. Therefore, samples of the same size were extracted from the base materials and weld seams. For providing similar surface conditions as used for welding, the preparation of the base material samples by grinding and cleaning with alcohol resembled the preparation for laser beam welding. In this way the falsification of the measurements and the deterioration of the welds by oxide layers and surface contaminations were reduced to a minimum. For each sample a separate graphite crucible was used. The calibration of the system was performed using a gas dosing based on hydrogen, since solid standards containing a defined hydrogen content were not available. All measurements were repeated at least three times for determining the average.

### 6.3.4. Visual testing

Visual testing was employed to assess the outer appearance of the welds and to detect surface discontinuities with normal eyesight alone or with the aid of optical instruments [82]. For documentation purposes macro photographs from front and root side of the welds were taken, with a single lens reflex camera Nikon D80 equipped with a macro objective (SIGMA 105 mm F2.8 EX). Typical outer weld discontinuities detectable by visual testing are for example undercut, insufficient or excess penetration, deposit, spatter and cracks of large dimension (Section 4.10).

### 6.3.5. Radiographic testing

Radiographic testing was employed to detect subsurface or inner discontinuities of the welded joints non-destructively [82]. The radiographic testing was performed according to EN ISO 17636-1 [101]. The used test arrangement was appropriate for plane welds and single wall penetrations. A Seifert Isovolt 320/13 with a focal spot of 1.5 mm × 1.5 mm served as radiation source, which was located in front of the specimen. The radiation-sensitive film (Agfa Strucutrix D4 DW ETE) was located at the opposite side of the specimen. A lead backing was used to reduce back scattering. The used tube voltage was 44 kV and the tube current was 2.6 mA. The exposure time depended on the density of the used Al-Zn alloy and ranged from 5 to 6.5 min. After exposure the radiographic film was processed by an automatic processing unit (GE NDT S eco 5320/300). Furthermore, the film was also scanned with a high resolution film digitizer (GE FS50B), which met the requirements of DIN EN 14096-2 [102] for radiographic film digitisation. For final interpretation of the radiographic pictures a high resolution radiology display (NDSsi Dome E3cHB) was used. Moreover, the radiographic pictures were brightened digitally for improving the visibility discontinuities. Inner weld discontinuities, such as pores, cracks and inclusions, of a size  $\geq 80\mu\text{m}$  are generally detectable by radiographic testing. Only in-plane cracks with a small crack opening in thickness direction can not be detected due to the resulting undifferentiated contrast on the film.

A digital image analysis for the radiographic pictures of the 'worst-case' welds was performed. For this purpose the software Adobe Photoshop CS5 Extended was used. By adjusting the tonal range of the pictures the porosity and undercut as well as the excess of

penetration and spikes were visualised. After the calibration of the picture size, it was possible to measure the amount of both groups with the help of planimetry tool provided by the software.

### 6.3.6. Microstructural analysis

The assessment of the shape and the microstructure of the welds was done by optical microscopy (OM). For this purpose cross sections were extracted from the welded joints. After their cold mounting in the resin Demotec 30 of Demotec Metallografie, automated wet grinding and polishing with a Struers Tegramin-30 and silicon carbide abrasive paper (with grit sizes from 80 to 2500) was performed. The cross sections were etched with Dix-Keller's reagent in order to improve the visibility of the microstructure. In case of high amounts of Al-Mg in the weld zone Kroll's reagent was used for etching. The compositions of both etchants are specified in Table 6.4. The characterization of the microstructure was done with the help of a Leica DMI 5000 M microscope, which was equipped with a Leica DFC 450 camera. During the preparation of the specimens special attention was paid to minimize the thermal impact, which may have an influence on the resulting microstructure.

Table 6.4.: Composition of the used etchants for the metallographic analysis.

Dix-Keller's reagent		Kroll's reagent	
190 ml	distilled water	92 ml	distilled water
5 ml	nitric acid	6 ml	nitric acid
2 ml	hydrofluoric acid	2 ml	hydrofluoric acid
3 ml	hydrochloric acid		

A more detailed investigation of the microstructure of the welds was done with the help of scanning electron microscopy (SEM). The extracted cross sections of the welds were warm mounted in the conductive resin WEM REM of Schmitz Metallografie. The temperature during warm mounting did not exceeded 180°C. The sample preparation resembled the preparation for OM but without an etching of the specimen surface. A JEOL JSM-6490LV SEM system was used for this kind of investigation.

### 6.3.7. Phase analysis

The local chemical composition of the certain regions in the weld was determined by energy-dispersive X-ray spectroscopy (EDX). The above described SEM was equipped with a EDAX AMETEK EDX Si(Li) detector, which allowed EDX measurements of the SEM specimens. The evaluation of the obtained data was performed using the software EDAX GENESIS Spectrum and the corresponding database.

The chemical composition of surface deposits was measured with the same system. Due to accuracy problems during direct measurements on the specimen surface, the deposit was removed from the surface by an adhesive graphite backing foil, which was then glued on the specimen holder. Thus, it was possible to avoid a falsification due to the underlying material.

For the identification of the predominant phases in the base material as well as in the fusion zone of the welded joints quantitative X-ray diffraction (XRD) measurements were conducted. For this purpose a Bruker D8 Advance X-ray diffractometer using Cu-K $\alpha$  radiation was used. The scanning step increase of 0.02° was used within a scan range of  $2\Theta = 20^\circ - 90^\circ$ . For the identification of the phases the software PANalytical X'Pert HighScore in combination with the JCPDS database were utilized. The small scale specimens were extracted with the help

of a diamond wire saw in order to reduce the thermal influence during sampling. In case of the welded joints, the fusion zone was extracted by sawing along the fusion line.

### 6.3.8. Mechanical testing

The assessment of the local mechanical properties of the welded joints was done by the determination of the microhardness according to DIN EN ISO 6507-1 [103]. For this purpose the semi-automatic hardness testing device Shimadzu HVM-2000 was used with a test load of 1.961 N (HV0.2) and an indentation time of 10 s. The indentations were set at designated positions in the base material, the heat affected zone and the fusion zone.

The tensile testing of the base materials as well as of the welded joints were performed according to ISO 6892-1 [104]. For this purpose flat tensile specimens were extracted in rolling and transverse direction for the base materials and perpendicular to the welding direction for the welded joints. Only in case of the AA7034 base material round tensile specimens were used. The welded joints were tested in a milled condition, in order to eliminate the influence of the weld geometry in terms of undercut and excess of penetration. The testing machine SchenkTreibel RM100 was used for this investigation. A constant strain rate of 0.5 mm/min or 1.0 mm/min was applied for testing, whereas the elongation was measured contact-free with the help of the laser extensometer system Fiedler WS-160.

The formability of the welded joints was assessed by limit dome height (LDH) testing. For this purpose the servo-controlled hydraulic press ITC ServoPress 225 equipped with a hemispherical punch was used. The punch as well as the lower and upper die were heatable, which allow isothermal warm forming. Square specimens with a size of 300 mm × 300 mm were extracted from the base material and from the welded joints - with the weld seam in the centre of the specimen. In order to reduce the friction between the punch and the specimen, a Teflon foil was placed between both. The tests were performed at room temperature (RT) as well as at an elevated temperature of 230°C. The strain during the deformation process was measured contact-free with the help of the optical measurement system GOM ARAMIS by capturing and evaluating numerous stereo image pairs. Therefore, a stochastic pattern was applied on the specimen surface. A punch speed of 90 mm/min was used for all tests. For preventing a draw-in from the flanges during LDH testing, the specimens were clamped with a force of 300 kN.

In the framework of a preliminary study [105] further mechanical testing - in terms of fatigue and fatigue crack propagation - was conducted for the 'enhanced' 1 welds of PA734.

The fatigue tests were performed according to DIN 50100 [106]. For this purpose flat fatigue specimens with a continuous radius were extracted perpendicular to the rolling direction for the base material and perpendicular to the welding direction for the welded joints. The specimen surfaces were milled from both sides in order to avoid a falsification of the results by surface notches and other surface imperfections. The tests were carried out at room temperature on the servo-hydraulic and load-controlled vibration test machines RUMUL Testronic 100 kN with a 20 kN load cell and Schenck Hydropuls PSA with a 40 kN load cell. The used R-ratio was 0.1.

The fatigue crack propagation tests were performed according to ASTM E647 [107]. A horizontal servo-hydraulic fatigue testing machine of Schenck with a 25 kN load cell was used for testing at a constant load amplitude using a 10 Hz sinusoidal wave form and a R-ratio of 0.1. Compact tension specimens C(T)100 in T-L orientation were extracted from the base material and the welded joints. In case of the welded specimen the notch was positioned in the fusion zone. The specimen surfaces were polished in the vicinity of the potential crack path in order to facilitate the detection and measurement of the fatigue crack.

### 6.3.9. Corrosion testing

In order to assess the global corrosion behaviour of the welded joints a salt spray test (SST) was conducted according to ISO 9227 [108]. For this purpose the salt spray chamber Weiss SC450 was used to provide an all-side exposure with the corrosive medium - a 5% NaCl solution. The exposure to corrosive medium took place for 168 h (7 days) at a temperature of 25°C in the chamber. The welds were tested in the as-welded condition as well as in the milled condition, in which a layer of the front and the root side was removed by mechanical milling until any kind of surface imperfection was removed. By this, it was possible to investigate the influence of the surface condition - such as the presence of an oxide layer - on the corrosion behaviour. The extracted specimens had a size of 30 mm × 30 mm and were cleaned with alcohol prior to the salt spray testing in order to avoid influences by surface contaminations. After the salt spray testing the specimens were cleaned according to ISO 8407 [109] in a solution containing phosphoric acid (50 ml phosphoric acid in 1000 ml distilled water) for 10 min in an ultrasonic bath at approximately 30°C. In order to quantify the corrosion attack - in terms of the corrosion rate - all specimens were weighed before and after the testing. The corrosion attack was observed optically by visual inspection as well as by the investigation with a Tescan VEGA 3 SEM equipped with an IXRF EDX Si(Li) detector. In this regard, either back-scattered electron (BSE) or secondary electron (SE) imaging was used. The evaluation of the obtained EDX data was performed using the software IXRF Iridium Ultra and the corresponding database. By doing so, it was possible to determine the location of elements such as vanadium and the preferential corrosive attack on the specimen as well as to classify type and size of defects.

## 7. Proof of concept

In this chapter, the obtained results for the base materials and the welded joints of the various welding scenarios are presented and discussed in detail. With the help of these information it is possible to assess the effectiveness of the developed approaches. The relevance of the approaches for the industry is also discussed in this chapter.

### 7.1. Base materials

The properties of the different base materials were determined in order to record the initial state of the materials and to allow a comparison between base material and welded joints.

#### Hydrogen content

The average initial hydrogen content of the five Al-Zn alloys used in this study was with approximately 1.2 to 2.1 ppm very low. With increasing amount of Zn+Mg+Cu the hydrogen content was only slightly decreasing, as it can be seen in Fig. 7.1.

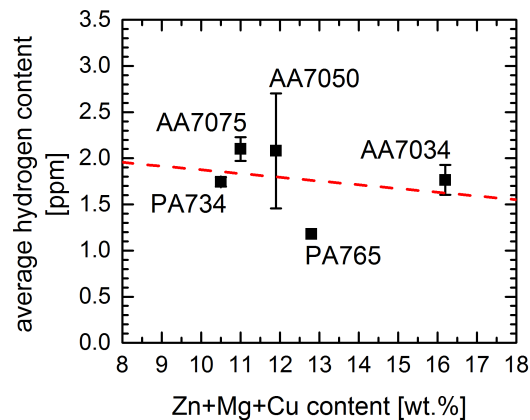


Figure 7.1.: Initial hydrogen content of the base materials (with error bars).

Although the magnesium content has the largest effect on the hydrogen solubility, the diminishing hydrogen content with increasing Zn+Mg+Cu content arose from the very high zinc content (especially in comparison to the magnesium and copper content), which was capable to compensate the unfavourable effect of the magnesium content, as indicated in Fig. 4.25b in Section 4.9.

The larger deviation of the hydrogen content of AA7050 could be caused by the presence of discontinuities in the bulk material, since the preparation of all samples and the measurement procedure were identical.

Due to the low initial hydrogen content of all investigated base materials, hydrogen could be excluded as the main reason for the observed porosity in the weld seams.

## Microstructure

The microstructures of the five base materials are shown in the macrographs of Fig. 7.2. The rolled alloy PA734 exhibited very large and elongated grains. The grains of the extruded alloy PA765 were also elongated but considerably smaller. The smallest grain size was observed for extruded alloy AA7034. The differences in the microstructure of the rolled alloys AA7075 and AA7050 were insignificant. Their microstructures were comparable to that of PA734, although their grains were less elongated and smaller in size.

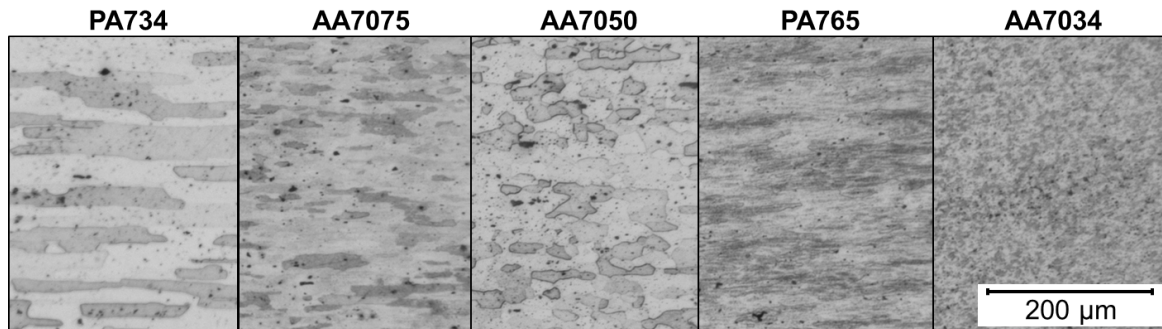


Figure 7.2.: Microstructure of the base materials (perpendicular to rolling/extrusion direction).

The differences in the microstructure were generated by the different processing of the base materials. The melt spinning of AA7034 prior to the extrusion enabled a very fast cooling of the melt so that a very fine microstructure resulted, as described by Hummert et al. [110]. Simple hot rolling and extrusion of cast ingots - as in case of all other alloys - generally results in a coarser microstructure with more elongated grains.

In Fig. 7.3 the results of the X-ray diffraction analysis of the base material AA7075-T6 are depicted. The peaks of the particular most important phases - namely Al, Zn and  $MgZn_2$  - were identified referring to the reference diffractograms, which are listed in the Appendix A.4. The base material in the as received, peak-aged condition T6 showed the typical weak peaks of the strengthening phase  $MgZn_2$  at  $2\theta \approx 40^\circ - 42^\circ$ . A slight over-ageing of this material (for example caused by a subsequent post weld heat treatment (PWHT) of the joints) resulted in an increase of the peak height. Since the peaks for the main alloying element zinc were very weak, no distinct peak at  $2\theta = 36.6^\circ$  for second main alloying element magnesium was observed.

The over-ageing of the Al-Zn alloy normally resulted in a coarsening of the  $MgZn_2$  phase, which was the reason for the increase of corresponding peaks after PWHT, as described by Zhao et al. [111].

## Mechanical properties

The mechanical properties of high-strength Al-Zn alloys are generally depending on their chemical composition and in particular on their Zn+Mg+Cu content, as described in Section 2.3. In Fig. 7.4 this linear dependency of the ultimate tensile strength and the microhardness becomes apparent for the used alloys in the peak-aged and over-aged condition. Only alloy PA765 showed a considerable higher strength and hardness as expected for this given Zn+Mg+Cu content and temper condition. By increasing the Zn+Mg+Cu content by one percent an UTS increase of approximately 21.3 MPa and a hardness increase of approximately 8.3 HV0.2 was achieved. In this context, the effect of micro-alloying and other special treatments was neglected.

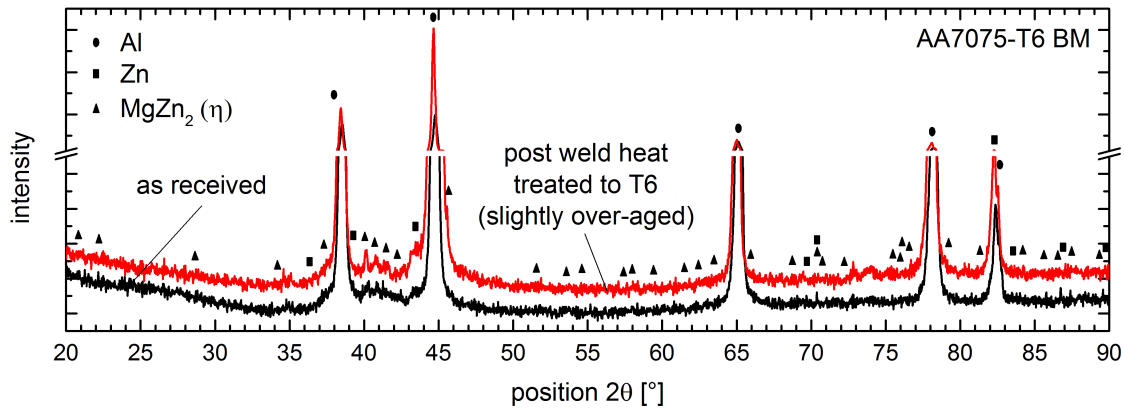


Figure 7.3.: XRD patterns of the base material AA7075-T6 in peak-aged and slightly over-aged condition.

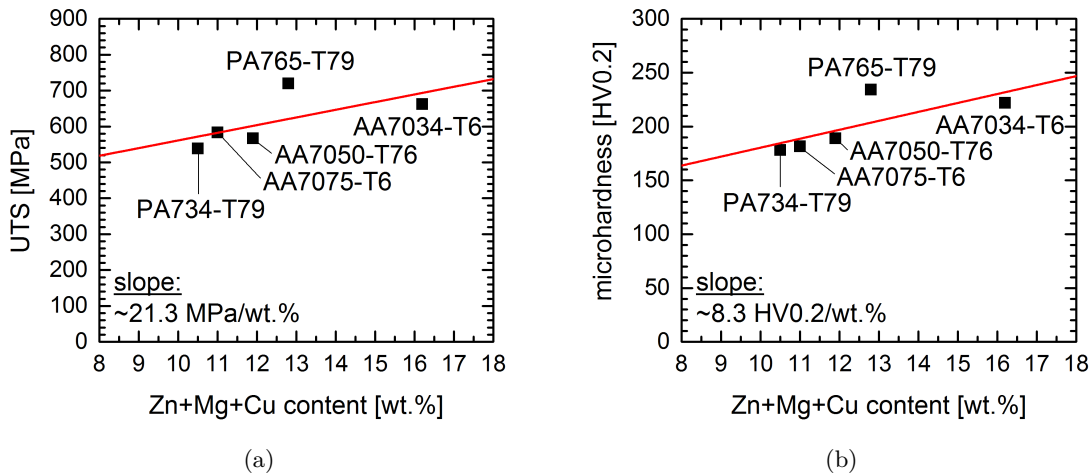


Figure 7.4.: Influence of the Zn+Mg+Cu content of the base material on the mechanical properties: ultimate tensile strength (a) and microhardness (b).

By comparing the stress-strain curves of the same alloys in Fig. 7.5 it can be seen that all alloys offered a good compromise of very high strength of up to 725 MPa and strain of up to 15.5%. This was in particular remarkable for the high-alloyed AA7034 in the peak-aged condition. In literature strengths of up to 800 MPa were reported [23]. Only the PA765 alloy - with the highest ultimate tensile strength - showed a limited strain of merely 6%.

The determined mechanical properties of the five Al-Zn alloys used in this study are summarized in Table 7.1.

In Fig. 7.6 the formability behaviour during limit dome height testing of AA7075-T6 is illustrated. The cold forming of AA7075-T6 at room temperature required a punch load of 124 kN. By performing the same forming procedure at a temperature of 230°C the required forming load was reduced by 53%. Furthermore, the punch displacement was increased by 14%.

Since high-alloyed Al-Zn alloys exhibited very high strengths, their formability at room temperature was naturally relatively low. Warm forming enabled an improvement of the forming behaviour due to recovery, which is generally characterized by a reduction of dislocation den-

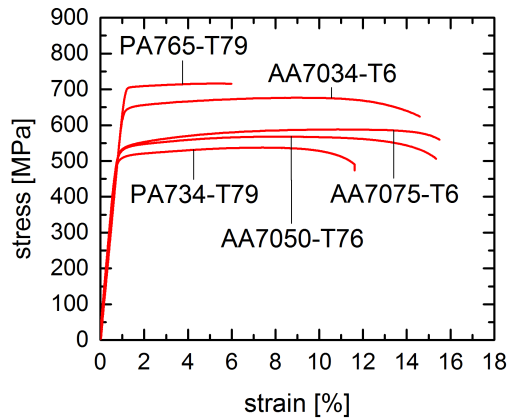


Figure 7.5.: Tensile properties (in rolling/extrusion direction) of the base materials.

Table 7.1.: Summarized mechanical properties of the base materials (in rolling/extrusion direction).

alloy	temper	YS [MPa]	UTS [MPa]	$\epsilon_f$ [%]	HV0.2 [-]
PA734	T79	505	532	11.6	178
AA7075	T6	533	588	15.5	182
AA7050	T76	527	568	15.3	189
PA765	T79	706	716	6.0	234
AA7034	T6	643	676	14.6	222

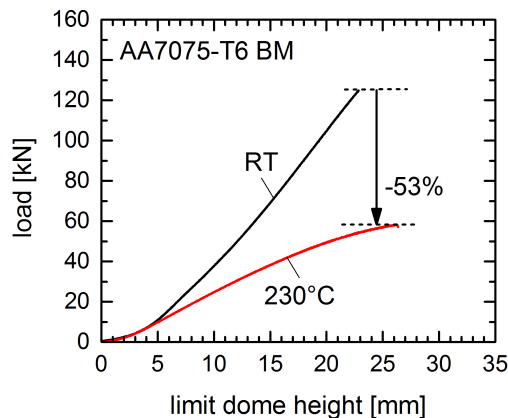


Figure 7.6.: Load-displacement curve during limit dome height testing of the base material AA7075-T6 at room temperature and 230°C.

sity and polygonisation at the expense of a higher manufacturing effort. It was demonstrated by Uffelmann [5] that warm forming of Al-Zn alloys at 230°C resulted in highest formability and a minimal strength reduction of 50 MPa, if the tempering lasted less than 5 minutes. Lower forming temperatures would cause an even lower loss of strength, but the formability would not be sufficient. Lower forming rates would also improve the forming behaviour, but the longer tempering would result in a greater loss of strength [5]. High forming temperatures, as for hot forming, lead to an improvement of the formability. However, hot forming

is always accompanied by a severe loss of strength and inferior surface qualities. The main difference between warm and hot forming is that the warm forming temperature is below the recrystallisation temperature range [112].

## 7.2. Worst case welding

The 'worst-case' welding scenario provides a survey of the typical weld defects occurring during laser beam welding with a conventional laser welding system and under worst possible conditions. This means that a small beam diameter provided by the Nd:YAG laser and neither filler material nor shielding gas was used for welding. Furthermore, the influence of the chemical composition of Al-Zn alloys on the laser weldability is demonstrated.

### Welding behaviour

Already during the laser beam welding of high-alloyed Al-Zn alloys it was possible to observe the process instabilities, which are generally resulting in weld discontinuities. In Fig. 7.7 photographs taken with the high speed camera are exemplarily shown. In the first picture the plasma plume above the keyhole was clearly visible. Within a time step of  $\Delta t = 0.02$  s this plume almost disappeared and then reappeared again with a different size within the next time step. The entire welding process was characterized by these kinds of fluctuations, at which the size of the plasma plume constantly changed or it even disappeared. These fluctuations were more severe as the periodic oscillation of the plume observed by Wang et al. [69] during the welding of other low-alloyed and weldable aluminium alloys. In addition, the fluctuations of the keyhole were accompanied by a high spatter tendency.



Figure 7.7.: Welding behaviour for a time interval of  $\Delta t = 0.08$  s during 'worst-case' welding of AA7075.

The observed fluctuations were generated by temporary vapour pressure drops due to the depletion of the volatile alloying elements zinc and magnesium in the aluminium alloy. Pure aluminium has a low vapour pressure, whereas the vapour pressure of zinc and magnesium is very high, as indicated in Fig. 4.11 in Section 4.4. Changing pressure conditions resulted in a collapsing of the keyhole due to the predominant keyhole pressure. Consequently, the plasma plume above the keyhole also disappeared. Alternatively, the shielding of the laser beam by the plume could be another explanation for the process instabilities, as explained in Section 4.2. Due to the high absorption, the energy of the laser beam did not suffice for keeping the keyhole stable.

### Outer appearance

The observed fluctuations during the laser beam welding process were also reflected in the outer appearance of weld seams, as it can be seen in Fig. 7.8. With increasing amount of Zn+Mg+Cu the outer appearance of the weld noticeably deteriorated. The amount and size of the spikes at the root side increased. In addition, an increase of spatter and deposit

predominantly at the root side was observed, whereas the amount of spatter appeared to decrease at the front side of the weld. The deposit at the weld root exhibited two shades of colour: white and brown to black (bottom row in Fig. 7.8). Furthermore, an inhomogeneous distribution of these two kinds of deposits was observed.

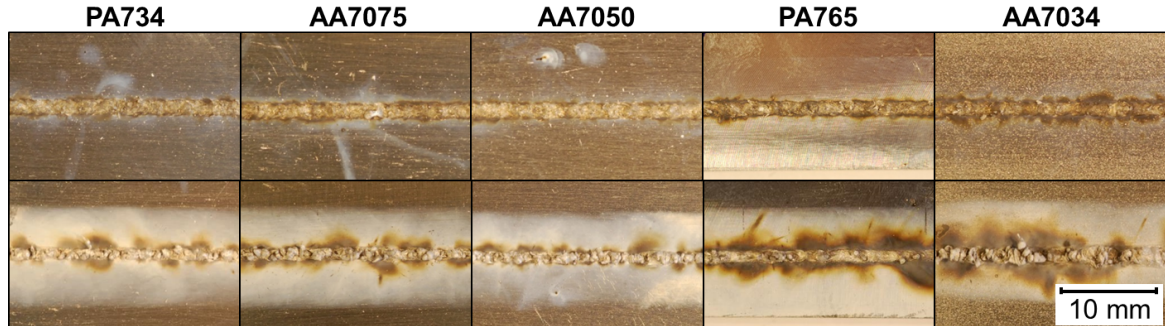


Figure 7.8.: Weld appearance from front side (top) and root side (bottom) of the 'worst-case' welds.

The increasing amount of spikes with increasing amount of Zn+Mg+Cu was caused by the reduction of surface tension and viscosity, mainly due to the high Mg content, as explained in Section 4.5. In this way, more material was expelled at the root side of the weld. This is also the explanation for the slightly reduced amount of spatter at the front side. Although the keyhole became even more unstable with increasing amount of Zn+Mg+Cu, most of the melt was moving in direction of the weld root, as illustrated in Fig. 4.15.

The inhomogeneous distribution of the deposits resulted from the keyhole instabilities during laser beam welding, which caused an irregular deflation of the vapour at the weld root. The detailed EDX analysis of the two deposits for welded PA765 - which exhibited very distinctive deposits - disclosed a differing chemical composition, as specified in Table 7.2. The main constituent of both deposits was zinc, which is plausible, since zinc has the lowest vaporisation temperature and highest vapour pressure. The dark deposit, which was in general in the vicinity to the fusion zone, had an almost 40% higher zinc content as the bright deposit. Although Mg is the second main alloying element with a likewise low vaporisation temperature, its portion in the deposits was relatively low (even lower than aluminium).

Table 7.2.: Chemical composition of the dark and bright deposits of a 'worst-case' weld of PA765.

element	brigh [wt.%]	multiple of Al	dark [wt.%]	multiple of Al
Al	32.42	–	14.49	–
Zn	56.19	1.73	77.99	5.38
Mg	11.39	0.35	7.52	0.52

For comparison purposes a second EDX analysis of the deposit of AA7075 was performed (Table 7.3). The measurement was done in the vicinity of the fusion zone, but as it can be seen in Fig. 7.8, the amount of dark deposit was considerable lower. Likewise, the zinc content in this deposit was lower, whereas the Mg content was higher. The measured copper content was low, as expected, since this element exhibits a considerable higher vaporisation temperature.

Table 7.3.: Chemical composition of the dark deposit of a 'worst-case' weld of AA7075.

element	'worst-case' [wt.%]	multiple of Al
Al	16.82	1.00
Zn	54.59	3.25
Mg	27.46	1.63
Cu	0.70	0.04
V	0.09	0.01

It has to be mentioned that the changes in deposit colour were mainly induced by the prevailing temperature (at a certain distance to the keyhole and plasma plume and their current condition), which resulted in a different degree of oxidation of the fine deposit particles during laser beam welding. Thus, the colours were not caused by the different chemical composition.

### Inner discontinuities

In Fig. 7.9 the radiographs - revealing the inner discontinuities - of the 'worst-case' welds are depicted. Surprisingly, the amount of porosity was very low, even in case of the high-alloyed AA7034. The observed weld seam discontinuities were characterised by an alternation of spikes (aggregation of material) and blow-holes (depletion of material). With increasing Zn+Mg+Cu content the amount of spikes increased (Fig. 7.10b), whereas the amount of blow-holes decreased (Fig. 7.10a). This can also be seen in the evaluation of the digital image analysis of the radiographs in Fig. 7.11. Solely in AA7034 a serve transversal crack - running from the fusion zone into the heat affected zone - was clearly visible.

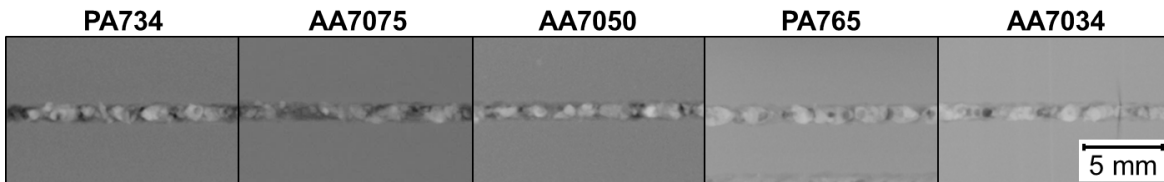


Figure 7.9.: Radiographs with typical inner discontinuities of the 'worst-case' welds.

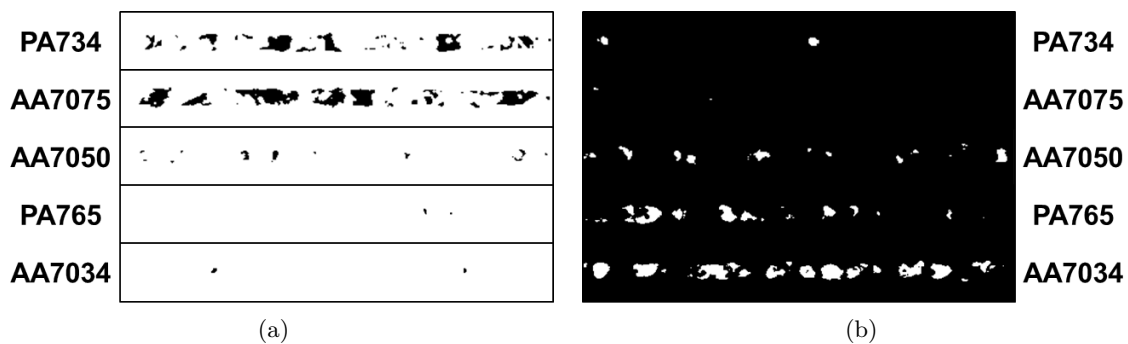


Figure 7.10.: Image analysis of the radiographs of the 'worst-case' welds: porosity and undercuts (a) and excess of penetration and spikes (b).

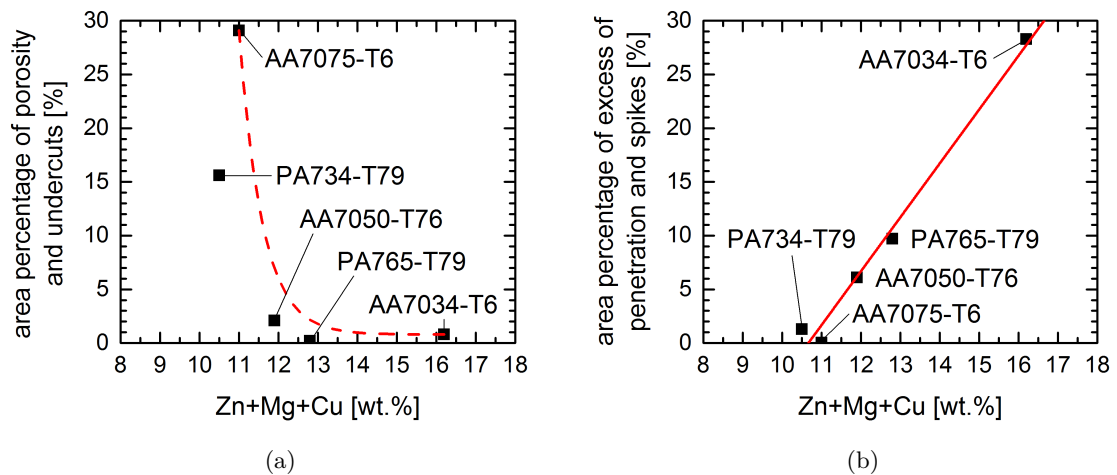


Figure 7.11.: Influence of the Zn+Mg+Cu content on the amount of porosity and undercuts (a) and excess of penetration and spikes (b) of the 'worst-case' welds.

The lack of porosity in the weld seams could be explained by the fact that most material was expelled at the root side of the weld. Furthermore, it was possible that pores - piling up in the weld root - could be obliterated on the radiograph by the high density of aggregated material in the weld root. The crack in AA7034 was identified as a solidification crack, due to its position in the fusion zone, as explained in Section 4.8. This kind of crack was caused by an unfavourable solidification range resulting from the chemical composition of the weld seam. Since this alloy had a very low copper content and higher magnesium content as PA734 - which should exhibit a higher hot cracking sensitivity, it was assumed that the crack resulted from an initial flaw in the solidified weld metal in combination with local welding-induced stress - aggravating the crack growth.

### Hydrogen content

The measured hydrogen content of the 'worst-case' fusion zone of AA7075 was  $1.92 \pm 0.26$  ppm. This value was even lower than for the base material with  $2.1 \pm 0.12$  ppm.

This low hydrogen content indicates that almost no hydrogen was introduced by the welding process itself. Due to the fact that most of the pores in the fusion zone and thus, also the hydrogen were expelled with the weld metal during the laser beam welding, a lower hydrogen content as for the base material may result.

### Microstructure

In the macrographs of Fig. 7.12 the poor weld seam quality was again clearly visible. All welds exhibited an undercut at the front side and an excess of penetration or spikes at the root side of the weld. In addition, the previous assumption that the pores are accumulating in the weld root, was confirmed. The fine grained alloys PA765 and AA7034 showed a distinct heat affected zone in the vicinity of the fusion zone. Furthermore, a severe cracking in the heat affected zone was observed for AA7034, which was already detected in the radiograph. On closer examination of the macrographs slight differences in the fusion zone width and size were identified, although identical parameters were used for welding.

Due to the fluctuations of the keyhole - collapsing and regeneration - during laser beam welding, the size and also shape of the keyhole underwent a permanent alteration. This

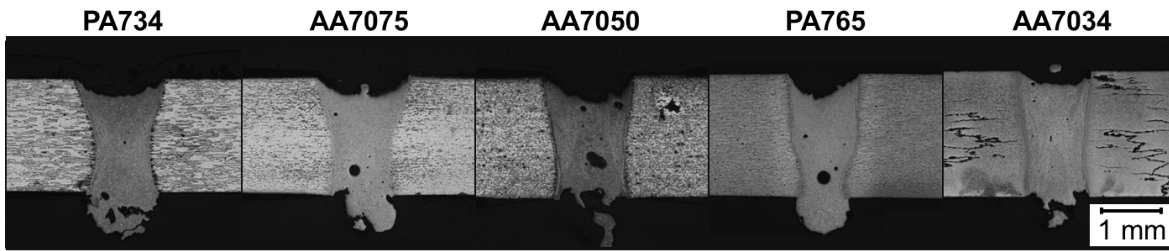


Figure 7.12.: Macrographs of the 'worst-case' welds.

dynamic behaviour of the keyhole was for example described by Kroos et al. [113] and Wei et al. [114]. Depending on the positions for the extraction of the specimens the fusion zone width could vary.

### Mechanical properties

By comparing the average microhardness of various 'worst-case' welds in Fig. 7.13a it becomes evident that the hardness of the heat affected zone was almost proportional to the initial hardness of the base material. The hardness drop in the heat affected zone increased with increasing amount of Zn+Mg+Cu from -10% for PA734 to -18% for AA7034. Although PA765 exhibited the highest initial hardness, the fusion zone of AA7034 possessed with 168 HV0.2 a higher hardness. Remarkably, the fusion zone hardness of AA7034 was comparable to heat affected zone hardness of the lower alloyed Al-Zn alloys such as PA734. The hardness drop in the fusion zone lay between -24 to -31%. Here, the highest degradation was observed for PA765-T79. A direct comparison of the hardness profiles of PA734-T79 and AA7034-T6, with a considerable higher Zn+Mg+Cu content, is given in Fig. 7.13b. Here, the local hardness dropped in the HAZ, due to the presence of cracks.

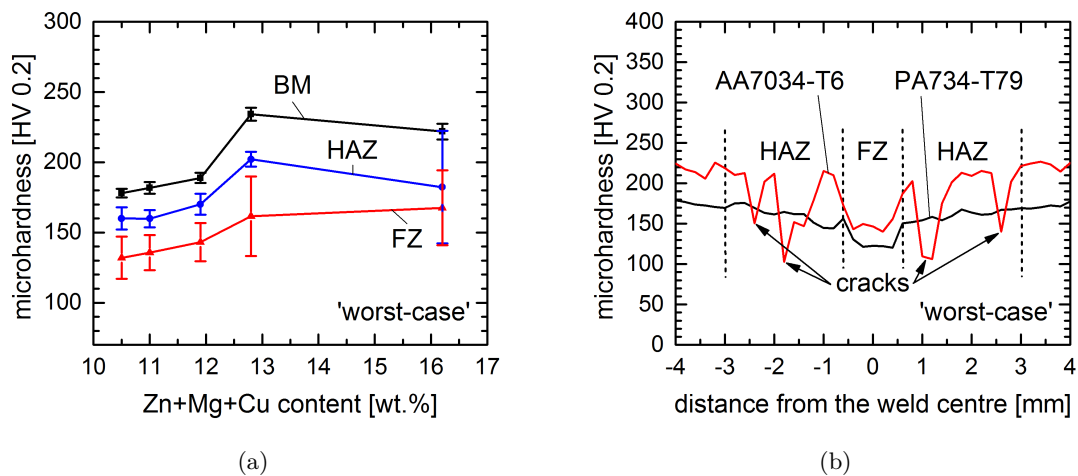


Figure 7.13.: Average microhardness of the 'worst-case' welds in different weld zones (a) and comparison of PA734 and AA7034 (b).

The hardness of the alloys with a very high Zn+Mg+Cu content deteriorated most by welding. These alloys had, as mentioned earlier, a well adjusted microstructure by alloying, processing and tempering. Due to heating and melting during the welding and slow and uncontrolled cooling after the welding this microstructure was changed or even destroyed. An

example for this could be the coarsening of precipitates in HAZ and the formation of dendrites in the FZ. Furthermore, the hardness in the HAZ and FZ could also be deteriorated by the presence of weld defects, as it can be seen for the HAZ of AA7034 in Fig. 7.13b.

### Corrosion behaviour

The visual inspection of the as corroded 'worst-case' specimens showed that the majority of the residues of the corrosive medium were found on the weld seam and in its vicinity, as it can be seen in Fig. 7.14. The most intense corrosion was observed after cleaning right below the adhered NaCl residues. In this regard, differences of the preferential corrosion sites were observed for the as welded and the milled specimens. In case of the as welded specimen corrosion predominantly took place in the heat affected zone in a distance of  $\geq 0.7$  to 1.3 mm, whereas the fusion zone showed only a slight attack. In contrast, the milled specimens showed the highest corrosive attack along the fusion line in a extremely narrow region. Additionally, a less intense corrosive attack was observed in the same region of the heat affected zone as for the as welded specimens. Furthermore, the weight loss due to corrosion was with 0.86% ( $\approx 0.02841$  g) more than 1.5-times higher for the milled condition as for the as welded condition with 0.54% ( $\approx 0.02665$  g).

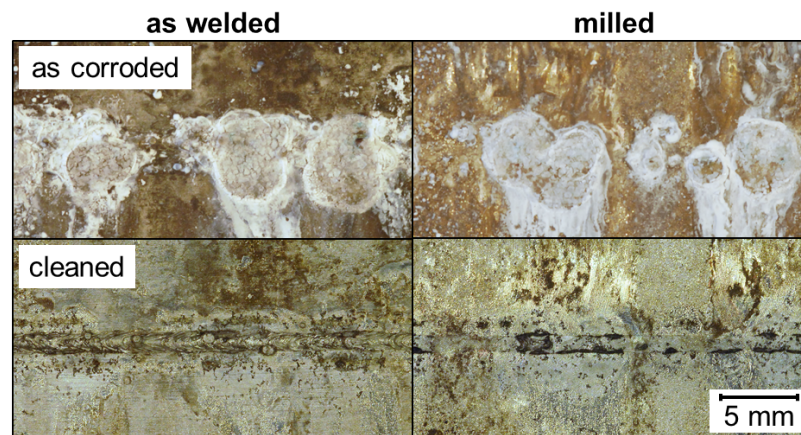
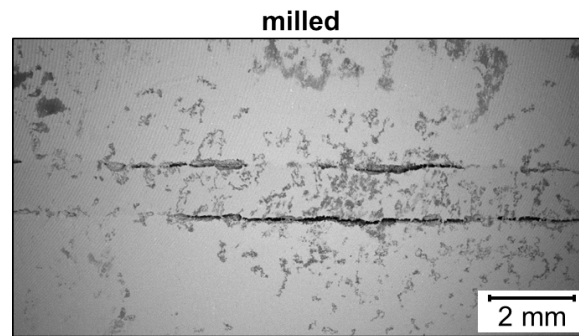


Figure 7.14.: Outer appearance of the as corroded (top) and cleaned (bottom) 'worst-case' welds in the as welded (left) and milled (right) condition.

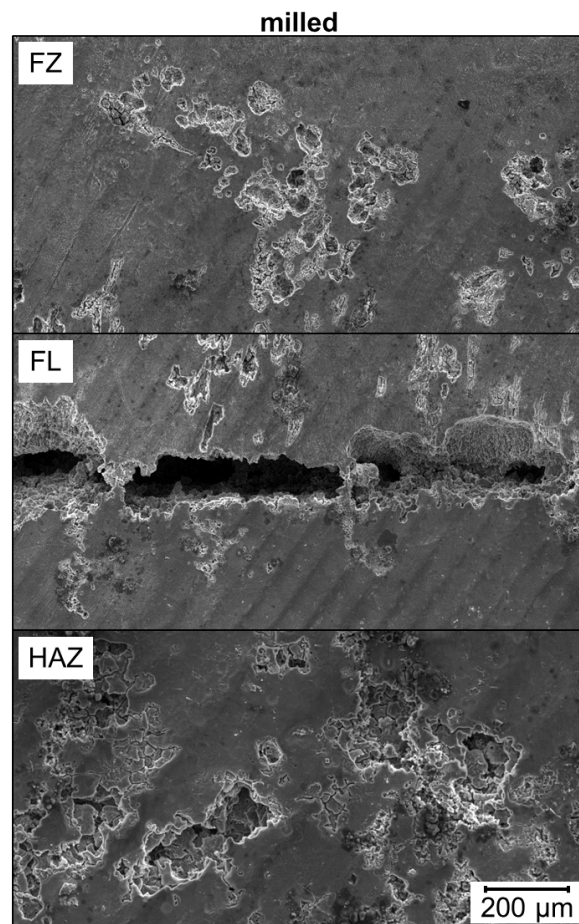
The higher corrosion rate of the milled specimen resulted from lack of a thick passive and protective oxide layer as for the as welded condition. Of course, directly after milling a new oxide layer was formed. But this layer is in general considerable thinner than the layer formed during welding. Elevated temperatures, as existing during welding, caused an increase in the growth rate of the oxide layer.

An overview as well as details of the corrosive attack for a cleaned milled specimen are shown in Fig. 7.15. The corrosion pits in the region of the heat affected zone appeared to be considerable deeper and larger in area as for the fusion zone of the same specimen. In addition, at the edges and in the close vicinity of these pits a preferential attack of the grain boundaries was observed.

The preferential corrosive attack along the fusion line, which is sometime also called knife-line attack (KLA), arose from galvanic effects in the partially melted zone. In this zone low melting eutectics in the grain boundaries were predominantly melted so that locally higher corrosion potential between precipitate free zones (PFZ) - a region adjacent to the grain boundary, which were depleted of precipitates - and grain boundaries resulted. Due to the



(a)



(b)

Figure 7.15.: Corrosive attack of a 'worst-case' weld of AA7075 in the milled condition: weld overview (BSE) (a) and weld details (SE) of the fusion zone, the fusion line and the heat affected zone (b).

narrow nature of the PMZ the intergranular corrosion was quickly transforming to a severe crevice corrosion. Consequently, a very deep corrosion induced crevice resulted. The reason, why this kind of corrosive attack was observed only in the milled condition, lay again in the fact that as welded condition exhibited a protective oxide layer in this region.

The differences in the corrosive attack of the FZ and the HAZ were mainly caused by their different chemical composition and temper condition. Each region in the HAZ experienced a certain peak temperature, heating and cooling rates so that locally different microstructures were resulting. A narrow region in the HAZ became more anodic in comparison to the unaffected base material, which resulted in a preferential attack in this region, as indicated earlier in Section 2.4. It could be concluded from the outer appearance of the corrosive attack in the HAZ that at the beginning pitting occurred, which is a very localized attack caused by very specific microstructural features. Later the pits became deeper and the growth rate increased [22]. The presence of local grain boundary attack in the HAZ indicates that there was a mixture of pitting and intergranular corrosion in this region. In the FZ microsegregation occurred during solidification so that the local galvanic potential was changed and only local pitting occurred.

### 7.3. Variation welding

The 'variation' welding scenario allows a demonstration of the limited capability of welding parameter variation for improving the weldability for a conventional laser welding system. For this welding scenario only one alloy - namely AA7075 - was used. As filler material a conventional Al-Mg filler wire was used.

#### Outer appearance

By sole variation of the laser beam welding parameters it was impossible to significantly improve the outer appearance of the welds - in comparison to the 'worst-case' welds. Typical weld appearances were identified according to the used welding parameter, as shown in Fig. 7.16. The obtained weld seams exhibited either an undercut or an excess of weld metal at the weld front. In case of high line energies the weld metal was sagging to the weld root or was expelled excessively at front and root side of the weld so that an undercut at the weld front was formed. By using a higher amount of filler wire this undercut could be filled with the additional material. Furthermore, three types of weld roots were obtained. In case of too low line energy, the sheets were not completely penetrated. In contrast to that, too high line energy resulted either in the sagging of the weld metal for low welding speeds or in the formation of spikes at the weld root for high welding speeds. By the use of filler wire the appearance of the weld root could not be changed.

The explanation for this unfavourable weld appearance is similar to that of the 'worst-case' welds. The only difference is that sagging occurred when the melt pool was too large so that most of the material was moving to the weld root due to the gravitational force, whereas the so-called spiking occurred in case of small melt pools, where most of the material was pushed out of the weld due to the high and unstable pressure in the keyhole. The phenomenon was already described in the Chapter 4 in Fig. 4.15.

#### Inner discontinuities

Although some of the weld seams might had a slightly better outer appearance, all of them exhibited a severe porosity, as it can be seen in Fig. 7.17. The highest porosity was observed

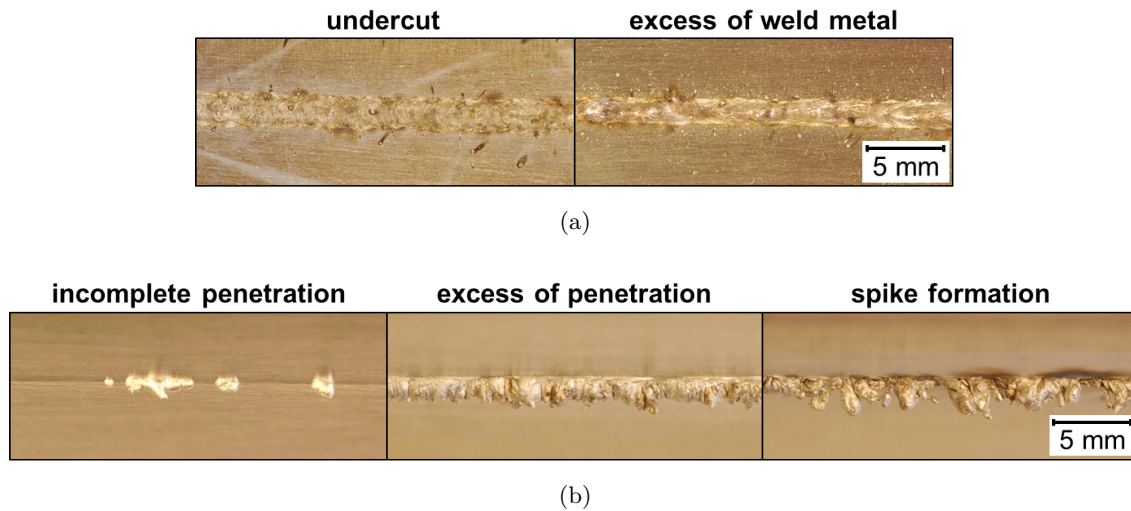


Figure 7.16.: Typical types of weld front (a) and weld root (b) appearances for the 'variation' welds of AA7075 (welded with different welding parameters).

for the incomplete penetrated and the sagging welds. In contrast, the welds with severe spiking formed rather blow-holes.

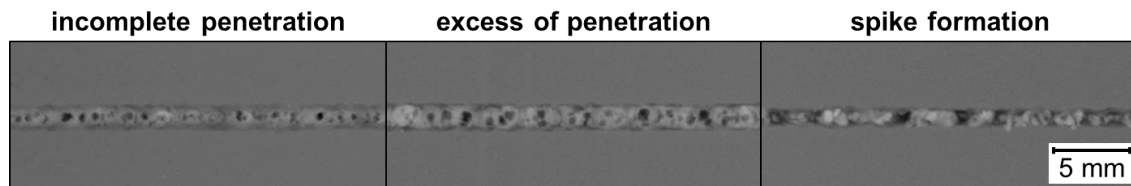


Figure 7.17.: Radiographs with typical inner discontinuities of the 'variation' welds of AA7075.

The higher porosity of the incomplete penetrated and sagged welds could be explained by the fact that in both cases the keyhole was closed at the root side so that the degassing to that side was impossible. The pores of the welds with spikes were either expelled with the weld metal or were hidden in the weld root, as explained earlier.

### Hydrogen content

The hydrogen content of a 'variation' fusion zone solely welded with the Al-Mg filler wire AA5087 lay at  $3.93 \pm 2.18$  ppm. This was an increase of +87% in comparison to the base material AA7075 and +105% in comparison to the 'worst-case' weld.

The increased hydrogen content was assumed to result from the added Al-Mg filler wire AA5087. As shown in Fig. 4.25b in Section 4.9, the solubility of hydrogen in aluminium increased with the Mg content. Moreover, the higher surface-to-volume ratio of the wire in combination with the limited possibility to efficiently remove an existing surface oxide layer implied the input of hydrogen to the weld metal. The hydrogen measurement of the filler wire material - in the as used condition - resulted in a value of  $4.43 \pm 0.37$  ppm, which almost correlated with the increase for the 'variation' weld seam. The radiograph and the macrograph of the selected 'variation' weld - for comparison purposes - are shown in Fig. 7.18.

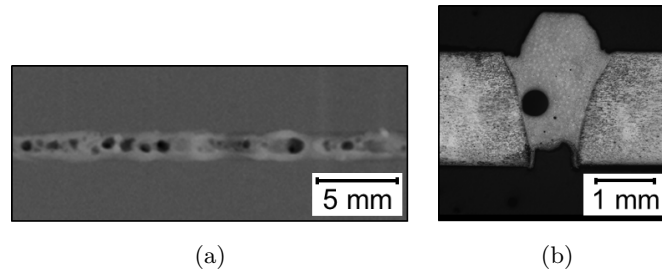


Figure 7.18.: Radiograph (a) and macrograph (b) of the selected 'variation' weld of AA7075.

### Microstructure

Typical macrographs of the 'variation' welds are shown in Fig. 7.19. It can be seen that all of the weld seams possessed large pores. In case of the welds with spikes microporosity was additionally observed. Furthermore, the undercut or excess of weld metal at the weld front as well as the sagging or spiking at the weld root could be seen. The welds differed not only in the outer appearance but also in width and shape of the fusion zone.

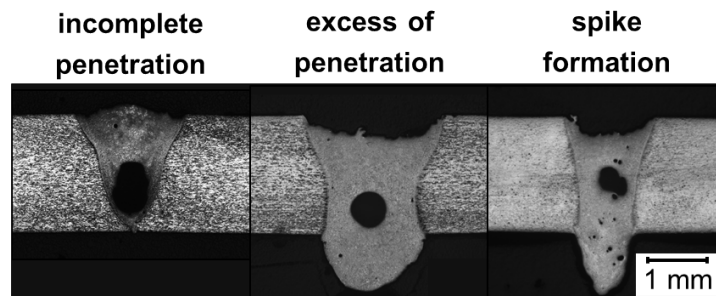


Figure 7.19.: Typical macrographs of the 'variation' welds of AA7075.

The differences of the fusion zone size and shape were predominantly arising from the parameters used for welding and only negligibly from fluctuations of the keyhole. Even similar line energies could result in different melt pool and keyhole dimensions, as described in Section 4.3.

### Mechanical properties

For comparative purposes only the AA7075 'variation' weld welded with filler wire and exhibiting spikes at the weld root was chosen for the mechanical testing. It was welded with a laser power of 2.0 kW, a welding speed of 3500 mm/min, a defocussing of 0 mm and feed rate of 3500 mm/min for an AA5087 filler wire.

From the graphs for the microhardness in Fig. 7.20 it could be deduced that there was almost no difference between the results of the 'worst-case' welds and the chosen 'variation' weld. The hardness drop for AA7075-T6 in the fusion zone with -18% and in the heat affected zone with -4% was almost the same.

The addition of the Al-Mg filler wire AA5087 did not lead to an improvement of the hardness in the fusion zone, since this alloy belonged to the low-strength and non heat-treatable alloys. But it also did not lead to a deterioration of the hardness, due to the comparatively low amount of wire material in the melt.

The tensile testing of the same 'variation' weld resulted in a reduction of the ultimate tensile strength of approximately 40% in comparison to the base material. In addition, the ductility

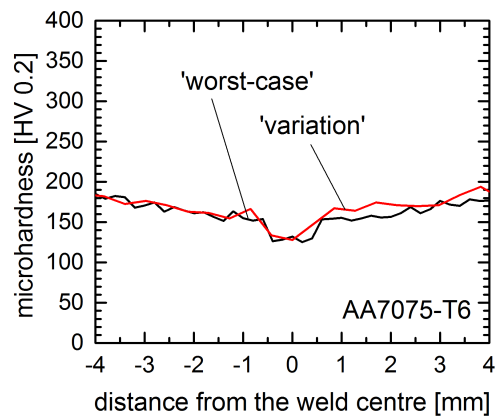


Figure 7.20.: Microhardness of the selected 'variation' weld welded with filler wire.

of the welded joint was with -95.7% also significantly reduced.

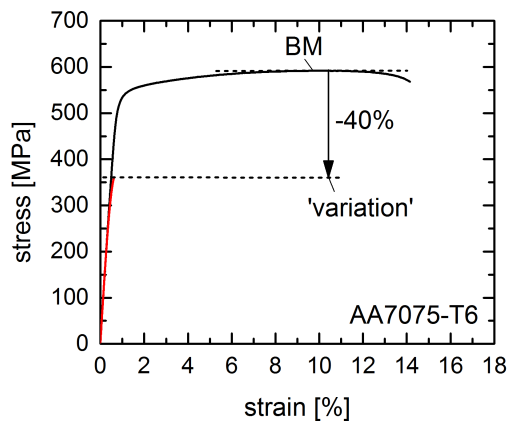


Figure 7.21.: Tensile properties of the selected 'variation' weld welded with filler wire.

In the fracture surface of the 'variation' weld tensile specimens the presence of porosity was clearly visible (Fig. 7.22). As a result, the crack was initiating and running within the fusion zone. This finally resulted in a very uneven fracture surface.



Figure 7.22.: Fracture surfaces of the selected 'variation' weld tensile specimen.

The failure of the specimen in the fusion zone during tensile testing was caused by the presence of porosity, which generally results in local strain concentration in this regions due to the reduced cross-sectional area. Another reason was the strength undermatching already revealed through the measurement of the microhardness.

## Corrosion behaviour

The corrosion behaviour of the 'variation' welds was also very similar to that of the 'worst-case' welds, although an Al-Mg filler material was added. This can be seen in the micrographs in Fig. 7.23. Again, the predominant corrosive attack of the milled specimens took place in the PMZ between the fusion zone and the heat affected zone. The weight loss due to corrosion was with 0.56% in the as welded condition and with 0.88% in the milled condition was only slightly higher than for the 'worst-case' welds.

Obviously, the addition of an Al-Mg filler material to the weld metal had only a minor effect on the corrosion behaviour. Although the main precipitate of Al-Mg alloys -  $\text{Al}_8\text{Mg}_5$  ( $\beta$ ) - is anodic in comparison to the base material and may deteriorate the corrosion behaviour, this effect was very limited due to the small amount of filler material in the fusion zone and the small dimensions in comparison to the base material. Nevertheless, the slight increase of the corrosion rate could be explained by this.

## 7.4. Enhanced welding: First approach

The 'enhanced' welding scenario of the first approach allows a demonstration of the capability of using vanadium foil as additional filler material for improving the laser weldability of different high-alloyed Al-Zn alloys using a conventional laser welding system.

Some parts of this section - concerning weldability improvement and mechanical properties (formability, fatigue and fracture) - were already published by the author [115–118].

### Optimization

In the framework of a preliminary study [105] the influence of foil thickness on the weld results of alloy PA734 was investigated. It can be seen in Fig. 7.24 that with increasing thickness of the foil the amount of undissolved foil increased for constant welding parameters. Without vanadium the weld tended to exhibit severe porosity and discontinuities due to process instabilities. For a foil thickness of 40  $\mu\text{m}$  the positive effect on the process stability and the avoidance of porosity was already visible. Thicker foils ( $\geq 250 \mu\text{m}$ ) also prevented the formation of pores, but at the same time the weld became discontinuous again.

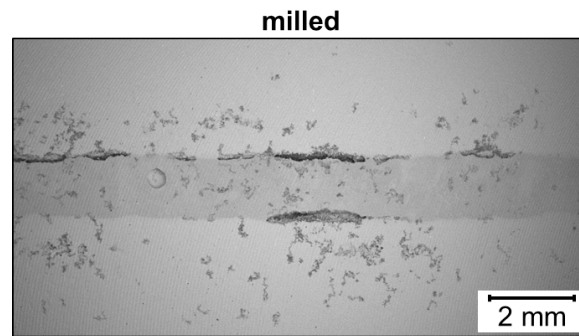
Furthermore, the complete melting and dilution of a large foil thickness required a higher line energy - the ratio of laser power to welding speed - otherwise a lack of connection between the foil and the sheet material occurred, as shown in Fig. 7.25.

In order to achieve sufficient melting and dilution of the foil during welding with the Nd:YAG laser with a maximum laser power 2.2 kW, a foil thickness of 40  $\mu\text{m}$  was chosen. The amount of filler wire fed during welding was also limited by the maximum laser power, since more energy was required for melting the additional material. In this regard, too low welding speeds should be avoided, because they generally result in a large heat input to the material due to the high thermal conductivity of aluminium - as shown in Fig. 4.6a - and hence in an increased degradation of the mechanical properties.

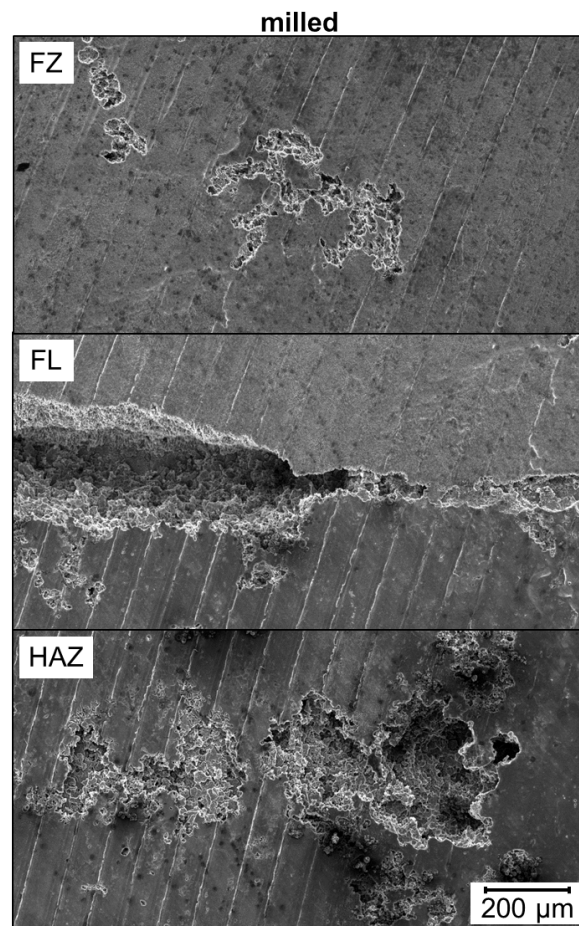
It turned out that a laser power of 2.0 kW, a welding speed of 3500 mm/min, a defocussing of 0 mm and a filler wire feed rate of 3500 mm/min were optimal for melting the vanadium foil and thus for improving the laser weldability. In the following the welding parameters of this approach will be also specified as the 'enhanced' 1 approach.

### Welding behaviour

The 'enhanced' welding of the first approach exhibited a completely different process behaviour in comparison to the 'worst-case' welding. During the entire welding process only



(a)



(b)

Figure 7.23.: Corrosive attack of the selected 'variation' weld of AA7075 in the milled condition: weld overview (BSE) (a) and weld details (SE) of the fusion zone, the fusion line and the heat affected zone (b).

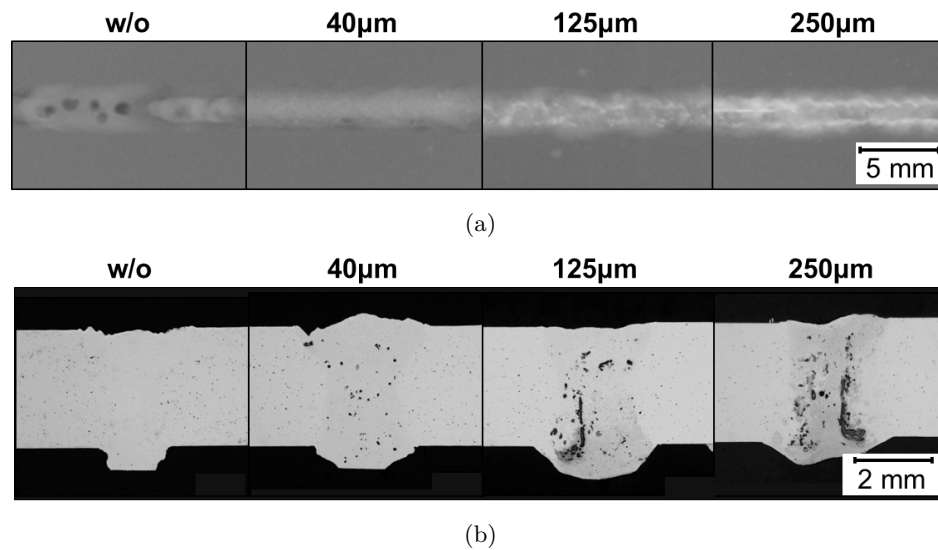


Figure 7.24.: Influence of the vanadium foil thickness for constant welding parameters ( $P_l = 3$  kW,  $v = 1800$  mm/min and  $v_w = 3600$  mm/min) on the weld results of PA734: radiographs (a) and macrographs (b) (referring to Iwan [105]).

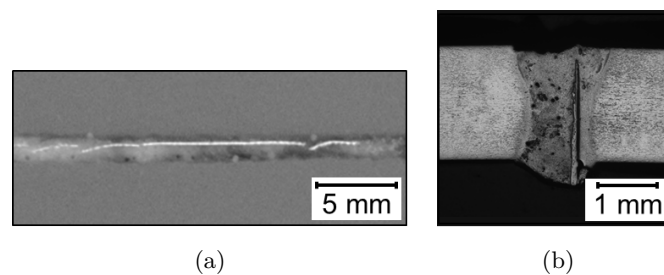


Figure 7.25.: Radiograph (a) and macrograph (b) of a joint with insufficient melting and dilution of a  $250 \mu\text{m}$  vanadium foil in AA7075 welded with a too low line energy ( $P_l = 2$  kW,  $v = 3500$  mm/min and  $v_w = 2500$  mm/min).

slight and almost periodic oscillations of the plasma plume were observed - comparable to the observations described by Wang. et al. [69]. However, the plume never completely disappeared, as it was observed for the 'worst-case' weld. This can be also seen in Fig. 7.26. In addition, the amount of spatter during welding was slightly reduced and seems to be more homogeneously distributed.



Figure 7.26.: Welding behaviour for a time interval of  $\Delta t = 0.08$  s during 'enhanced' 1 welding of AA7075.

The different process behaviour arose from the beneficial effect of vanadium on the process stability. The comparatively high amount of vanadium - especially in comparison to the both

alloying elements zinc and magnesium - in the fusion zone helped to stabilize the pressure conditions in the keyhole, as indicated in Fig. 4.11 in Section 4.4. This resulted in a constant vaporisation rate and thus in an almost constant plasma plume above the keyhole. Due to the use of shielding gas during welding no negative effect of absorption by the plume was directly observed. But in case of an existing plume shielding, the effect appeared to be very small and constant during the whole welding process.

### Transient temperature distribution

Fig. 7.27a shows the transient temperature cycles measured during the 'enhanced' welding of the first approach at different distances to the centre of the fusion zone. In Fig. 7.27b the corresponding peak temperatures of the 'enhanced' 1 welding are compared to that of the 'variation' welding. Both welding scenarios exhibited almost the same temperature field. However, the 'enhanced' weld showed a slightly lower average peak temperature - with a large scatter range - at a distance of 3 mm to the weld centre, although the size of the fusion zone was slightly larger for the 'enhanced' weld, as it can be seen in Fig. 7.27c.

The slightly lower temperatures in the vicinity of the 'enhanced' welds were resulting from the lower temperature conductivity of the weld metal due to the use of a vanadium foil as additional filler material. This narrow area of elevated temperatures during the laser welding of vanadium is also illustrated in Fig. 4.5 in Section 4.3. Moreover, some of the introduced laser energy was needed for melting the additional material. Thus, less energy was available for the heating of surrounding material of the melt pool.

### Outer appearance

The favourable effect of vanadium on the laser weldability was also reflected in the outer appearance of the welds (Fig. 7.28). The weld seams of all Al-Zn alloys showed a very uniform appearance - especially in direct comparison to the 'worst-case' welds in Fig. 7.8. At the root side no excess of penetration or spikes were formed. Instead, uniform flow marks were observed. Even the deposits of all welds appeared to be more uniform.

The absence of the excess of penetration as well as the spikes at the weld root could be explained by the high surface tension and viscosity of vanadium and thus also of the resulting melt pool. Furthermore, the improved keyhole stability by the use of vanadium restrained the discontinuous expulsion of weld metal. In this way, the amount of spatter was also significantly reduced.

The detailed EDX analysis of the deposits of the 'worst-case' and 'enhanced' welds disclosed comparable results (Table 7.3 and 7.4). From this it could be concluded that the addition of a vanadium foil and an Al-Mg filler wire did not lead to a considerable change of the portions of the elements in the deposits. Only small amounts of vanadium were vaporised during the welding process. The only change observed was an overall colour changing of the deposit to darker shades.

The colour change of the deposits predominantly resulted from the different temperature conditions during laser welding, but not by the negligible change of the chemical composition. The total amount of deposit could not be quantified with the available methods, but from the appearance it could be assumed that the amount of deposit was slightly reduced. This could be explained by the fact that shielding gas was supplied from top and root side, in contrast to the 'worst-case' welds.

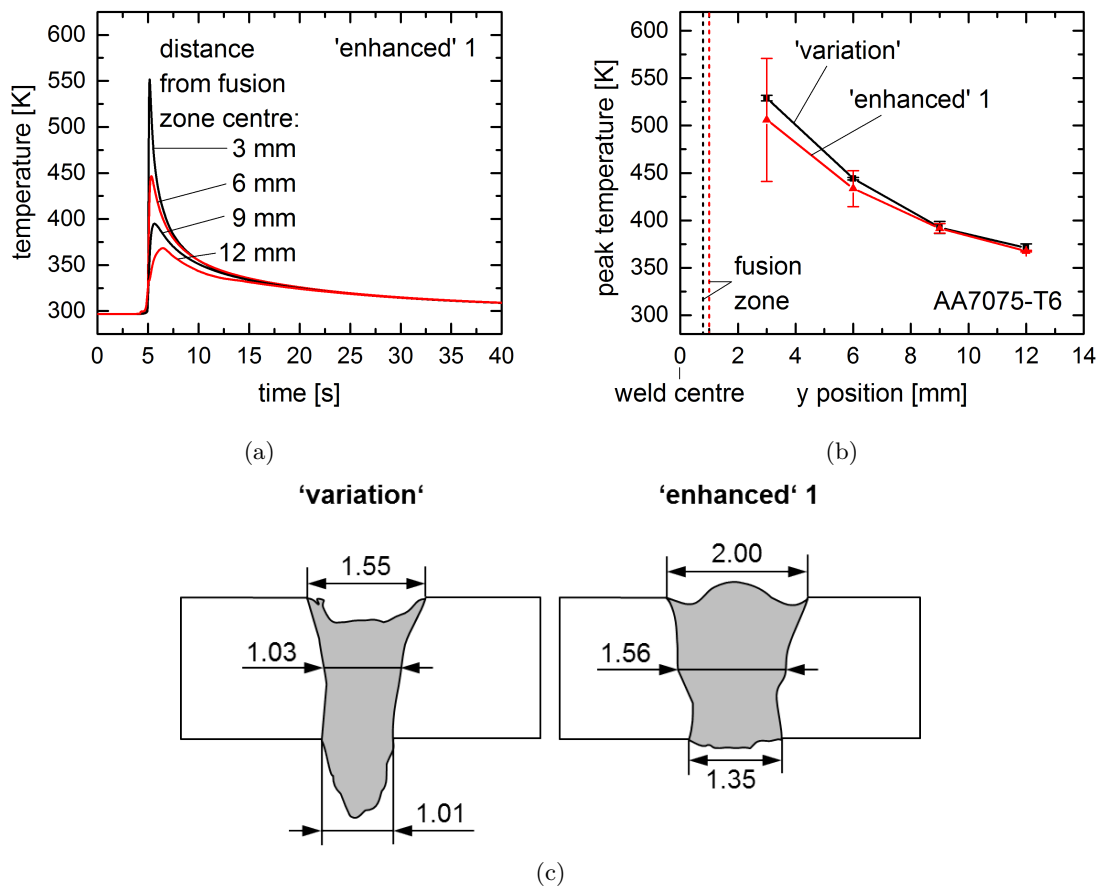


Figure 7.27.: Transient temperatures (a), peak temperatures at different distances to the fusion zone centre (b) and the resulting fusion zone dimensions (c) during the 'enhanced' 1 welding of AA7075.

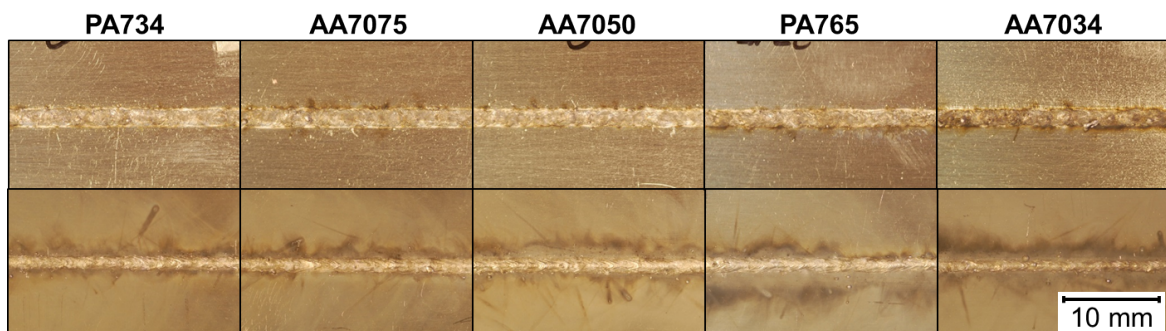


Figure 7.28.: Weld appearance of the front (top) and root (bottom) side of 'enhanced' 1 welds.

### Inner discontinuities

The radiographs in Fig. 7.29 demonstrate that the amount of porosity was considerably reduced for all Al-Zn alloys by the use of vanadium as additional filler material. Only some very small residual porosity was observed. Although, most of the welds exhibited a very homogeneous weld seam, some residual unmelted or undiluted vanadium foil - visible as higher dense material - was detected in some of the welds. However, there was no dependency

Table 7.4.: Chemical composition of the deposit of the 'enhanced' 1 weld of AA7075.

element	'enhanced' [wt.%]	multiple of Al
Al	14.72	1.00
Zn	60.95	4.14
Mg	23.26	1.58
Cu	0.65	0.04
V	0.33	0.02

of the observed minor defects on the Zn+Mg+Cu content evident.

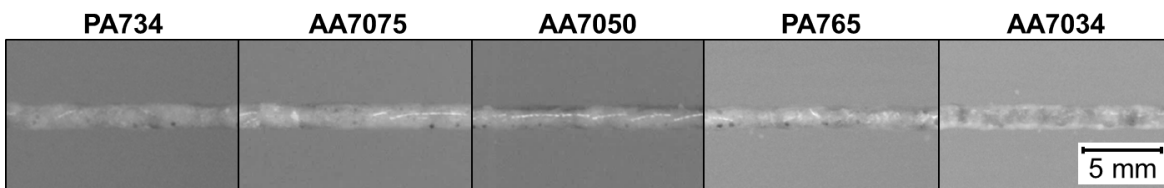


Figure 7.29.: Radiographs of the 'enhanced' 1 welds.

Due to the small size of the observed pores it could be assumed that they were most likely caused by hydrogen, as explained in Section 4.9. The origin of the hydrogen will be described in the following subsection. The presence of residual vanadium foil in the weld seams indicated the difficulties of accurate alignment of the laser and the vanadium foil.

### Hydrogen content

The measured hydrogen content of the 'enhanced' fusion zone of AA7075 lay at  $6.97 \pm 1.85$  ppm. This was still a low hydrogen content. However, in comparison to the base material, this meant an increase of more than +200%, as depicted in Fig. 7.30. This increased hydrogen content could lead to the small-scaled residual porosity observed in the weld seam.

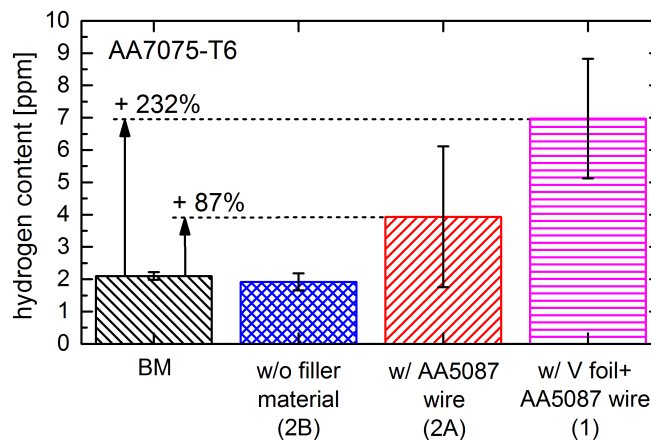


Figure 7.30.: Average hydrogen content of the 'enhanced' 1 weld of AA7075 in comparison to the base material and influence of the filler material used for laser beam welding with constant welding parameters.

Most of the hydrogen appeared to originate from the vanadium foil, since the addition of solely AA5087 filler wire resulted in a lower hydrogen content. The measurement of the as received vanadium foil disclosed a value of approximately 54 ppm, which was very high in comparison to the hydrogen content of the base materials and the filler wire (more than the 12.7-fold).

The reason for this was again the high surface-to-volume ratio of a foil in comparison to a common sheet material. In this regard, one origin for this hydrogen could be the oxide layer on the vanadium foil. Another reason for the increased hydrogen content could be the high solubility of hydrogen in V-rich aluminium alloys, as described by Kumar et al. [119]. The appearance of the as received vanadium foil is shown in Fig. 7.31. The observed yellow to blue temper colour represented different oxidation states originating from the oxidation during the manufacturing process of the foil. The removal of this oxide layer is rather extensive due to the low foil thickness. In addition, a new oxide layer would be formed during the welding process in the vicinity of the welding area with elevated temperatures. For this reason, it will be hard to completely avoid the unfavourable influence of vanadium on the resulting hydrogen content and thus on the formation of residual porosity. In spite of this high hydrogen content the influence on the resulting weld porosity was relatively low, because of its low volume in comparison to the volume of the melt pool.

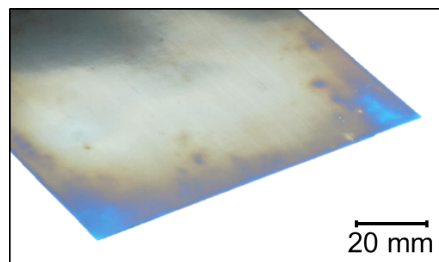


Figure 7.31.: Temper colours (oxide layer) of the as received vanadium foil.

### Microstructure

In the macrographs of the 'enhanced' welds of the first approach in Fig. 7.32 the already determined weld seam characteristics are reflected. The amount of porosity in the fusion zone was significantly reduced in comparison to the 'worst-case' welds. The large dark areas within the fusion zone were not any pores but V-rich inclusions, which exhibited an increased etching behaviour.

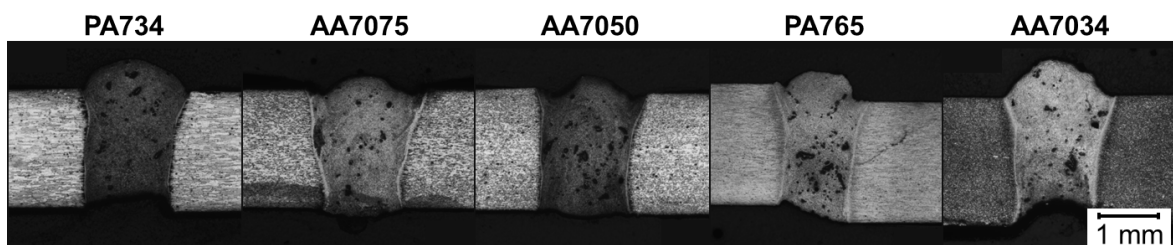


Figure 7.32.: Macrographs of the 'enhanced' 1 welds.

In the SEM micrographs in Fig. 7.33a these inclusions appeared as bright areas due to the higher density of vanadium, whereas the small-scaled residual porosity appeared as black

areas. Besides that, three different kinds of grains were identified: the V-rich grains (1) and the V-containing grains (2) and the V-free grain (3), as illustrated in Fig. 7.33b.

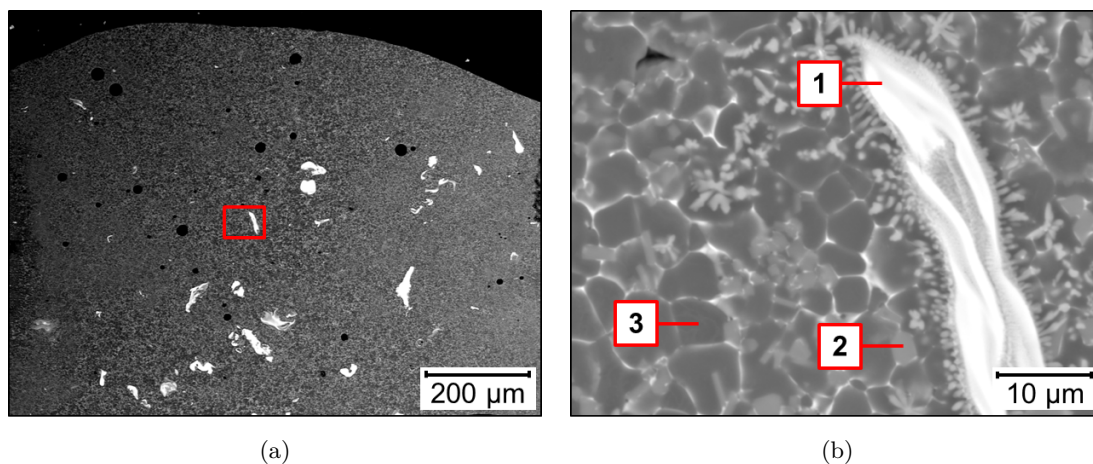


Figure 7.33.: SEM micrograph of an 'enhanced' 1 weld of alloy AA7075 (a) with the typical appearance of a V-rich inclusion (b).

The chemical compositions of the main phases observed in the fusion zone of the 'enhanced' welds are summarized in Table 7.5.

Table 7.5.: Chemical composition of the different phases in the 'enhanced' 1 weld according to Fig. 7.33b.

phase (position in Fig. 7.33)	Al [wt.%]	Zn [wt.%]	Mg [wt.%]	V [wt.%]
V-rich (1)	30	< 1	< 1	67
V-containing (2)	77	4	6	12
V-free (3)	95	3	2	< 1

The V-rich inclusions were completely melted during the welding and were not any foil residuals. They represented a mixture of vanadium and aluminium. However, their vanadium content was with 67 wt.% very high in comparison to the V-containing grains with only 12 wt.% vanadium. The V-rich inclusions were randomly distributed in the fusion zone, whereas the V-containing grains were very homogeneously distributed. The reason for this lay in the fact that vanadium and thus, also V-rich inclusions exhibit a higher density in comparison to aluminium, which might influence the melt pool dynamics.

A more detailed investigation of the microstructure along the fusion line revealed (Fig. 7.34) that at the transition of the fusion zone to the heat affected zone two distinct zones were present. Adjacent of the the fusion line a partially melted zone (PMZ) was observed. This zone exhibited a considerable melting of the grain boundaries, whereas the grains were unaffected by melting. In the direct vicinity of the PMZ the so-called over-aged zone (OAZ) was found. In this zone a coarsening of the precipitates within the grains was observed, caused by an unique heat treatment during the welding process. This locally changed microstructure might influence the resulting mechanical and corrosion properties, as assumed earlier for the 'worst-case' welds.

In Fig. 7.35 the diffractograms for an 'enhanced' weld of AA7075-T6 in the as welded condition as well as in the post weld heat treated to T6 condition are depicted. The dominant phase observed in the fusion zone - besides the aluminium peaks - was the  $Al_{10}V$  phase with a

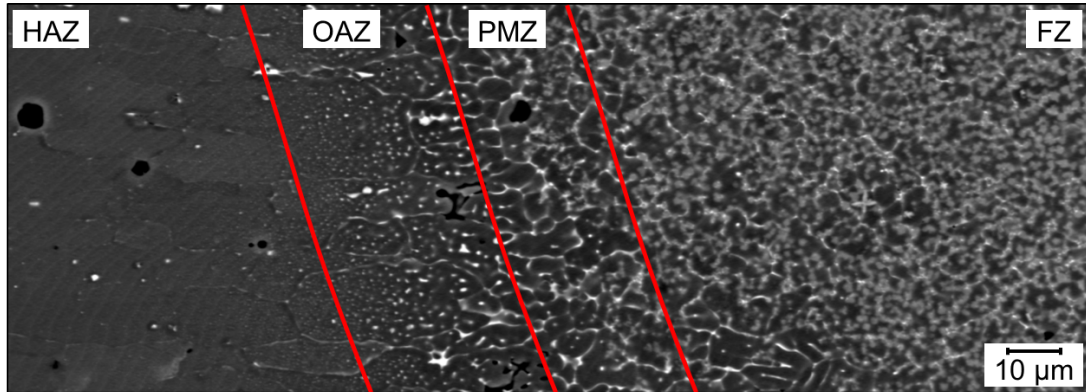


Figure 7.34.: Weld zones observed at the transition of the fusion zone to the heat affected zone of an 'enhanced' 1 weld of AA7075.

typical comb formation at  $2\Theta \approx 40-41^\circ$  and other distinct peaks. A post weld heat treatment caused - as already observed for the base material - an increase of the peak height.

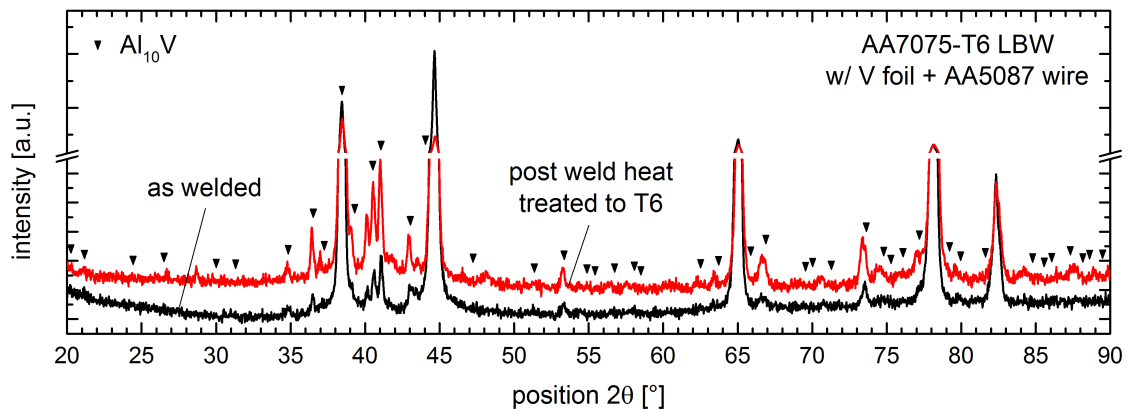


Figure 7.35.: Influence of the post-weld heat treatment on the phases in the fusion zone of an 'enhanced' 1 weld (XRD patterns).

Fig. 7.36 shows the effect of the filler material on the formation of phases in the fusion zone. The results for the fusion zones of the joints welded without any filler material ('worst-case') and welded with AA5087 ('variation') were resembling each other in the appearance. The dominant peaks - besides the aluminium peaks - were the two peaks at  $2\Theta \approx 40^\circ$ . These peaks were not observed for the base material and could not be identified with the help of known reference diffractograms. But according to Zhao et al. [111] these peaks were assigned to the presence of the Guinier-Preston zones. They were assumed to be Zn-rich (Mg,Zn) zones [120]. By appropriate annealing these zones would transform into the strengthening phase  $MgZn_2$ , as described in Section 2.2. In the fusion zones of the joints welded with vanadium these peaks disappeared. This could be explained by the fact that other V-induced phases became predominant - such as  $Al_{10}V$  - due to the changed chemical composition of the melt. No peaks for pure vanadium - for example caused by unmelted vanadium foil - could be identified.

The phase diagram of the Al-V system is shown in Fig. 7.37. The maximum equilibrium solubility of vanadium in aluminium lay at about 0.5 wt.%. The nearest phase in equilibrium

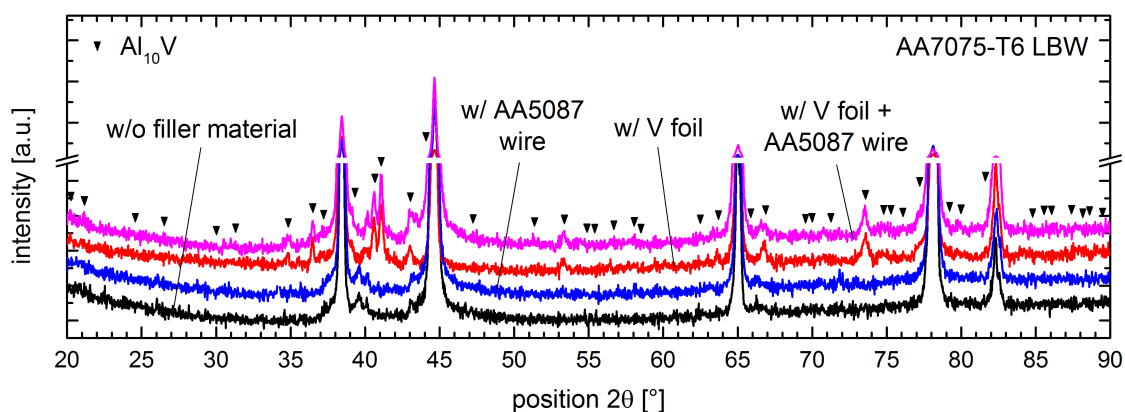


Figure 7.36.: Influence of the filler material on the phases formed in the fusion zone (XRD patterns).

with the solid solution (Al) is the  $\text{Al}_{10}\text{V}$  phase, which is sometimes also designated as  $\text{Al}_{21}\text{V}_2$  [121]. And this was the predominant intermetallic phase at the Al-rich side identified in the fusion zone of the 'enhanced' welds of the first approach. Furthermore, it can be seen that the melting temperature was considerably increased by the addition of vanadium - even for small quantities.

### Mechanical properties

The comparison of the average microhardness of the 'enhanced' 1 welds in Fig. 7.38 demonstrates that the use of vanadium foil was able to shift the hardness in the fusion zone to considerable higher values. Remarkably, these values were sometimes even higher than for the heat affected zone (up to +5% for AA7075). However, the average fusion zone hardness possessed a very large scatter. The hardness values in the heat affected zones were slightly lower than for the 'worst-case' welds and range from -12% for AA7050 to -16% for PA734. Only in case of the heat affected zone of AA7034 a higher hardness with 207 HV0.2 (-7%) was observed due to the absence of cracks.

By comparing the microhardness of the 'enhanced' welds for the alloys with the lowest and the highest Zn+Mg+Cu content - namely PA734 and AA7034 - to their respective 'worst-case' welds in Fig. 7.39 it was possible to see the above described effects of vanadium. In case of PA734 the average hardness of the fusion zone was almost equal to that of its heat affected zone. And in case of the AA7034 alloy no local hardness drops due to the presence of cracks in the heat affected zone were observed. The local hardness peaks observed in all fusion zones exhibited hardness values of up to 375 HV0.2.

The increase of the average hardness in the fusion zone - even above the average hardness of the heat affected zone - could be explained by the presence of the V-containing phase, whereas the hardness peaks were caused by the presence of V-rich inclusions. Pure vanadium can exhibit a hardness of up to 630 HV0.2. This was also the reason for the large scatter observed for the average hardness in the fusion zone, where these hard inclusions were inhomogeneously distributed.

In the preliminary study of Iwan [105] the influence of the vanadium foil thickness on the tensile properties was investigated. It was shown that the ultimate tensile strength was significantly reduced with increasing vanadium foil thickness (Fig. 7.40a). For the thickest foil with  $250\mu\text{m}$  the ultimate tensile strength was reduced by -50% in comparison to base

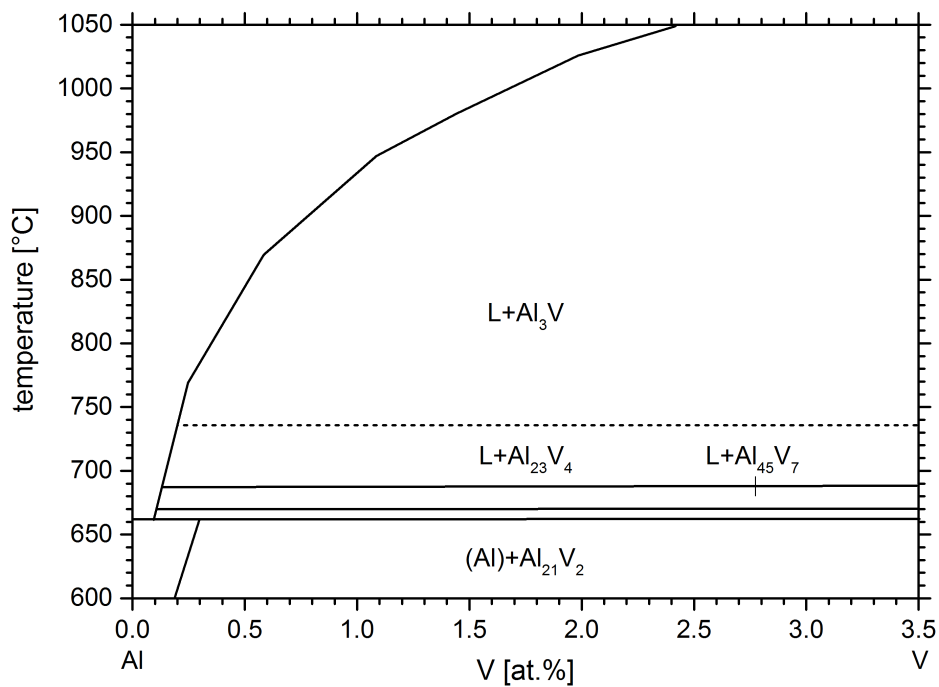
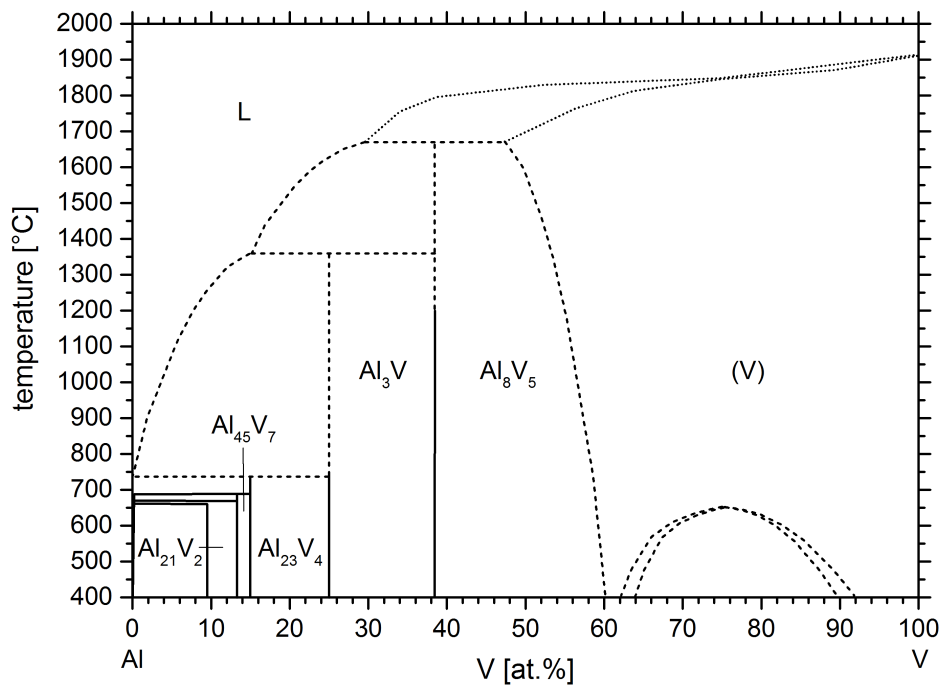


Figure 7.37.: Complete binary phase diagram of the Al-V system (a) and its Al-rich side (b) (according to Murray [121]).

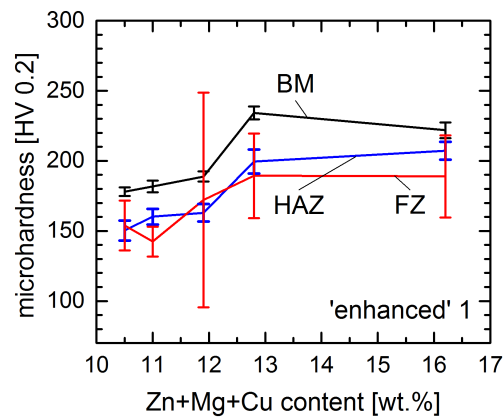


Figure 7.38.: Influence of the Zn+Mg+Cu content on the average microhardness of the 'enhanced' 1 welds in different weld zones.

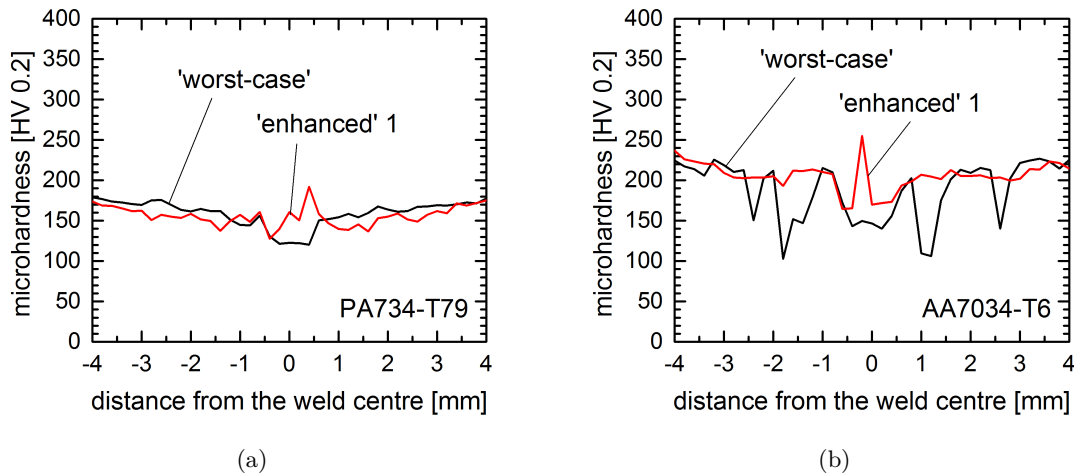


Figure 7.39.: Microhardness of the 'enhanced' 1 welds in comparison to the respective 'worst-case' welds.

material, whereas in case of  $40\mu\text{m}$  thickness this reduction was only -30%. It was mentioned earlier that an accurate positioning of the foil was essential. In case of an incomplete melted foil the ultimate tensile strength was even further reduced to a level far below the ultimate tensile strength of the 'variation' welds - containing severe porosity, as depicted in Fig. 7.40b.

According to Iwan [105], the fracture surface of the tensile specimens changed with increasing foil thickness, as it can be seen in Fig. 7.41a. For larger foil thicknesses the crack was deflected more often as for the  $40\mu\text{m}$  foil, which resulted in a more uneven fracture surface. In case of an incomplete melted vanadium foil the fracture surface was very even (Fig. 7.41b). This was indicating that the crack was running along the unmelted foil.

The failure predominantly initiated in all cases at the fusion line caused by the brittle nature of the partially melted zone. In case of the low foil thickness the crack ran into the fusion zone, whereas for larger foil thicknesses the crack was staying close to the fusion line.

In Fig. 7.42 the forming behaviour of the 'enhanced' welds is presented. It can be seen in Fig. 7.42a that the welded joints exhibited an inferior formability. At room temperature

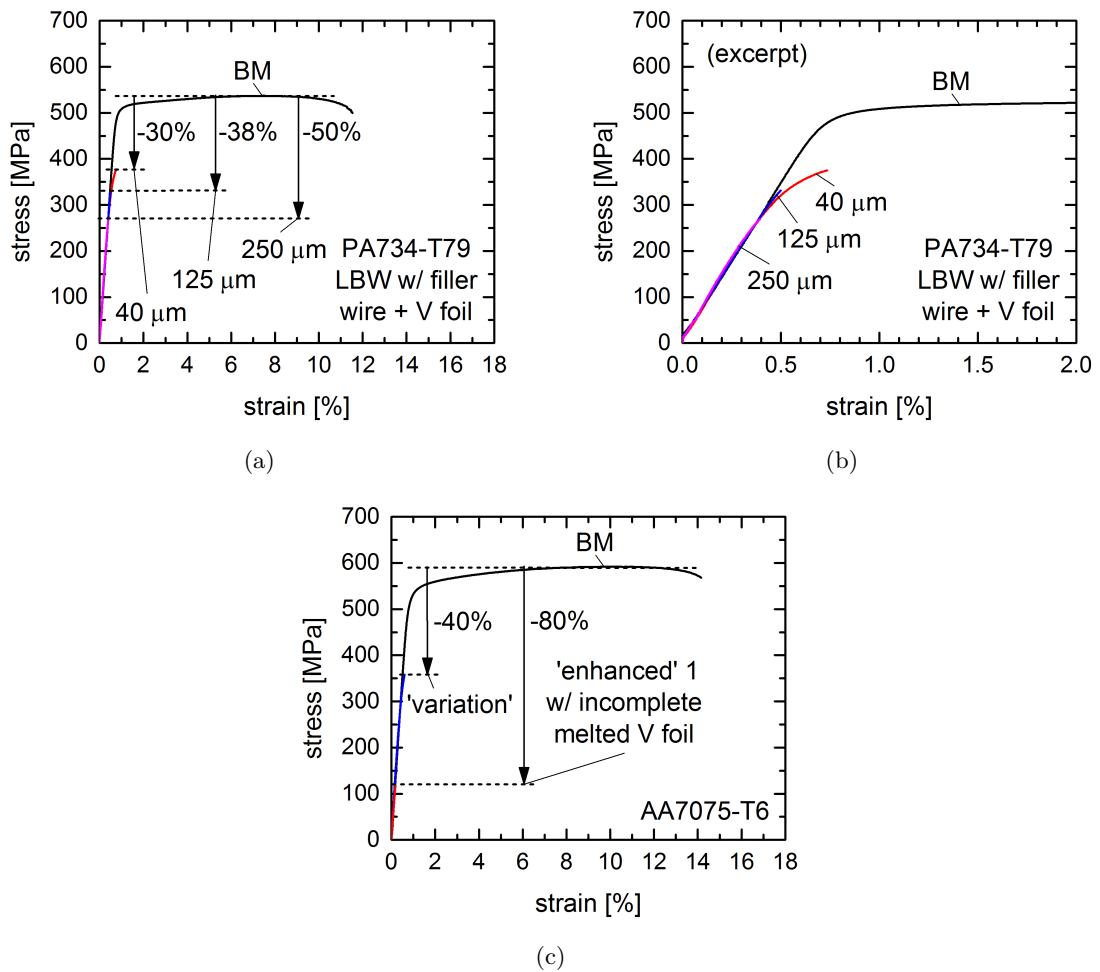


Figure 7.40.: Tensile properties in dependence to the used vanadium foil thickness (a) and (b) (according to Iwan [105]) and influence of an incomplete melted foil (c) in comparison to the base material.

the joints failed at a punch displacement of only 2.5 mm. This corresponds to a reduction of 89% in comparison to the base material. Even for the warm forming process no improvement could be achieved. From the strain distribution in Fig. 7.42b a strain localisation especially in the fusion zone could be deduced, which was generally not observed for base material. This indicated that the failure initiated first in the fusion zone. This can be also seen in Fig. 7.43.

A reason for the early failure of the 'enhanced' welded joints could be explained on the one hand by strain localisation due to softening of fusion zone and heat affected zone and on the other hand by the presence of hard V-rich inclusions. These inclusions acted as metallurgical notches, which resulted in an inhomogeneous forming behaviour. At elevated temperature these formability differences of the weld metal and the V-rich inclusions even increased due to the higher softening temperature of vanadium. The influence of the microstructural change - from rolling structure to cast-like structure - due to the welding process itself was expected to be small in comparison.

The fatigue behaviour of the 'enhanced' welds of PA734 in comparison to the base material is depicted in Fig. 7.44. The base material exhibited an approximate endurance limit - where no fatigue failure occurred - at about 55% of the ultimate tensile strength. In contrast, no

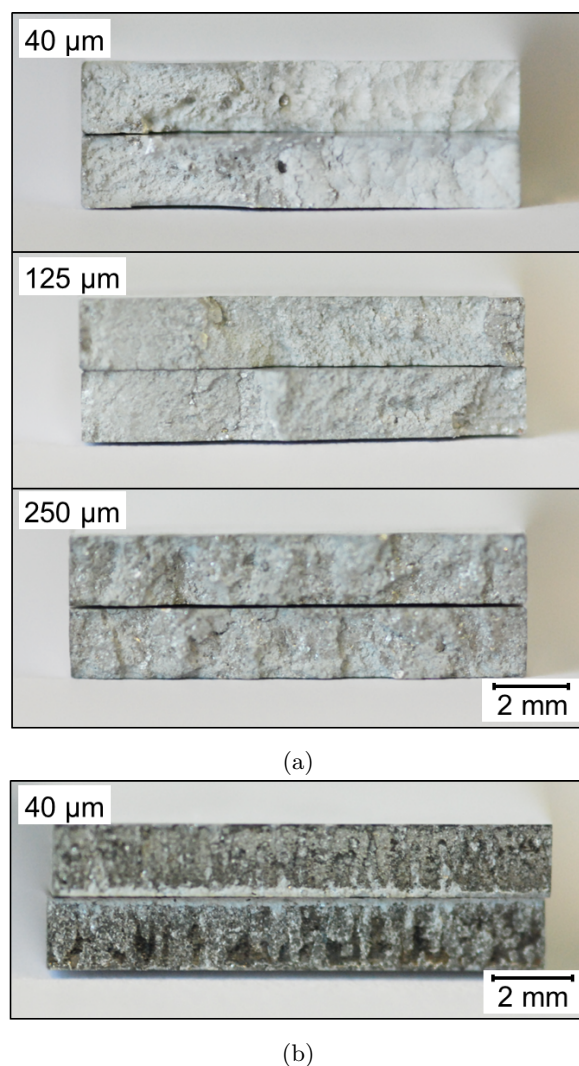


Figure 7.41.: Fracture surfaces of the 'enhanced' 1 weld tensile specimens in dependence to the vanadium foil thickness (a) and in case of an incomplete melting of the vanadium foil (b).

distinct endurance limit was observed for the 'enhanced' weld. However, at a fatigue stress of 15% of the ultimate tensile strength a life time of 10 million cycles was reached. Above 50% of the ultimate tensile strength no valid data was obtained for the 'enhanced' weld. By comparing both curves, it can be seen that the base material possessed with -0.04 a considerable lower Basquin slope as the 'enhanced' weld with -0.21. The fracture predominantly occurred along the fusion line.

The lower Basquin slope of base material implied that a small reduction of the load led to higher life times as for the 'enhanced' welds. The fracture along the fusion line arose from the metallographic misorientation between the fusion zone and heat affected zone as well as from the high notch sensitivity of Al-Zn alloys, as described by Kaufman [122].

The fatigue crack propagation (FCP) behaviour of the 'enhanced' welds of PA734 and the base material is shown in Fig. 7.45a. The linear regime in Fig. 7.45a could be described by the Paris law ( $da/dN = C(\Delta K)^m$ ). The respective parameters are summarized in Table 7.6. In this regard, the slope of base material was slightly lower than for the 'enhanced' weld. A shift to lower propagation rates as well as a local drop-off was observed for the 'enhanced' welds.

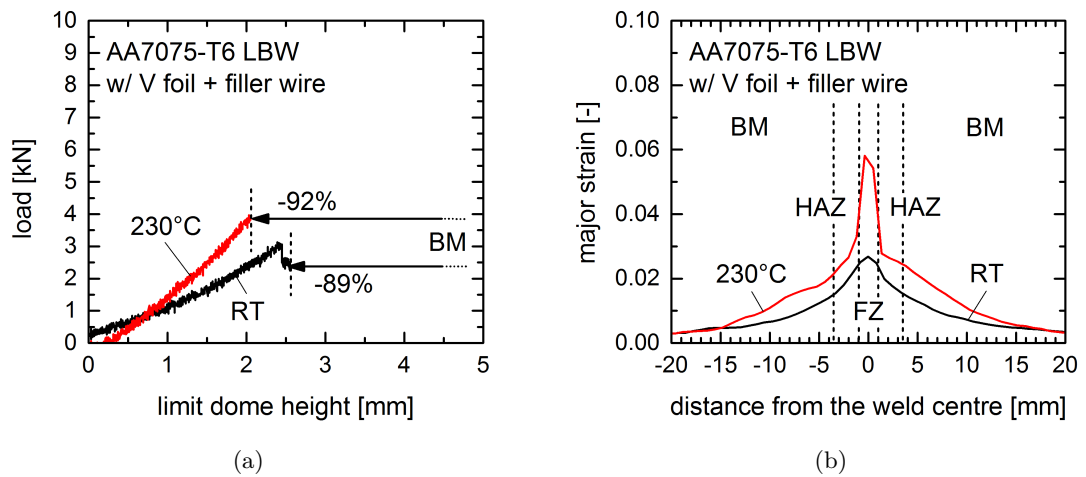


Figure 7.42.: Load-displacement curves (a) and major strain curves (b) during limit dome height testing of 'enhanced' 1 welds of AA7075-T6 at room temperature and 230°C.

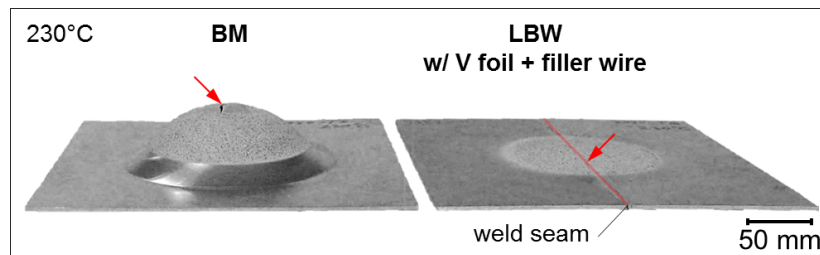


Figure 7.43.: Appearance of the dome formed at 230°C of AA7075 base material (left) and 'enhanced' weld (right). The red arrow indicates the site of fracture.

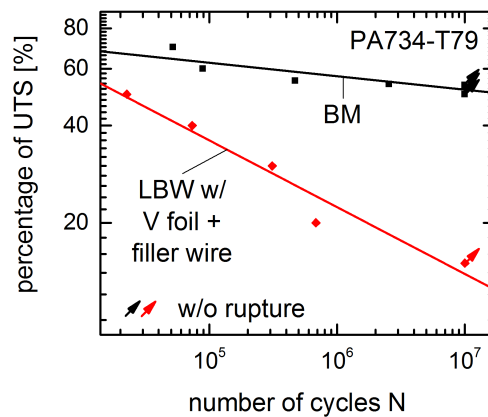


Figure 7.44.: Stress-life curves of the 'enhanced' 1 welds of PA734 and the base material (according to Iwan [105]).

The corresponding crack propagation life behaviour is depicted in Fig. 7.45b. Likewise, a shift to lower crack propagation rates was observed. During crack propagation the crack left the fusion zone - in which the pre-crack was inserted - and ran into the heat affected zone. The zone transition is marked in the diagrams. The resulting fracture surface is shown in

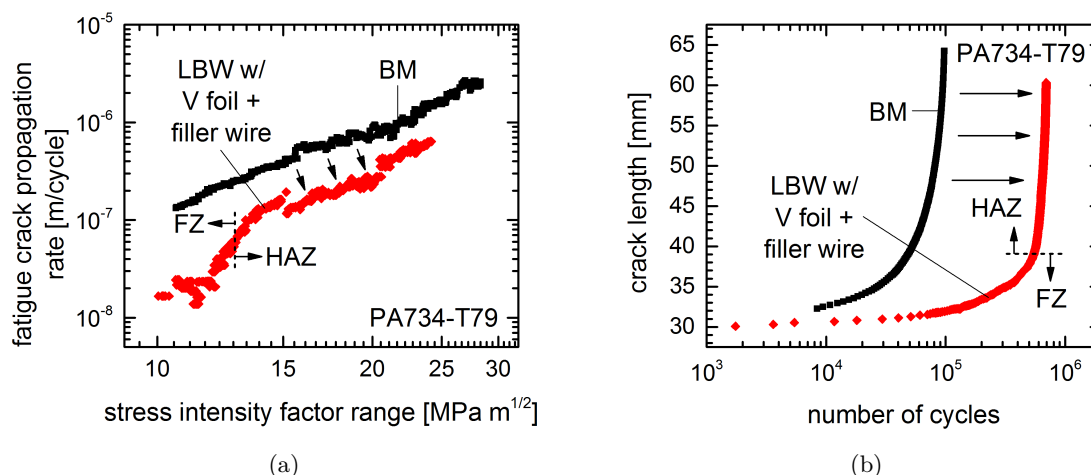


Figure 7.45.: Fatigue crack propagation rate (a) and crack propagation life (b) behaviour of the 'enhanced' 1 welds of PA734 and the base material (according to Iwan [105]).

Fig. 7.46a. A morphology change was observed for the transition from the fusion zone to the heat affected zone, as shown in Fig. 7.46b. The fusion zone possessed a fine-structured and brittle morphology - indicating a retarded crack propagation, whereas the heat affected zone possessed a more ductile morphology - indicating an enabled, fast and uniform crack propagation. The corresponding crack path through the specimen is illustrated in Fig. 7.46c.

Table 7.6.: Summarized parameters of the Paris law with corresponding coefficient of determination (according to Fig. 7.45a).

material	C	m	R <sup>2</sup>
BM	$1.60 \cdot 10^{-10}$	2.87	0.98
LBW w/ V foil + filler wire	$3.01 \cdot 10^{-11}$	3.09	0.91

The shift to lower crack propagation rates for the heat affected zone arose from the locally changed temper condition due to welding and the resulting lower tensile strength of the heat affected zone, as explained by Schwalbe [123].

The transition of the crack from the fusion zone to the heat affected zone arose from the local strength overmatching in the fusion zone due to the presence of hard V-rich inclusions - deflecting the crack - and the strength undermatching of the heat affected zone. In contrast, the strength undermatching of aluminium - welded without vanadium - was observed in the fusion zone, as described by dos Santos et al. [124].

## Corrosion behaviour

Although vanadium was added to the weld metal for the 'enhanced' welds the outer appearance of the corroded specimens - as welded and milled condition - was comparable to that of the 'worst-case' and 'variation' welds, as it can be seen in Fig. 7.47. The knife-line attack along the fusion line in the milled condition and its absence in the as welded condition as well as the attack in a certain region of the heat affected zone were resembling the corrosion behaviour of the 'worst-case' and 'variation' welds. The described differences between the as welded and the milled condition were clearly visible in the direct comparison in Fig. 7.47.

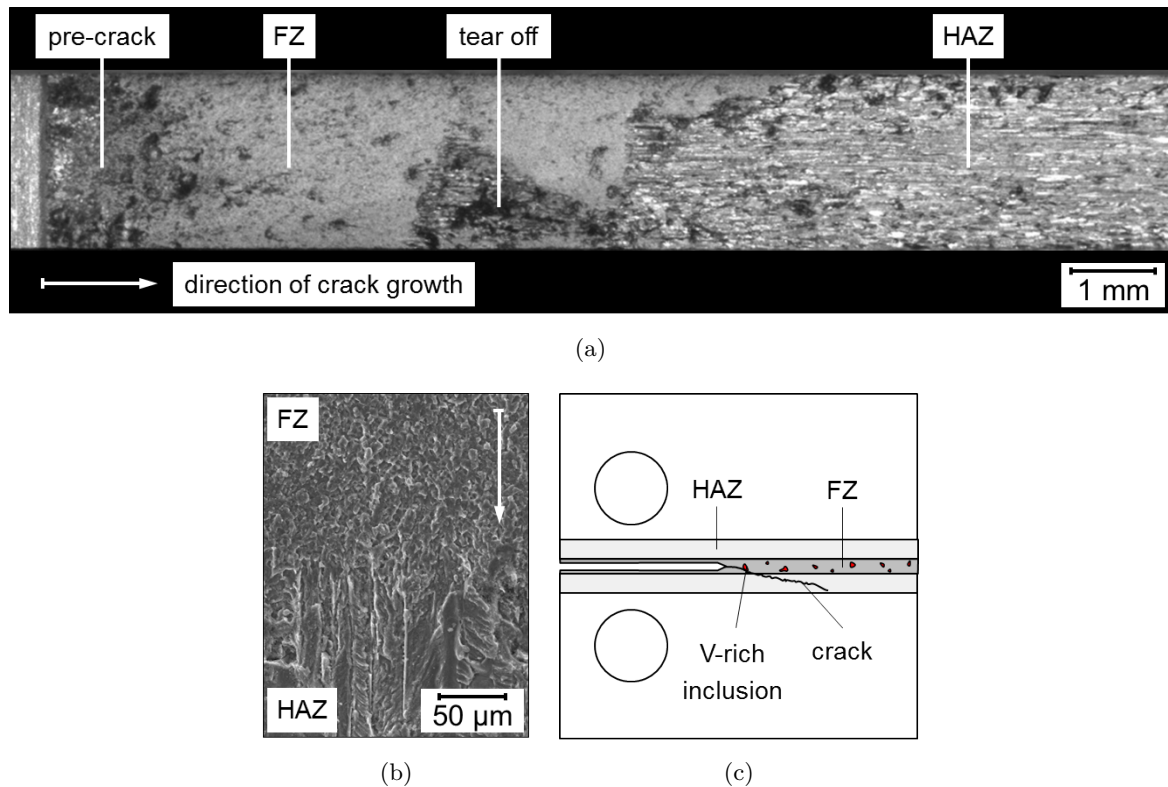
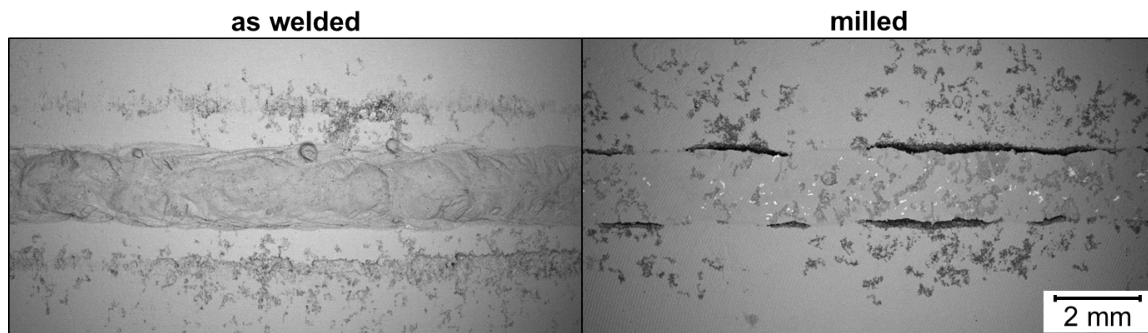


Figure 7.46.: Macrograph of the fracture surface (a), micrograph of the transition zone (b) of an 'enhanced' 1 weld of PA734 (according to Iwan [105]) and the corresponding crack path through the specimen (c) (according to dos Santos [124]).

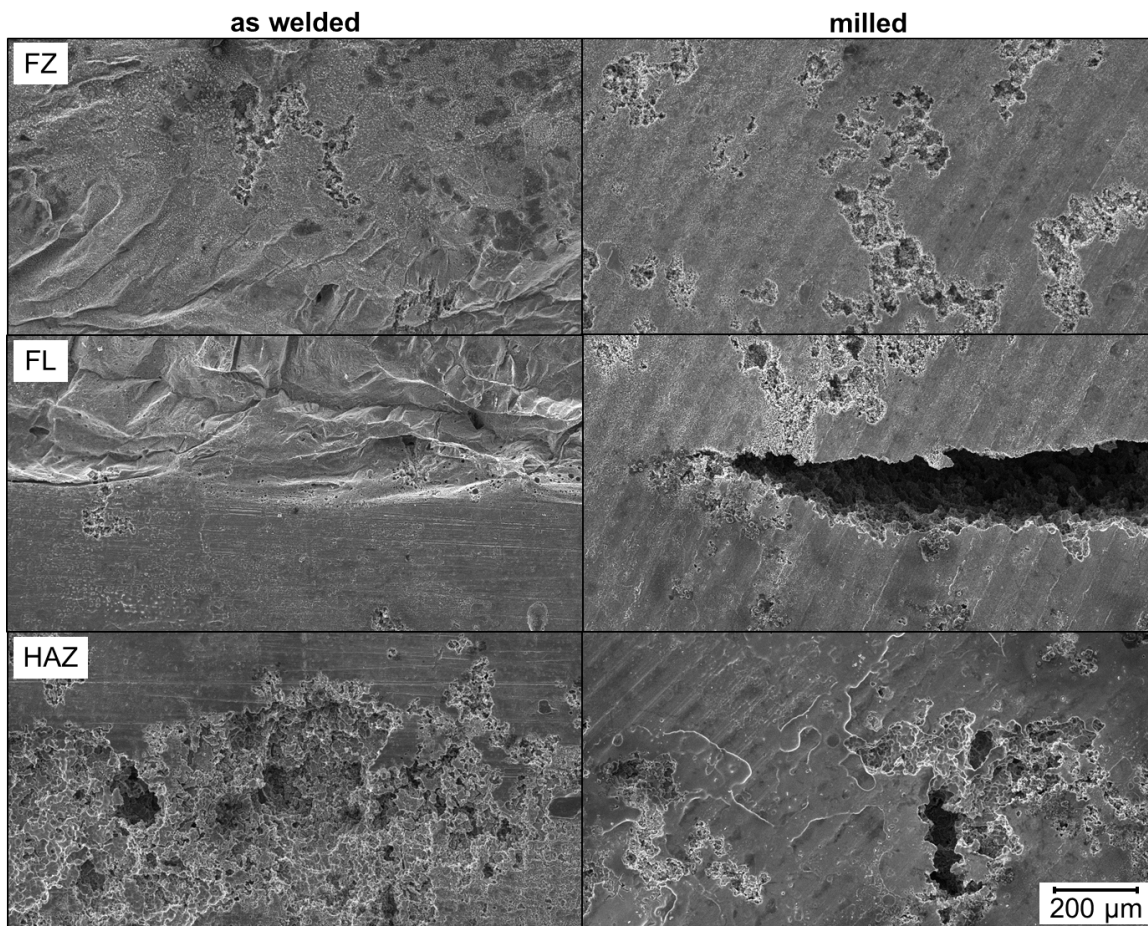
In the vicinity of the V-rich inclusions - of the milled specimens - no distinct corrosive attack was discovered. But in order to clarify the influence of vanadium in the weld metal on the corrosion behaviour an EDX mapping of the 'enhanced' welds - for both conditions - was conducted. In Fig. 7.48 it can be seen that there was no correlation between the local corrosive attack in the fusion zone and the presence of V-rich inclusions. Especially in case of the milled condition V-rich inclusions were present in the exposed weld seam surface. The putative correlation between the V-containing phase and the corrosive attack in the fusion zone was due to the fact that a shallow layer of the less noble Al-rich phase was removed during corrosion so that the V-containing material was laying bare.

By comparing the corrosion rate of 'enhanced' welds with 'worst-case' (without filler wire) and 'variation' (with filler wire) welds, it becomes obvious that welds containing vanadium had with 0.75% ( $\approx 0.02594$  g) considerable lower weight loss in the milled condition (Fig. 7.49). In case of the as welded condition the weight loss was with 0.57% ( $\approx 0.02845$  g) almost comparable to the welds welded without (0.54%) or solely with Al-Mg filler wire (0.56%).

The lower corrosion rate of the 'enhanced' welds was resulting from the more noble vanadium present in the weld metal. In the milled condition more V-rich inclusions and V-containing phases were bared so that less material was dissipated during corrosion. In the as welded condition, almost no V-rich inclusions were present at the weld seam surface. In addition, the concentration of the filler wire material was due to the way of feeding the wire higher in the upper region of the weld seam. Hence, the favourable protective effect of vanadium could not be leveraged.



(a)



(b)

Figure 7.47.: Corrosive attack of an 'enhanced' 1 weld of AA7075 in the as welded and milled condition: weld overview (BSE) (a) and weld details (SE) of the fusion zone, the fusion line and the heat affected zone (b).

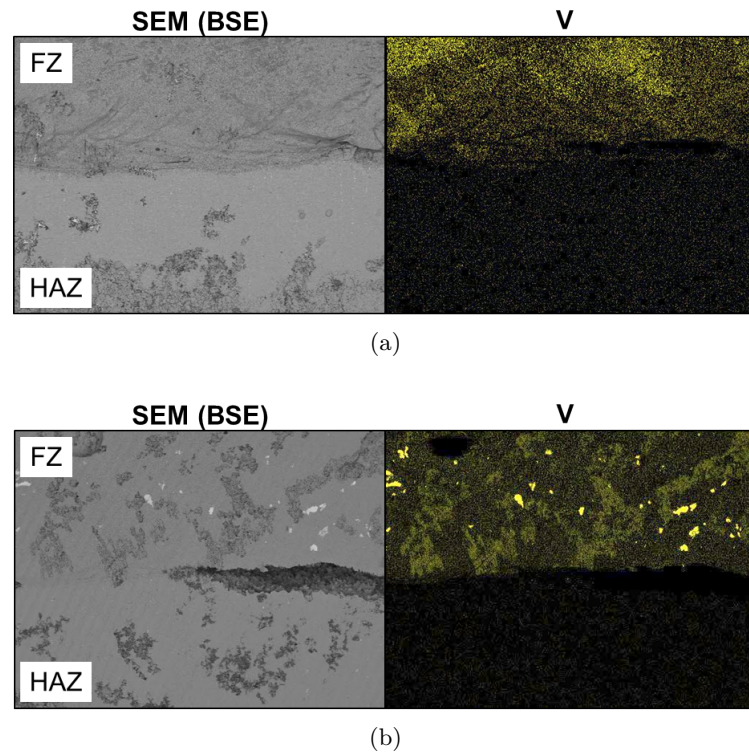


Figure 7.48.: EDX mapping for the 'enhanced' 1 welds in the as welded condition (a) and in the milled condition (b).

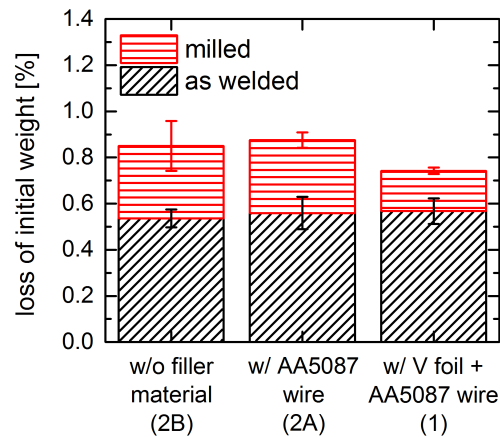


Figure 7.49.: Comparison of the weight loss of the different welding scenarios in the as welded and milled condition.

## 7.5. Enhanced welding: Second approach

The 'enhanced' welding scenario of the second approach allows a demonstration of the capability of using a high-power fibre laser with an enlarged laser beam for improving the weldability of different high-alloyed Al-Zn alloys. No special filler material was used besides a conventional Al-Mg filler wire.

## Optimization

**Variant A** The beam diameter of the fibre laser used for welding in this approach was with  $746\mu\text{m}$  (in focus) approximately twice as big as for the Nd:YAG laser with  $366\mu\text{m}$  (in focus), as illustrated in Fig. 6.2. Moreover, the keyhole dimensions could be further influenced by the parameters used for welding, as explained earlier in Section 4.3. Even in case of identical line energies the keyhole dimensions could differ. For comparison purposes the same line energy of  $34.29\text{ J/mm}$  as for the 'worst-case' welding was used. The defocussing of both beams was  $0\text{ mm}$ . However, a higher welding speed  $10500\text{ mm/min}$  and thus, also a higher laser power of  $6.0\text{ kW}$  was chosen so that larger keyhole dimensions resulted, as exemplarily depicted in Fig. 7.50. In this regard, the keyhole was predominantly elongated in welding direction (x). For achieving a beneficial effect, the initial beam diameter had to be large enough, otherwise the keyhole was still too narrow in y direction (perpendicular to the welding direction), as demonstrated for the 'variation' welding scenario. The increase of the laser beam diameter also led to a reduction of the beam irradiance to  $1.4\text{ MW/cm}^2$  in comparison to the 'worst-case' weld with a beam irradiance of  $1.9\text{ MW/cm}^2$  (referring to Eq. 4.15). The increase of the welding speed was limited, since high welding speeds were always accompanied by high cooling rates, which resulted in an entrapment of pores in the melt pool [12]. In addition, the increase of the laser power was limited, since the high resulting vaporisation rate was assumed to increase keyhole instabilities, as explained in Section 4.2 and 4.4.

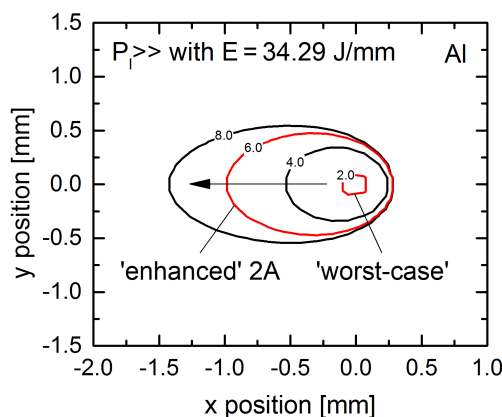


Figure 7.50.: Calculated keyhole dimensions for a constant line energy with increasing laser powers (in kW) (according to Section 4.3).

It turned out that the use of an enlarged laser beam diameter and the adjustment of the welding parameters resulted in an improvement of the laser weldability. In the following the welding parameters of this approach will be specified as the 'enhanced' 2A approach.

**Variant B** As mentioned earlier in Section 5.3, the dimensions of the laser beam - and thus of the keyhole - could also be further influenced by defocussing. For this reason, the influence of defocussing of the laser beam for a constant beam irradiance on the laser weldability was investigated. As starting point the same laser power ( $2.0\text{ kW}$ ), welding speed ( $3500\text{ mm/min}$ ) and defocussing ( $0\text{ mm}$ , on the surface) as for the 'worst-case' welding scenario was used, which resulted in full penetration and which corresponds to the welding parameters of the 'worst-case' welds. However, the laser beam diameter was bigger than the one used for the 'worst-case' welding. Thus, the beam irradiance for the 'worst-case' welds was with  $1.9\text{ MW/cm}^2$  considerable higher. As for the 'worst-case' welding, no filler wire but sufficient

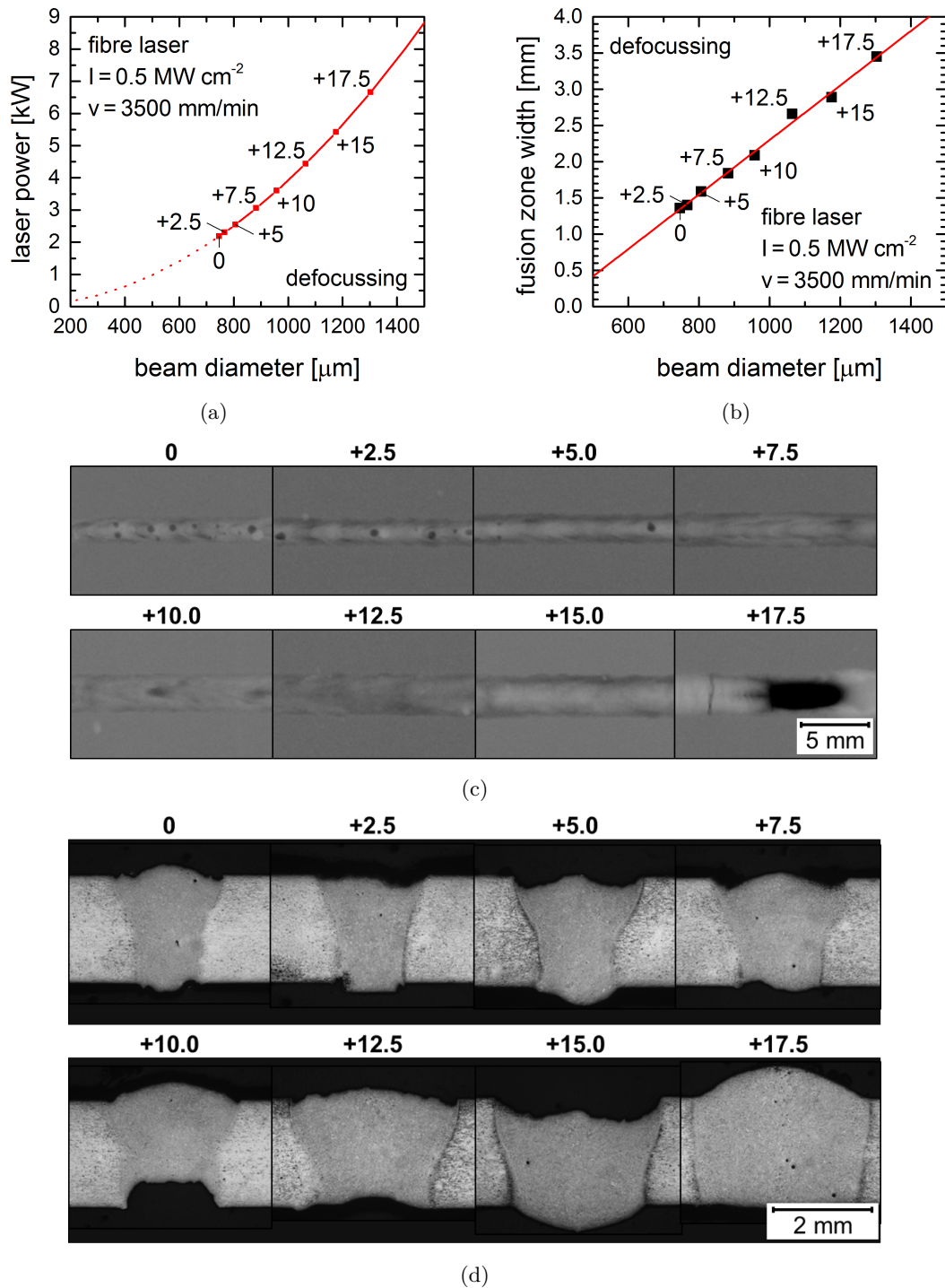


Figure 7.51.: Influence of the defocussing (in mm) on the required laser power (a), the fusion zone width (b), the inner discontinuities (c) and the weld seam shape (d) for a constant irradiance of  $0.5 \text{ MW cm}^{-2}$ .

shielding was used. The defocussing (above the material surface) was increased with a step size of +2.5 mm to values above the Rayleigh length, whereas the beam irradiance was kept constant at 0.5 MW/cm<sup>2</sup> by adjusting the laser power, as shown in Fig. 7.51a. This low beam irradiance had also a beneficial effect on the weldability, as mentioned earlier in Section 4.7. Negative defocussing (below the material surface) also led to an increase of the spot size. However, negative defocussing generally results in a higher vapour temperature and pressure and thus in an increased keyhole instability, as it was stated by Verhaeghe [12].

In Fig. 7.51c and d the radiographs and macrographs for each of the defocussing steps are depicted. It becomes obvious that the amount of porosity was decreasing for increasing defocussing until no porosity was observed for a defocussing of +7.5 mm - which corresponded to a beam diameter of 883  $\mu\text{m}$ . For a defocussing of  $\geq 17.5$  mm the keyhole became unstable and blow-holes were formed, mainly due to the high laser power. Furthermore, severe cracking was observed for this high line energy. With increasing laser beam diameter the size of the fusion zone increased almost linearly, as shown in Fig. 7.51b.

It turned out that a defocussing of +7.5 mm resulted in best weld seam with regard to discontinuities (pores, cracks and blow-holes), the fusion zone size and shape. In the following the welding parameters ( $P_l = 3.0$  kW and  $v = 3500$  mm/min) of this approach will be specified as the 'enhanced' 2B approach. The resulting line energy of this approach was with 51.43 J/mm considerably higher than for all other welding scenarios.

### Transient temperature distribution

In Fig. 7.52a the peak temperatures measured during the 'enhanced' welding of the second approach (2A and 2B) are depicted in relation to that of the 'variation' welding. The temperatures of the 2A weld were lower than measured for the 'variation' weld, although the same line energy and filler wire feed was used. However, the fusion zone of the 2A weld was larger than for the 'variation' weld, as it can be seen in Fig. 7.52b. In contrast, the 2B weld - welded without any filler material and with a higher line energy - exhibited higher temperatures, as expected from the consideration in Section 4.3. These higher temperatures resulted also in a larger fusion zone width as observed for the 'enhanced' 2A weld and the 'variation' weld. The observed temperature differences were expected to be even larger in vicinity of the fusion zone and in the fusion zone itself.

The temperature difference between the 'enhanced' 2A weld and the 'variation' mainly arose from the considerable larger laser beam used for welding. This resulted in a larger keyhole and fusion zone, which generated a changed temperature distribution. Other reasons were the differing laser power and welding speed, although the same line energy was used for welding. As depicted in Fig. 7.50, the dimensions of the keyhole and the melt pool strongly depended on these two parameters.

### Outer appearance

The favourable effect of using an enlarged beam diameter was reflected in the outer appearance of the welds. The 'enhanced' 2 weld seams of all Al-Zn alloys showed a very uniform appearance. But there were also differences between the 'enhanced' 2A welds welded with a low line energy and the 'enhanced' 2B welds welded with a higher line energy, as it can be seen in Fig. 7.53.

The 2A welds were narrower than the 2B welds, but they exhibited the same width as the 'enhanced' 1 welds. Due to the use of filler wire for 2A welds a slight excess of penetration was formed, whereas the omitting of any filler material, as for 2B welds, resulted in a slight undercut at the weld front. At the root side of all welds a brown to black deposit was

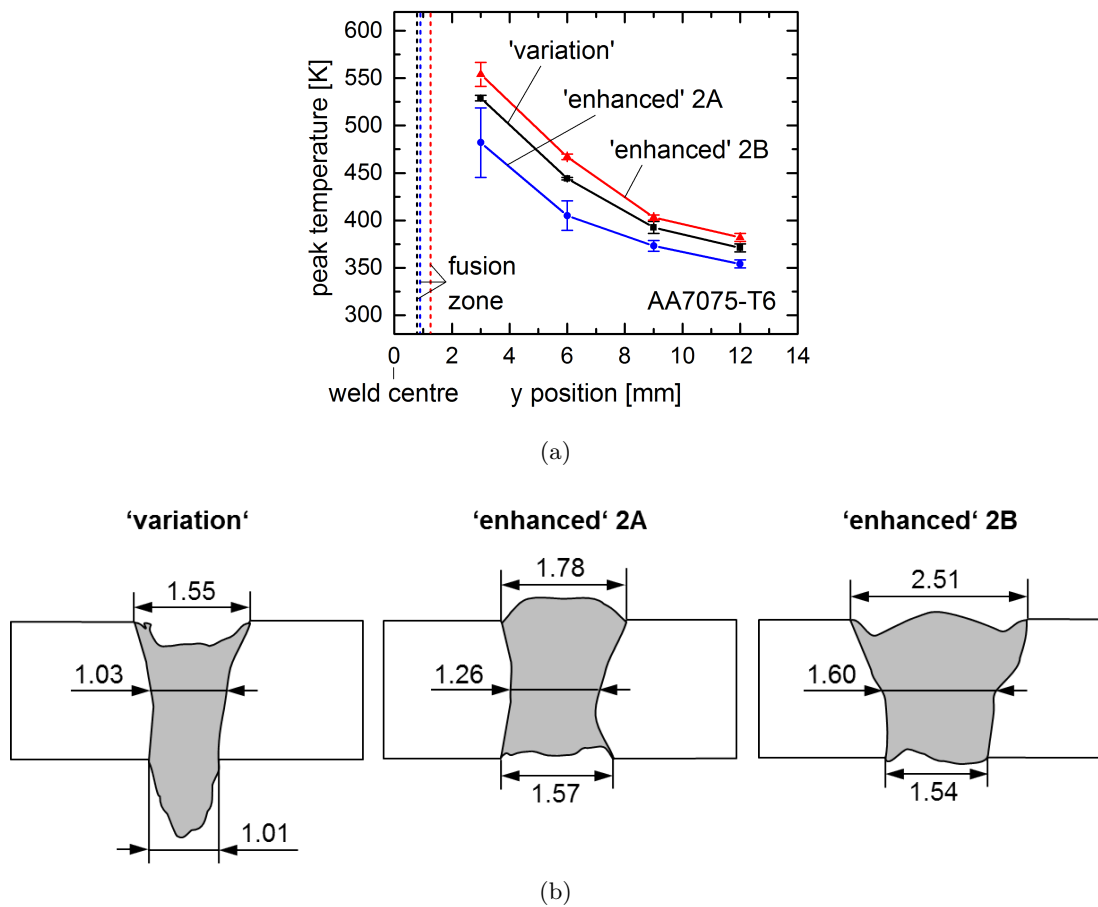


Figure 7.52.: Temperature profile (a) and resulting fusion zone dimensions (b) during the 'enhanced' 2A and 2B welding in comparison to the 'variation' welding of AA7075.

observed. In case of the 2B welds, welded with a higher line energy, the amount of deposit was considerably higher, although the same gas shielding set-up was used. The same was true for the amount of spatter, which was predominantly accumulated in the vicinity of the weld seam.

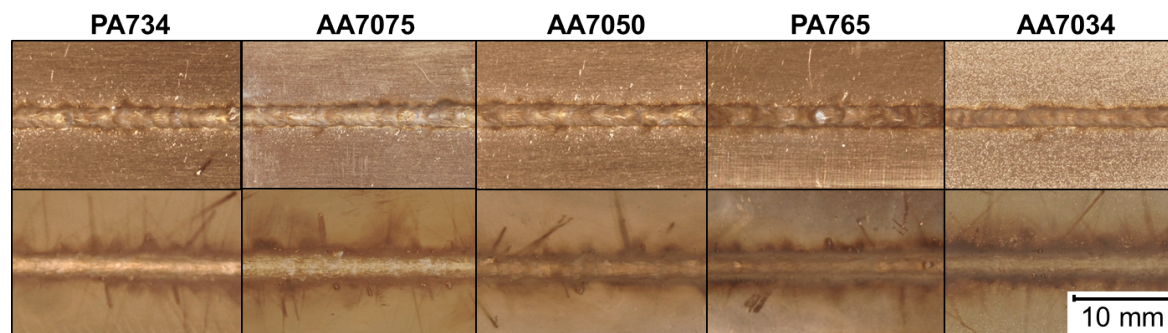
The weld seam dimensions were not only influenced by the line energy, laser power and welding speed, but also by the defocussing of the laser beam - which resulted in larger keyhole dimensions - and the use of a filler wire - which resulted in a higher energy requirement for melting the additional material.

Although, there were some similarities of the 'enhanced' 2A welds to the 'variation' welds - namely the line energy and the use of filler wire - the welds resulting were completely different. The reason for this lay in the fact that the larger beam diameter helped to stabilize the keyhole and to improve the degassing during welding.

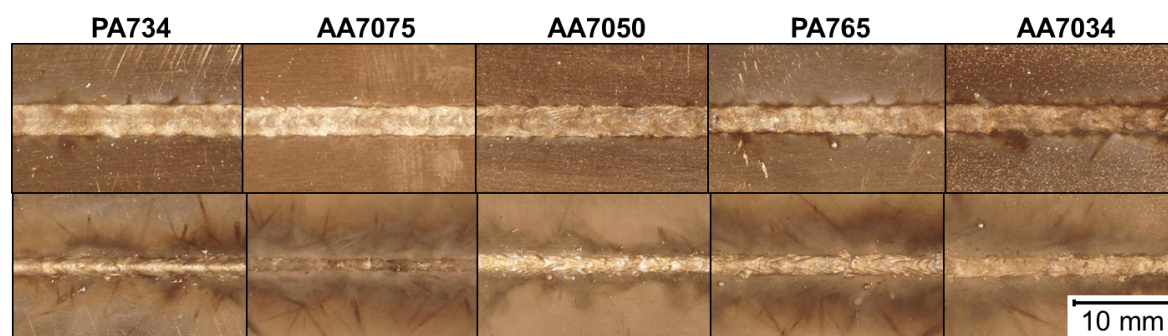
The increased amount of deposit and spatter for the 2B welds in comparison to the 2A welds could be explained by the higher line energy, which caused higher temperatures in the vicinity of the weld and thus also a higher vaporisation rate.

### Inner discontinuities

The radiographs in Fig. 7.54 demonstrate that by generating an enlarged keyhole the porosity in the weld seams was almost eliminated. Even for the 'enhanced' welds (2A) welded with the



(a)



(b)

Figure 7.53.: Weld appearance of the 'enhanced' welds welded with a lower line energy (2A) (a) and welded with a higher line energy (2B) (b).

Al-Mg filler wire almost very few residual porosity was visible, in contrast to the 'variation' welds. Only the welds of AA7034 exhibited some residual porosity. Although, the 'enhanced' welds (2B) possessed indicators for keyhole instabilities - such as the increased amount of deposit and spatter - no evidence for that was found in the radiographs. Surprisingly, transverse cracks in the fusion zone were observed for the 'enhanced' welds (2A) welded with filler wire, although an Al-Mg filler wire is strongly recommended in order to avoid hot cracking in the fusion zone. But this kind of crack only occurred in the rolled alloys PA734, AA7050 and AA7075 and not in the extruded and very high-alloyed alloys PA765 and AA7034. In contrast, all 'enhanced' welds (2B) welded without filler did not exhibit any cracks in the fusion zone.

Due to the absence of high-dense material or excess of penetration no obliteration of putative porosity on the radiographs was expected.

The occurrence of transversal cracks only for PA734, AA7050 and AA7075 welded with filler wire could be explained by the changed chemical composition. In this regard, the Cu and Mg content were of particular importance, as explained in Section 4.8. By the addition of the Al-Mg filler wire AA5087 the Mg content of the weld metal was slightly increased, whereas the Cu content was slightly decreased. Referring to Fig. 4.23b the highest cracking sensitivity was expected for a Cu content of approximately 3.0 wt.% and a Mg content of 1.25 wt.%. Thus, the highest cracking sensitivity was expected for the base material PA734 due to the critically low Mg content in combination with a relatively high Cu content followed by AA7050 and AA7075. In contrast, the base materials PA765 and AA7034 had a favourable low Cu content, as it can be deduced from Table 6.1. The calculated chemical compositions of the 'enhanced' fusion zones of all alloys welded with (2A) and without (2B) filler wire are specified in Table

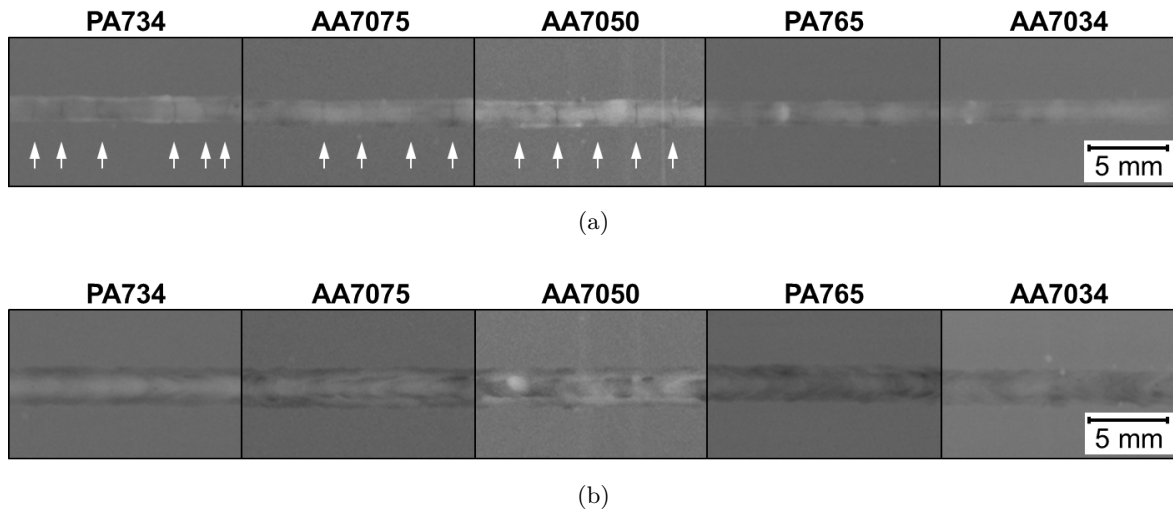


Figure 7.54.: Radiographs of the 'enhanced' welds welded with filler wire (2A) (a) and without filler wire (2B) (b). The white arrows indicate the site of cracks.

7.7 neglecting losses due to the vaporisation during welding. It became apparent that the addition of filler wire did not lead to a significant change of chemical composition. Because of the fact that PA734, AA7075 and AA7050 did not exhibit cracks in the 'enhanced' welds welded without filler, it was assumed that further aspects had an influence on the cracking behaviour.

Table 7.7.: Calculated chemical composition of the 'enhanced' fusion zones welded with filler wire (2A) and without filler wire (2B).

alloy	scenario	Mg	Cu
		[wt.%]	[wt.%]
PA734	2A	1.96	1.9
	2B	1.64	2.13
AA7075	2A	3.03	1.79
	2B	2.9	2.0
AA7050	2A	2.87	2.4
	2B	2.6	2.6
PA765	2A	2.75	0.51
	2B	2.72	0.61
AA7034	2A	2.22	0.76
	2B	2.23	1.0

Another reason for cracking of only selected alloys could be the microstructure of these alloys, as described in Section 4.8. It was demonstrated by Coniglio et al. [78] and Coniglio [77] that a small grain size has a beneficial effect on the cracking sensitivity. The microstructure is not only influenced by the general chemical composition and the processing of the alloys but also by the addition of minor alloying elements acting as grain refiners. In the description of the base material it was already noted that PA765 and AA7034 exhibited an extraordinary fine microstructure in comparison to the other alloys (Fig. 7.2). The grain refiner could also decrease the average grain size in a weld seam. Microstructural differences of the weld seams of both alloys are shown in Fig. 7.56 and will be explained in the following.

It was also stated by Coniglio et al. [78] that stress and strain fields around the welding zone could influence the cracking behaviour of aluminium alloys. These fields predominantly depend on the parameter used for welding. Cicală et al. [125] explicated the unfavourable effect of high welding speeds on the crack susceptibility. Welding speeds  $>5000$  mm/min resulted in a significant increase of cracks in the fusion zone due the deformation of the melt pool during solidification.

From this it was concluded that cracking occurred for alloys PA734, AA7050 and AA7075 with an unfavourable chemical composition in combination with unfavourable welding parameters used for welding the 'enhanced' 2A welds.

### Hydrogen content

The hydrogen content of the 'enhanced' fusion zones of the second approach was not measured. Because of the similarities in matters of the chemical composition to the 'worst-case' welds - welded without filler material - and 'variation' welds - welded solely with AA5087 filler wire - the respective hydrogen content were expected to be comparable (Fig. 7.30). Due to the absence of any pores even lower hydrogen level could be possible.

### Microstructure

The macrographs of the 'enhanced' welds of the second approach in Fig. 7.55 reflect the favourable effect of an enlarged keyhole. The only discontinuities observed were the residual porosity in AA7034 and the really small undercut in case of the 2B welds. Both 'enhanced' welds 2A and 2B showed distinct differences in the fusion zone size and shape. The 2A welds possessed a narrow and rectangular weld seam - comparable to the 'enhanced' welds of the first approach, whereas the weld seams of the 2B welds were considerably larger and had a trapezoidal shape.

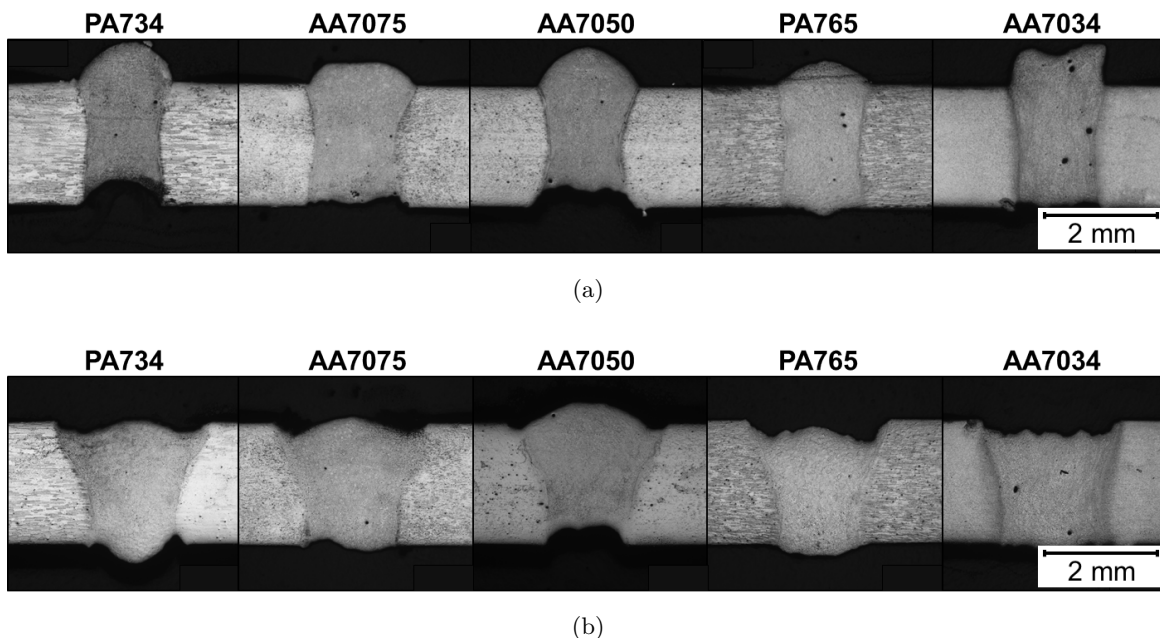


Figure 7.55.: Macrographs of the 'enhanced' welds welded with filler wire (2A) (a) and without filler wire (2B) (b).

The trapezoidal shape of the 2B welds could be explained by the large defocussing of  $+7.5$

mm of the laser beam, which yielded not only in an increase of the beam diameter but also in a change of the beam irradiance distribution - from the top-hat to a more Gaussian-like distribution, as explained earlier in Section 5.3. The larger fusion zone width was also caused by the high line energy used for welding.

Due to the presence of cracks in the fusion zone of only certain 2A welds, as observed on the radiographs, the microstructure of these welds was further investigated. For this purpose, the fusion zone of PA734 - which exhibited cracks - was compared to that of AA7034 - which was crack-free. As it can be seen in Fig. 7.56, the AA7034 fusion zone possess very small and equiaxed grains, whereas larger dendrites were formed in case of alloy PA734.

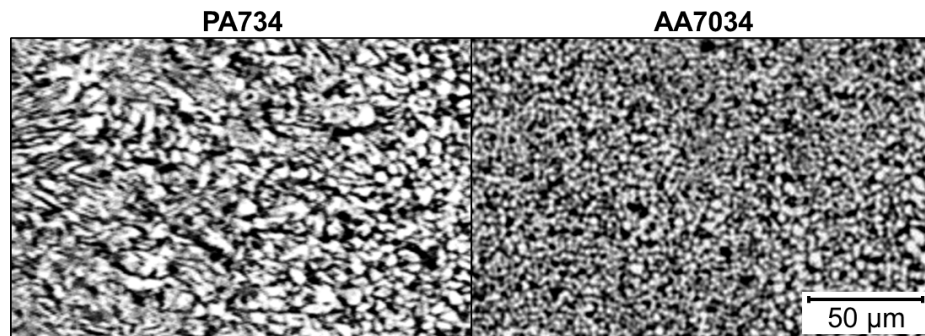


Figure 7.56.: Differences in microstructure in the 2A fusion zones of PA734 and AA7034.

These differences in the microstructure in the fusion zone of both alloys were caused by the different chemical composition and processing of the base materials, which might also have an influence on the cracking sensitivity.

No XRD measurement for the 'enhanced' welds were performed. But it was expected that the phases formed in AA7075 during 2A welding corresponds to that of the 'variation' weld, since the same base and filler materials were used. The slightly differing heat input due to the different welding parameters might only cause higher peak intensities due to the coarsening of precipitates, but it does not cause significantly different peak positions. This is the case only if different filler materials are used. The same was true for the 2B and 'worst-case' welds of AA7075. In both case no filler material was used. The presence of weld discontinuities - such as pores and cracks - do not have any effect on the phases formed in the fusion zone and heat affected zone.

### Mechanical properties

In Fig. 7.57 the average microhardness of the 'enhanced' welds (2A and 2B) - exhibiting certain differences in the HAZ and FZ - is shown. In contrast to the 'enhanced' welds of the first approach no considerable improvement of the fusion zone hardness was observed. Nevertheless, the hardness of the heat affected zone of the 2A welds exhibited the lowest degradation in comparison to the 'worst-case', 'enhanced' 1 and 2B welds, as for example in case of AA7034 with only -5%. The highest hardness in the fusion zone with 168 HV0.2 and heat affected zone with 210 HV0.2 was observed for the 2A weld of AA7034-T6, whereas PA765-T79 - with the highest initial hardness - exhibited the severest hardness reduction with up to 32% in heat affected zone of the 2B weld. In general it can be stated that the 2B welds possessed a severer degradation of the hardness.

The comparison of the 'enhanced' welds of the second approach of the alloys PA734 and AA7034 to their respective 'worst-case' welds in Fig. 7.58 reveals the negligible effect of using an enlarged laser beam on the microhardness.

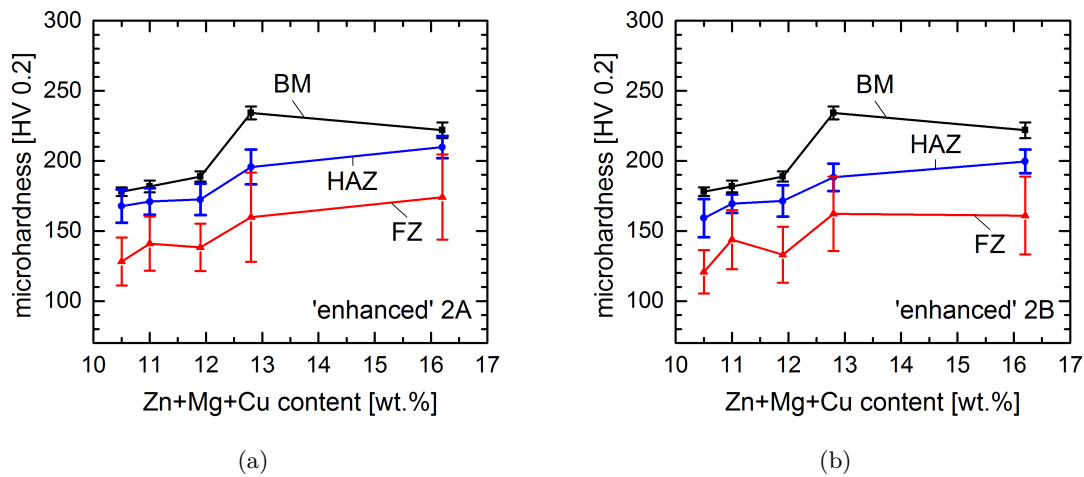


Figure 7.57.: Average microhardness of the 'enhanced' welds 2A (a) and 2B (b) in different weld zones.

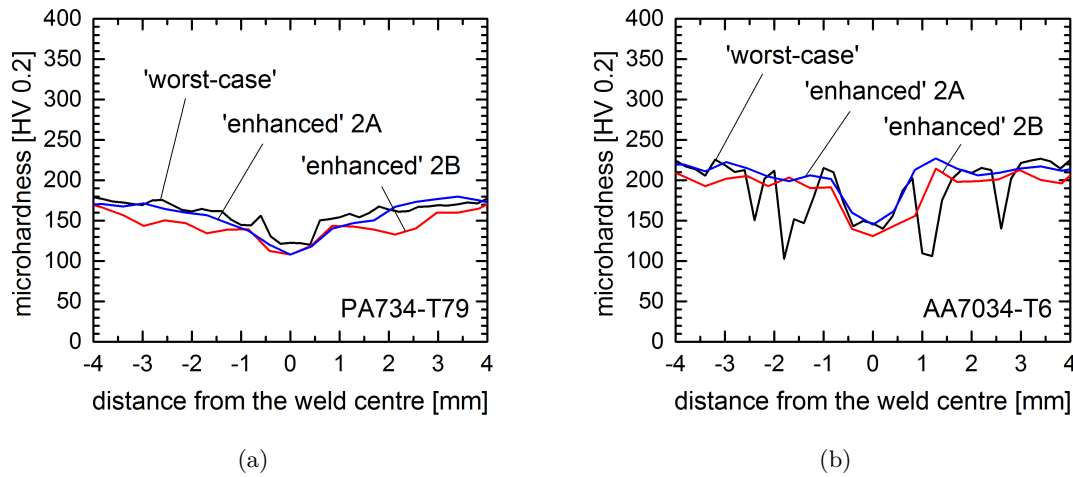


Figure 7.58.: Microhardness of 'enhanced' welds of the second approach in comparison to the respective 'worst-case' welds of PA734 (a) and AA7034 (b).

The greater degradation of the hardness in the heat affected zone in the 2B welds arose from the higher transient temperatures during welding with high line energy. The temperature fields measured during welding of the 'enhanced' welds of the second approach are described in the following.

Furthermore, differences in the tensile properties were observed for the 'enhanced' 2A and 2B welds, as it can be seen in Fig. 7.59. The 2A weld of AA7075 possessed a reduction of the ultimate tensile strength of -34% in comparison to the base material. In case of the 2B weld a slightly higher ultimate tensile strength (+3%) was observed. But in comparison to the 'variation' weld an improvement was clearly visible. Besides the reduction of the tensile strength, a considerable reduction of the ductility was determined. A slightly higher ductility was observed for the 2B weld. However, the strain at failure was still -95% in comparison to the base material AA7075-T6.

The fracture surfaces of the 'enhanced' welds 2A and 2B possessed a completely different appearance, as shown in Fig. 7.60. The 2A welds - welded with a filler wire - exhibited

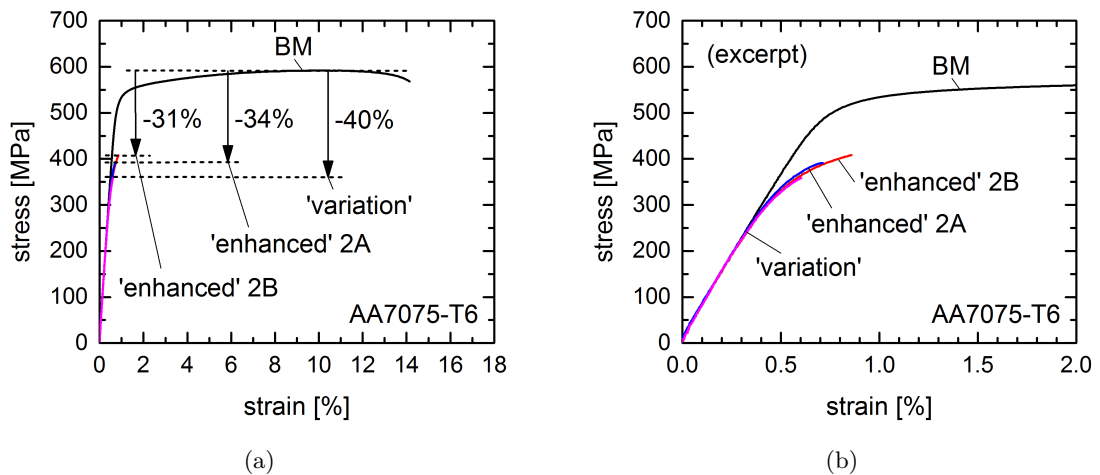


Figure 7.59.: Tensile properties of the 'enhanced' welds of the second approach in comparison to the base material and a 'variation' weld of AA7075.

crack-like flaws at the fracture surface and the crack was running almost in the middle of the fusion zone. In contrast to that, the 2B welds - welded autogenously - exhibited a very smooth fracture surface, whereas the crack was predominantly running along one of the fusion lines.

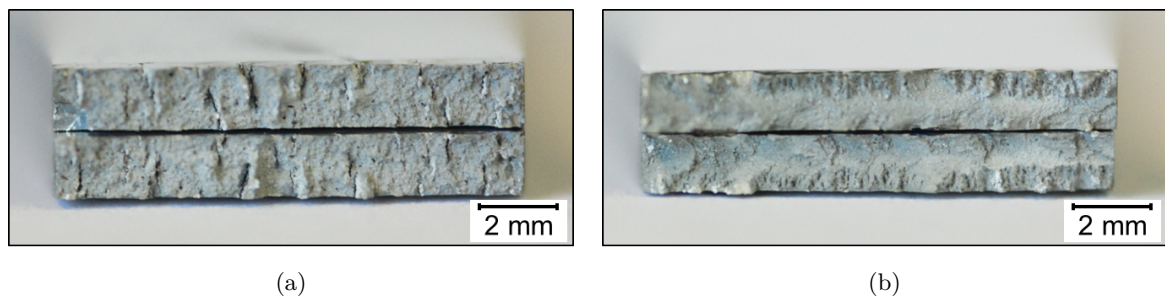


Figure 7.60.: Fracture surfaces of the 'enhanced' weld tensile specimens of 2A (a) and 2B (b) of AA7075.

The slightly lower ultimate tensile strength of the 2A welds arose from the presence of cracks in the fusion zone, as observed in the respective radiograph. This was also reflected in the appearance of the fracture surface and the crack path of the 2A weld. However, it turned out that the presence of porosity in the fusion zone, as in case of the 'variation' weld, had a greater influence on the resulting mechanical properties.

### Corrosion behaviour

The corrosion behaviour of the 'enhanced' welds of the second approach was not investigated. But due to the similarities in matters of the chemical composition to the 'worst-case' welds - welded without filler material - and 'variation' welds - welded solely with AA5087 filler wire - the corrosion behaviour can be expected to be comparable.

The larger dimensions of the fusion zones and the heat affected zones - especially in case of the 'enhanced' weld (2B) might result in a slightly higher weight loss due to corrosion.

## 7.6. Relevance for the industry

For the implementation of the developed approaches to an industrial production various requirements have to be met besides the fulfilment of their actual purpose - the improvement of the laser weldability of high-alloyed Al-Zn alloys. Examples for such requirements are: The approaches should be easy to integrate to an existing production line and also easy to handle. For achieving cost-effectiveness the costs for the purchasing of the required devices and consumables should be as low as possible. Furthermore, the approaches should possess a capability for large-scale production and a certain versatility in application. The latter means that the approach or the employed devices could also be used for different welding tasks in matters of materials and joint configurations.

Although vanadium is improving the laser weldability, the implementation of the first approach to an industrial production process is hardly feasible, since the handling of the foil is laborious. The use of the vanadium foil requires an accurate and reliable positioning during the laser beam welding, in order to achieve a complete melting and dilution in the weld metal. Otherwise a degradation of the mechanical properties has to be anticipated. The fixation of the foil could be realised by laser tack welding as a preparatory measure. The use of a V-containing aluminium filler wire would simplify the handling, since welding filler wires are widely used in the industry. For realising the beneficial effect, the vanadium content in the wire has to be high enough. Due to the high strength of vanadium, the processing of such a wire is expected to be very difficult and expensive. Another drawback of vanadium from the industrial point of view are the high expenses for this transition metal as a consumable. Vanadium is far from being scarce, but the extraction and processing is very complex.

The great advantage of the second approach is its ability to be easily implemented to an industrial production process, since the handling of the required laser is as unproblematic and up-scalable as for other commonly used industrial lasers. The high beam quality and thus, the large Rayleigh length as well as the large beam diameter itself allow relatively large positioning tolerances during the laser beam welding process. Moreover, this approach is less prone to process-specific discontinuities, such as the non-melting of the vanadium foil for the first approach. The required laser system could also be easily used for different welding tasks.

Within the framework of a preliminary study, it was shown by the author that the second approach can be utilised for the laser welding of dissimilar tailor welded blanks (TWB). Fig. 7.61 shows an example of such a dissimilar AA5182-AA7075 tailor welded blank. The Al-Mg alloy AA5182, which is widely used in the automotive industry, possess a high formability in contrast to the high-strength Al-Zn alloy AA7075. In this way, it is possible to locally adjust the mechanical properties and finally also to reduce the weight of the final automotive structure. Although the high Mg content of the Al-Mg alloy results in a further reduction of the surface tension of the melt pool the second approach is able to compensate this unfavourable effect on the keyhole stability by using a large laser beam diameter and a low laser beam irradiance for the welding. No weld discontinuities are visible in the radiograph and macrograph of the resulting tailor welded blank. The tensile testing of the tailor welded blanks demonstrated the beneficial characteristics of welded joints. The failure occurred not in the fusion zone or heat affected zone but in the base material of AA5182, which possess a considerable lower tensile strength and a higher ductility. Hence, a comparatively high deformation of the tailor welded blank resulted. This mechanical behaviour could be, for example, exploited for the design of automotive crash structures. On the one hand, the AA5182-side of the tailor welded blank is able to absorb crashing energy by the deformation of the material. On the other hand, the AA7075-side is able to maintain the rigidity of the structure during the crash of a vehicle.

It was shown by Khomenko [126] and the author [127, 128] that the second approach can also

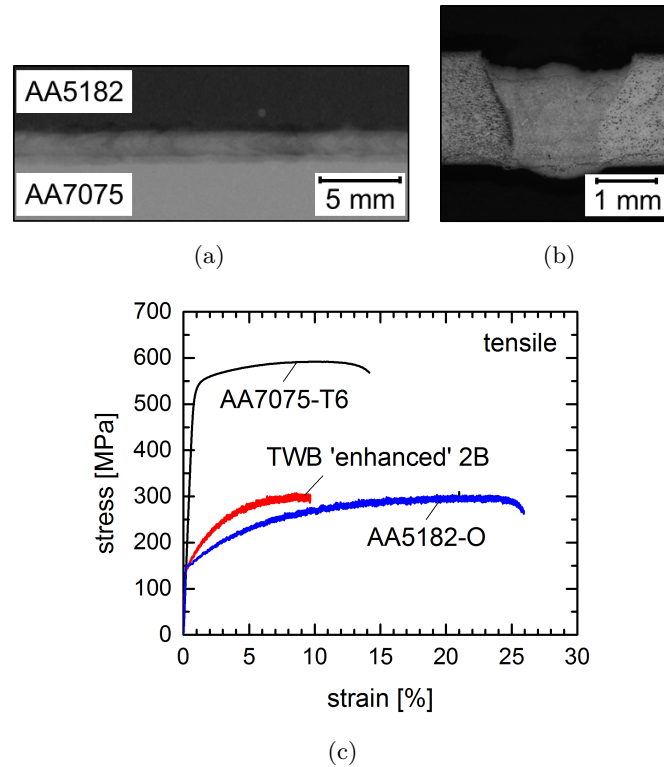


Figure 7.61.: Radiograph (a), macrograph (b) and tensile properties (c) of an AA5182-AA7075 tailor welded blank using the second approach.

be applied for the single-sided welding of T-joints. In general, single-sided welding of T-joints with conventional lasers results in a high weld porosity mainly due to keyhole instabilities caused by insufficient keyhole pressures and an unfavourable temperature field. For this reason, the double-sided welding of T-joints - simultaneously with two lasers or successively with solely one laser - is preferred by the industry, since this was so far the only way to achieve defect-free welds. But this is generally associated with a high production effort. The use of a high-power laser with an enlarged beam diameter for the single-sided welding of T-joints stabilizes the keyhole and enables the degassing, as described in the present study for the welding of a butt joints. Fig. 7.62 shows an example of such a single-sided welded dissimilar AA2024-AA7050 T-joint (with filler wire), which possesses no weld discontinuities as well as a beneficial weld seam shape. The low penetration into the skin sheet results in reduced degradation of the skin material and thus in a relatively high deformation of the skin-stringer joint during hoop-stress testing.

These two examples demonstrate the ability of the second approach to be applicable to other aluminium alloys and alloy combinations as well as to other joint configurations. All aluminium alloys - with the exception of high-alloyed Al-Zn alloys - are assumed to be weldable. Using a large laser beam in conjunction with a low beam irradiance is assumed not to have any negative effect on the weldability of these alloys. In case of aluminium alloys with a high cracking sensitivity, as for example for the Al-Cu alloys, the adjustment of laser welding parameters and/or the use of an appropriate filler wire has to be considered. A restriction of applicability is merely expected for very high sheet thicknesses ( $> 10$  mm). The reason for this lies in the fact that the hydrostatic pressure and thus also the keyhole pressure becomes too high, which finally leads to keyhole instabilities (Section 4.4). In this case, special precautionary measures have to be made, as for example the reduction of the ambient pressure,

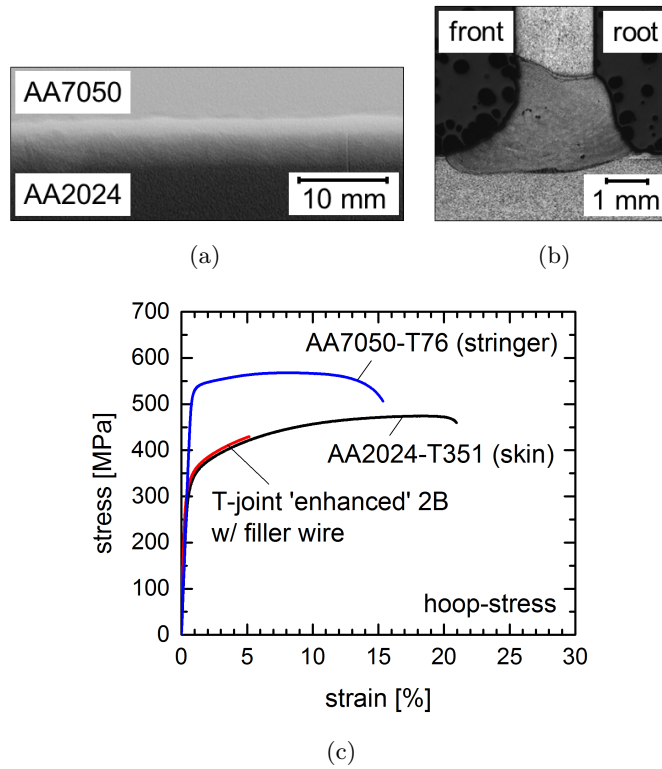


Figure 7.62.: Radiograph (a), macrograph (b) and hoop-stress properties of a single-sided welded AA2024-AA7050 T-joint using the second approach (according to Khomenko [126] and the author [127, 128]).

as described in Section 4.4 and 5.1.

From this it can be concluded that the second approach might be more attractive for the industry as the first approach.

## 8. Conclusions

High-alloyed Al-Zn alloys possess very high strengths in combination with low densities and are therefore predestined for the use in light-weight structures. However, the possibilities for the industrial application of these high-strength alloys are currently limited. The reasons for this disregard by industry lie their severe weldability problems. In the present thesis the problems of welding high-alloyed Al-Zn alloys were surveyed, with special attention to laser beam welding as an efficient method for producing joints. In this literature review it was found that up to now no applicable approaches for solving these laser weldability problems exist.

The aim of the thesis was therefore to specify the theoretical fundamentals of laser weldability with regard to high-alloyed and hard-to-weld Al-Zn alloys. It emerged that the thermophysical parameters describe best the relevant material properties and processes during laser beam welding. By gaining deeper understanding about the laser weldability, it was possible to clarify the reasons for weldability problems and subsequently to develop applicable remedial measures. In this regard, the stabilisation of the keyhole during laser beam welding was of great importance for improving the quality of the resulting welds. Two distinctive approaches were developed, which should positively influence the thermophysical parameters of weld metal. The effectiveness of the approaches for improving the laser weldability was assessed by their application to diverse high-alloyed Al-Zn alloys. The welding behaviour was analysed and the resulting weld characteristics were determined.

The first approach implies the use of a vanadium foil as additional filler material for the laser beam welding of high-alloyed Al-Zn alloys. This approach makes no special demands on the laser used for welding. The effectiveness of vanadium for improving the laser weldability of high-alloyed Al-Zn alloys was successfully verified. The porosity was reduced to a minimum and the outer appearance of the weld seam was improved. The mechanical properties of the fusion zone were improved by using vanadium. Furthermore, no degradation of the overall corrosion behaviour was observed.

The beneficial effect of vanadium can be explained by its thermophysical properties, which enables the manipulation of the material properties of the weld metal. In this regard, the high surface tension and viscosity helps to avoid the formation of excess of penetration and spikes at the root side of the weld. Furthermore, the high surface tension in combination with the low vapour pressure of vanadium as well as its low threshold beam irradiance helps to stabilize the keyhole during welding. The favourable temperature distribution in vanadium during welding - due to its low thermal conductivity and diffusivity - helps to achieve an enlarged keyhole and hence to improve the degassing behaviour.

The second approach implies the use of a laser with an enlarged beam diameter, a high laser power and a high beam quality. And in contrast to the first approach, no special demands on the filler material are made. Its effectiveness for improving the laser weldability of high-alloyed Al-Zn alloys was also successfully verified. Compared to the first approach, no local improvement of the mechanical properties were achieved. However, there was also no degradation of the mechanical properties observed. The corrosion behaviour is expected to be only slightly inferior to the first approach.

The beneficial effect of a laser with an enlarged beam diameter, a high laser power and a high beam quality can be explained by the manipulation of the welding process, in order to

countervail the unfavourable material properties of the weld metal. The welding with such a laser results in the formation of a large keyhole. The stability of the keyhole is improved by the reduction of the capillary pressure - the largest fraction of keyhole pressure, which induces the closing of the keyhole during laser beam welding. Furthermore, the required beam irradiance is decreased for large beam diameters, which also leads to a more stable welding process, although the unfavourable surface tension and viscosity of the weld metal is unchanged. And finally, the degassing conditions may also be improved for larger keyholes.

Although both developed approaches resulted in an improvement of the laser weldability of high-alloyed Al-Zn alloys, only the second approach has the potential to be adopted by the industry. The reasons for this lie in its easy handling, high versatility and the capability for large-scale production.

The present thesis demonstrated the importance of the theoretical fundamentals for the improvement of laser weldability. The most relevant thermophysical properties were identified and their influence on the laser weldability was explained in detail. With the help of this knowledge two distinct approaches were developed whose effectiveness was successfully verified and which might already be implemented in an industrial production line. By this means, the general claim that 'high-alloyed Al-Zn alloys are unweldable' is disproved. However, further investigations have to be conducted to validate their versatility in matters of larger sheet thicknesses and other aluminium alloy systems, such as the Al-Cu-Li aircraft alloys, which also possess certain weldability problems. The obtained knowledge could also be used in future works for the development of further approaches for improving the laser weldability of other metallic structural materials, for example by choosing the appropriate filler material and laser welding system as well as by the adjustment of the welding condition and parameters. By the application of successfully laser welded high-strength Al-Zn alloys in automotive structures, the weight of future vehicles could be further reduced in order to meet the challenges for reducing carbon dioxide emissions.

## 9. Bibliography

- [1] P. Mock. European CO<sub>2</sub> emission performance standards for passenger cars and light commercial vehicles. Technical report, The International Council on Clean Transportation (ICCT), July 2012.
- [2] N. Zacharof, U. Tietge, and P. Mock. CO<sub>2</sub> emissions from new passenger cars in the EU: Car manufacturers performance in 2014. Technical report, The International Council on Clean Transportation (ICCT), July 2015.
- [3] K.H. von Zengen. Aluminium - The light heavyweight in automotive. In *Proceedings of the International Conference on Automotive Technologies (ICAT)*, November 2004.
- [4] European Aluminium Association (EAA). Aluminium in cars - Unlocking the light-weighting potential. Technical report, European Aluminium Association, September 2013.
- [5] D. Uffelmann. Take-off für hochfestes Aluminium im Automobilbau. *ATZextra*, 15(10):22–27, 2010.
- [6] D. van Nieuwerburgh. Aluminium sheet developments for current and future BIW concepts. In *Aluminium Experience Day*. Aleris Europe, August 2011.
- [7] Ducker Worldwide and European Aluminium Association (EAA). Aluminium penetration in cars - Final report. Technical report, Ducker Worldwide and European Aluminium Association, March 2012.
- [8] European Aluminium Association (EAA). CO<sub>2</sub> and Road Transport - Position and messages of the European aluminium industry. Communication from the European Commission on reducing CO<sub>2</sub> emission from cars, July 2007.
- [9] H. Wallentowitz, K.H. von Zengen, T. Parr, R. Wohlecker, and D. Wynands. Leichtbaupotenzial eines aluminium-intensiven Fahrzeugs. *ATZ Worldwide*, 105(3):278–285, 2003.
- [10] J. Hirsch. Recent development in aluminium for automotive applications. *Transactions of Nonferrous Metals Society of China*, 24(7):1995–2002, 2014.
- [11] T. Ma. *Weldability of Al-Zn-Mg alloys*. PhD thesis, Delft University of Technology, 1997.
- [12] G. Verhaeghe. *Achieving aerospace standard porosity levels when welding thin and thick-section aluminium using fibre-delivered lasers*. PhD thesis, University of Warwick, 2008.
- [13] W. Zhou. Problems in welding high-strength aluminium alloys. *Singapore Welding Society Newsletter*, September 1999.
- [14] J.K. Larsson. Laser development at Volvo. *Industrial Laser Solutions for Manufacturing*, 28(2), 2013.

- [15] M. Spöttl and H. Mohrbacher. A review of laser welding technology for mass production of tailored blanks. In *Proceedings of the 1st International Symposium on Automobile Steel*, volume 382, 2009.
- [16] H. Nielsen, W. Hufnagel, and G. Ganoulis. *Aluminium-Taschenbuch*. Aluminium-Verlag GmbH, Düsseldorf, 13th edition, 1974.
- [17] L.F. Mondolfo. *Aluminium alloys: Structure and properties*. Butterworth, London, 1976.
- [18] J.R. Davis. *Aluminum and aluminum alloys*, volume 4. ASM International, Materials Park, 1996.
- [19] The Aluminum Association. International alloy designation and chemical composition limits for wrought aluminum and wrought aluminum alloys. Technical report, The Aluminum Association, Washington D.C., 2015.
- [20] A. Romeyn. Welding Al-Zn-Mg (7xxx series) alloys - A literature review (MRL-R-888). Technical report, Department of Defence, Materials Research Laboratories, Australia, 1983.
- [21] M.J. Starink and S.C. Wang. A model for the yield strength of overaged Al-Zn-Mg-Cu alloys. *Acta Materialia*, 51(17):5131–5150, 2003.
- [22] G.E. Tooten and S. MacEnzie, editors. *Handbook of aluminium: Physical Metallurgy and Process*, volume 1. CRC Press, Boca Raton, 2003.
- [23] I.N. Fridlyander. High-strength aluminium alloys with zinc, magnesium, and copper. *Metal Science and Heat Treatment*, 45(9):341–343, 2003.
- [24] H. Liang, S.L. Chen, and Y.A. Chang. A thermodynamic description of the Al-Mg-Zn system. *Metallurgical and Materials Transactions A*, 28A:1725–1734, 1997.
- [25] Deutsches Institut für Normung (DIN). DIN EN 515:1993: Aluminium and aluminium alloys - wrought products - temper designations. Technical report, Deutsches Institut für Normung, 1993.
- [26] A.F. Oliveira, M.C. de Barros, K.R. Cardos, and D.N. Travessa. The effect of RRA on the strength and SCC resistance on AA7050 and AA7150 aluminium alloys. *Materials Science and Engineering A*, 379:321–326, 2004.
- [27] H. Chandler, editor. *Heat treater's guide: Practices and procedures for nonferrous alloys*. ASM International, Materials Park, 1996.
- [28] R.P. Martukanitz. Selection and weldability of heat-treatable aluminum alloys. In *ASM Handbook*, volume 6. ASM International, Materials Park, 10<sup>th</sup> edition, 1993.
- [29] Y.L. Wu, F.H.S. Froes, C. Li, and A. Alvares. Microalloying of Sc, and Ni and Ce in an advanced Al-Zn-Mg-Cu alloy. *Metallurgical and Materials Transactions A*, 30(4):1017–1024, 1999.
- [30] RSP Technology. RS alloys - High strength. <http://www.rsp-technology.com>, downloaded on 10.07.2015.

- 
- [31] G.M. Scamans, N. Birbilis, and R.G. Buchheit. Corrosion of aluminum and its alloys. In *Shreir's Corrosion - Corrosion and Degradation of Engineering Materials*, volume 3. Elsevier, Amsterdam, 1st edition, 2009.
- [32] J.R. Davis. Corrosion of nonferrous alloy weldments. In *Corrosion of Weldments*. ASM International, Materials Park, 1st edition, 2006.
- [33] J.G. Kaufman. Corrosion of aluminum and aluminium alloys. In *ASM Handbook*, volume 13B, pages 95–124. ASM International, Materials Park, 2005.
- [34] M. Olabode. *Weldability of high strength aluminium alloys*. PhD thesis, University of Technology Lappeenranta, 2015.
- [35] M. Olabode, P. Kah, E. Hiltunen, and J. Martikainen. Effect of Al<sub>2</sub>O<sub>3</sub> film on the mechanical properties of a welded high-strength (AW 7020) aluminium alloy. *Proceedings of the Institution of Mechanical Engineers, Part B: Journal of Engineering Manufacture*, pages 1–10, 2015.
- [36] C.G. Rhodes, M.W. Mahoney, W. H. Bingel, R.A. Spurling, and C.C. Bampton. Effect of friction stir welding on the microstructure of 7075 aluminium. *Scripta Materialia*, 36(1):69–75, 1997.
- [37] M.W. Mahoney, C.G. Rhodes, C.G. Flintoff, W. H. Bingel, and R.A. Spurling. Properties of friction-stir-welded 7075 T651 aluminium. *Metallurgical and Materials Transactions A*, 29(7):1955–1964, 1998.
- [38] M. Dumont, A. Steuwer, A. Deschamps, M. Peel, and P.J. Withers. Microstructure mapping in friction stir welds of 7449 aluminium alloy using SAXS. *Acta Materialia*, 54(18):4793–4801, 2006.
- [39] N. Kamp, A. Sullivan, and J.D. Robson. Modelling of friction stir welding of 7xxx aluminium alloys. *Materials Science and Engineering A*, 466(1):246–255, 2007.
- [40] G. Çam and M. Koçak. Microstructural and mechanical characterization of electron beam welded Al-alloy 7020. *Journal of Material Science*, 42(17):7154–7161, 2007.
- [41] A. Deschamps, S. Ringeval, G. Texier, and L. Delfaut-Durut. Quantitative characterization of the microstructure of an electron-beam welded medium strength Al-Zn-Mg alloy. *Material Science and Engineering A*, 571(1):361–368, 2009.
- [42] Y. Arata, M. Ohsumi, and Y. Hayakawa. Electron beam welding of high strength aluminum alloy (Report 1). *Transactions of Joining and Welding Research Institute (JWRI)*, 5(1):19–25, 1976.
- [43] J. Koy and U. Derudi. Elektronenstrahlschweißen einer AlZnMgCu-Legierung und deren mechanische Eigenschaften. In *Vorträge und Posterbeiträge der 3. Internationalen Konferenz Strahltechnik*, pages 95–99, Karlsruhe, March 1991. Deutscher Verband für Schweißen und verwandte Verfahren (DVS).
- [44] U. Krüger. Beam welding processes of aluminium. Technical Report Training in Aluminium Application Technology (TALAT) Lecture 4300, European Aluminium Association (EAA), 1994.
- [45] European Aluminium Association (EAA). Joining - 4. Beam Welding. The Aluminium Automotive Manual, European Aluminium Association, 2015.

- [46] C.M. Allen, G. Verhaeghe, P.A. Hilton, C.P. Heason, and P.B. Prangnell. Laser and hybrid laser-MIG welding of 6.35 and 12.7 mm thick aluminium aerospace alloy. *Material Science Forum*, 519:1139–1144, 2006.
- [47] S. Katayama, H. Nagayama, M. Mizutani, and Y. Kawahito. Fibre laser welding of aluminium alloys. *Welding International*, 23(10):744–752, 2009.
- [48] L. Zhang, X. Li, Z. Nie, H. Huang, and J. Sun. Microstructure and mechanical properties of a new Al-Zn-Mg-Cu alloy joints welded by laser beam. *Materials and Design*, 83:451–458, 2015.
- [49] International Organization for Standardization (ISO). ISO/TR 581:2005(E): Weldability - Metallic materials - General principles. Technical report, International Organization for Standardization, 2005.
- [50] J.F. Lancaster, editor. *The physics of welding*. Pergamon Press, Oxford, 2<sup>nd</sup> edition, 1986. International Institute of Welding (IIW).
- [51] E. Beyer. *Schweißen mit Laser - Grundlagen*. Laser in der Technik und Forschung. Springer, Berlin, 1995.
- [52] E. Kannatey-Asibu. *Principles of laser materials processing*. John Wiley and Sons, Hoboken, 2009.
- [53] H. Sakamoto, K. Shibata, and F. Dausinger. Laser welding of different aluminium alloys. In *Proceedings of the European Conference of Laser Treatment of Materials (ECLAT)*, pages 125–130, Göttingen, October 1992.
- [54] H. Hügel. *Strahlwerkzeug Laser: Eine Einführung*. Teubner Studienbücher Maschinenbau. Teubner, Stuttgart, 1992.
- [55] J. Rapp, C. Glumann, F. Dausinger, and H. Hügel. The effect of magnesium evaporation in laser welding of aluminium alloys. In *Proceedings of the International Conference on Welding and Melting by Electron and Laser Beams*, pages 275–282, La Baule, June 1993.
- [56] J. Rapp, M. Beck, F. Dausinger, and H. Hügel. Fundamental approach to the laser weldability. In *Proceedings of the European Conference of Laser Treatment of Materials (ECLAT)*, pages 313–325, Bremen, September 1994.
- [57] J. Rapp. *Laserschweißbeignung von Aluminiumwerkstoffen für Anwendungen im Leichtbau*. Laser in der Materialbearbeitung: Forschungsberichte des IFSW. Teubner, Stuttgart, 1996.
- [58] K.H. Leong, H.K. Geyer, K.R. Sabo, and P.G. Sanders. Threshold laser beam irradiances for melting and welding. *Journal of Laser Applications*, 9(5):227–231, 1997.
- [59] K.H. Leong and H.K. Geyer. Laser beam welding of any metal. In *Proceedings of the International Congress on Applications of Lasers and Electro-Optics (ICALEO)*, pages F-243–251, Orlando, November 1998.
- [60] C. Ho, R.P. Powell, and P.E. Liley. Thermal conductivity of the elements. *Journal of Physical and Chemical Reference Data*, 1(2):279–421, 1972.
- [61] C.B. Alcock, V.P. Itkin, and M.K. Horrigan. Vapour pressure equations for the metallic elements 298-2500K. *Canadian Metallurgical Quarterly*, 23(3):309–313, 1984.

- 
- [62] P.F. Paradis, T. Ishikawa, and N. Koike. Thermophysical properties of molten yttrium measured by non-contact techniques. *Microgravity Science and Technology*, 21(1-2):113–118, 2009.
- [63] J.T. Okada, T. Ishikawa, Y. Watanabe, and P.F. Paradis. Surface tension and viscosity of molten vanadium measured with an electrostatic levitation furnace. *The Journal of Chemical Thermodynamics*, 42(7):856–859, 2010.
- [64] W.M. Haynes, editor. *CRC Handbook of chemistry and physics*. CRC Press, Boca Raton, 93<sup>rd</sup> edition, 2012.
- [65] M. Satake and Y. Mido, editors. *Chemistry of transition metals*. Discovery Publishing House, New Dehli, 2010.
- [66] F. Dausinger. *Strahlwerkzeug Laser: Einkopplung und Prozeßeffektivität*. PhD thesis, University of Stuttgart, 1994.
- [67] Y. Arata, N. Abe, and T. Oda. Beam hole behavior during laser beam welding. In *International Congress on Application of Lasers and Electro-Optics (ICALEO)*, pages 59–66, Los Angeles, November 1984. Laser Insitute of America (LIA).
- [68] M. Gao, C. Chen, M. Hu, L. Guo, Z. Wang, and X. Zeng. Characteristics of plasma plume in fibre laser welding of aluminum alloy. *Applied Surface Science*, 326:181–186, 2015.
- [69] J. Wang, C. Wang, X. Meng, X. Hu, Y. Yu, and S. Yu. Study on the periodic oscillation of plasma/vapour induced during high power fibre laser penetration welding. *Optics and Laser Technology*, 44:67–70, 2012.
- [70] Y. Luo, X. Tang, F. Lu, Q. Chen, and H. Cui. Effect of subatmospheric pressure on plasma plume in fiber laser welding. *Journal of Materials Processing Technology*, 215:219–224, 2015.
- [71] J.E. Hatch, editor. *Aluminium: Properties and physical metallurgy*. ASM International, Materials Park, 1984.
- [72] T. Iida and R.I.L. Gurthie. *The physical properties of liquid metals*. Oxford University Press, Oxford, 1988.
- [73] L. Quintino, R. Miranda, U. Dilthey, D. Iordachescu, M. Banasik, and S. Stano. Laser welding of structural aluminium. In *Structural Connections for Lightweight Metallic Structures*, volume 8 of *Advanced Structured Materials*, pages 33–57. Springer Verlag, Berlin, 2012.
- [74] G. Guizzetti and A. Piaggi. Vanadium (V). In E.D. Palik, editor, *Handbook of Optical Constants of Solids 2*, pages 477–485. Academic Press, New York, 1st edition, 1998.
- [75] Y. Kawahito, N. Matsumoto, Y. Abe, and S. Katayama. Relationship of laser absorption to keyhole behavior in high power fibre laser welding of stainless steel and aluminium alloy. *Journal of Materials Processing Technology*, 211:1563–1568, 2011.
- [76] C.E. Cross. On the origin of weld solidification cracking. In T. Böllinghaus and H. Herold, editors, *Hot Cracking Phenomena in Welds II*, pages 3–18. Springer, Berlin, 2005.

- [77] N. Coniglio. *Aluminium alloy weldability: Identification of weld solidification cracking mechanisms through novel experimental technique and model development*. PhD thesis, Bundesanstalt für Materialforschung (BAM), 2008.
- [78] N. Coniglio and C.E. Cross. Weld parameter and minor element effects on solidification crack initiation in aluminum. In T. Böllinghaus and H. Herold, editors, *Hot Cracking Phenomena in Welds II*, pages 277–310. Springer, Berlin, 2005.
- [79] P.N. Anyalebechi. Analysis of the effects of alloying elements on hydrogen solubility in liquid aluminium alloys. *Scripta Metallurgica et Materialia*, 33(8):1209–1216, 1995.
- [80] International Organization for Standardization (ISO). ISO 6520-1:2007: Welding and allied processes - Classification of geometric imperfections in metallic materials - Part 1: Fusion welding. Technical report, International Organization for Standardization, 2007.
- [81] International Organization for Standardization (ISO). ISO 13919-2:2001: Welding: Electron and laser beam welded joints - Guidance on quality levels for imperfections - Part 2: Aluminium and its alloys. Technical report, International Organization for Standardization, 2001.
- [82] G.V. Crowe. *An introduction to nondestructive testing*. The American Society for Nondestructive Testing Inc. (ASNT), Columbus, 2009.
- [83] A. Trautmann and M.F. Zaeh. Laser bifocal hybrid welding of aluminium. *Advanced Material Research*, 10:65–78, 2006.
- [84] M.R. Kronthaler, S. Braunreuther, and M.F. Zaeh. Bifocal hybrid laser welding - More than a superposition of two processes. *Physics Procedia*, 12:208–214, 2011.
- [85] K.S. Hansen, M. Kristiansen, and O. Olsen. Beam shaping to control of weldpool size in width and depth. In *Proceedings of the International Conference on Photonic Technologies (LANE)*, volume 56, pages 467–476, Fürth, September 2014.
- [86] S. Katayama, Y. Kobayashi, N. Seto, M. Mizutani, and A. Matsunawa. Effect of vacuum on penetration and defects in laser welding. In *Proceedings of the International Congress on Applications of Lasers and Electro-Optics (ICALEO)*, pages 612–629, Orlando, October 2000.
- [87] C. Börner, K. Dilger, V. Rominger, T. Harrer, T. Krüssel, and T. Löwer. Influence of ambient pressure on spattering and weld seam quality in laser beam welding with the solid-state laser. In *Proceedings of the International Congress on Applications of Lasers and Electro-Optics (ICALEO)*, pages 612–629, Orlando, October 2011.
- [88] C. Börner, T. Krüssel, and K. Dilger. Process characteristics of laser beam welding at reduced ambient pressure. In *Proceedings of the Conference on High-Power Laser Materials Processing (SPIE 8603)*, pages 86030M1–13, San Francisco, February 2013.
- [89] A. Youhei, K. Yousuke, N. Hiroshi, N. Koji, M. Masami, and K. Seiji. Effect of reduced pressure atmosphere on weld geometry in partial penetration laser welding of stainless steel and aluminium alloy with high power and high brightness laser. *Science and Technology of Welding and Joining*, 19(4):324–332, 2014.

- 
- [90] U. Resigen, S. Olschok, S. Jakobs, and M. Mücke. Welding with laser beam in vacuum - Close-to-production test series for the vehicle industry. *Laser Technik Journal*, 2:42–46, April 2015.
- [91] A. Schneider, A. Gumenyuk, and M. Rethmeier. Mobile vacuum in pocket format. *Lasertechnik Journal*, 4:43–46, 2015.
- [92] S. Riekehr, H. Iwan, R. Dinse, V. Ventzke, and P. Haack (Helmholtz-Zentrum Geesthacht Zentrum für Material- und Küstenforschung GmbH). Process for joining workpieces made of zinc-containing aluminium alloys by laser beam welding. Patent EP20120162865, October 2013.
- [93] S. Riekehr, H. Iwan, R. Dinse, V. Ventzke, and P. Haack (Helmholtz-Zentrum Geesthacht Zentrum für Material- und Küstenforschung GmbH). Process for joining workpieces made of zinc-containing aluminium alloys by laser beam welding. Patent US 9089929 B2, July 2015.
- [94] M. Pastor, H. Zhao, R.P. Martukanitz, and T. Debroy. Porosity, underfill and magnesium loss during continuous wave Nd:YAG laser welding of thin plates of aluminium alloys 5182 and 5754. *Welding Journal*, 78(6):207–s–216–s, 1999.
- [95] M. Pastor, H. Zhao, and T. Debroy. Pore formation during continuous wave Nd:YAG laser welding of aluminium for automotive applications. *Welding International*, 15(4):275–281, 2001.
- [96] E. Stiles. Fibre lasers: The flexible tool for high power laser welding. In *International Welding Technologies Conference*. American Welding Society (AWS), June 2010.
- [97] R. Poprawe. *Lasertechnik für die Fertigung - Grundlagen, Perspektive und Beispiele für den innovativen Ingenieur*. Springer, Berlin, 2005.
- [98] L. Green. Monitoring laser beam performance. *The Fabricator.com*, February 2001.
- [99] A. Morris. Aluminium alloys for aerospace. *Materials World*, 6(7):407–408, 1998.
- [100] Gesellschaft für Schweißtechnik International mbH (GSI). Internationaler Schweißfachingenieurlehrgang nach Richtlinie DVS-IIW 1170. Technical report, Gesellschaft für Schweißtechnik International mbH (GSI), 2009.
- [101] International Organization for Standardization (ISO). EN ISO 17636-1:2013: Non-destructive testing of welds - Radiographic testing - Part 1: X- and gamma-ray techniques with film. Technical report, International Organization for Standardization, 2013.
- [102] Deutsches Institut für Normung (DIN). DIN EN 14096-2:2003: Non-destructive testing - Qualification of radiographic film digitisation systems - Part 2: Minimum requirements. Technical report, Deutsches Institut für Normung, 2003.
- [103] International Organization for Standardization (ISO). DIN EN ISO 6507-1:2006: Metallic materials - Vickers hardness test - Part 1: Test method. Technical report, International Organization for Standardization, 2006.
- [104] International Organization for Standardization (ISO). ISO 6892-1:2009: Metallic materials - Tensile testing - Part 1: Method of test at room temperature. Technical report, International Organization for Standardization, 2009.

- [105] H. Iwan. Laserstrahlschweißen von hoch-zinkhaltiger Aluminiumlegierung. Master's thesis, Hamburg University of Technology, January 2014.
- [106] Deutsches Institut für Normung (DIN). DIN 50100:1978-02: Testing of materials - continuous vibration test: definitions, symbols, procedure, evaluation. Technical report, Deutsches Institut für Normung, 1978.
- [107] American Society for Testing and Materials (ASTM) International. ASTM E647: Standard test method for measurement of fatigue crack growth rates. Technical report, American Society for Testing and Materials International, 2013.
- [108] International Organization for Standardization (ISO). ISO 69227:2012: Corrosion test in artificial atmospheres - Salt spray tests. Technical report, International Organization for Standardization, 2012.
- [109] International Organization for Standardization (ISO). ISO 8407:2009: Corrosion of metals and alloys - Removal of corrosion products from corrosion test specimens. Technical report, International Organization for Standardization, 2009.
- [110] K. Hummert, R. Schattevoy, M. Broda, M. Knappe, R. Müller, P. Beiss, F. Klubberg, T. Schubert, and T. Weißgärber. Nanostructured high strength aluminium for automotive applications. In *Proceedings of the World Congress on Powder Metallurgy and Particulate Materials*, pages 9–161–171, Washington D.C., June 2008.
- [111] Y.H. Zhao and X.Z. Liao, Z. Jin, R.Z. Valiev, and Y.T. Zhu. Microstructure and mechanical properties of ultrafine grained 7075 Al alloy processed by ECAP and their evolutions during annealing. *Acta Materialia*, 52:4589–4599, 2004.
- [112] G. Salvendy, editor. *Handbook of industrial engineering: Technology and operations management*. John Wiley and Sons, 3<sup>rd</sup> edition, 2001.
- [113] J. Kroos, U. Gratzke, M. Vicanek, and G. Simon. Dynamic behaviour of the keyhole in laser welding. *Journal of Physics D: Applied Physics*, 26(3):481–486, 1993.
- [114] P.S. Wei, K.C. Chuang, J.S. Kou, and T. DebRoy. Mechanisms of spiking and humping in keyhole welding. *IEEE Transactions on Components, Packaging and Manufacturing Technology*, 2(1), March 2012.
- [115] J. Enz, S. Riekehr, V. Ventzke, V. Sotirov, and N. Kashaev. Laser welding of high-strength aluminium alloys for the sheet metal forming process. *Procedia CIRP*, 18:203–208, 2014.
- [116] J. Enz, H. Iwan, S. Riekehr, V. Ventzke, and N. Kashaev. Fracture behavior of a laser beam welded high-strength Al-Zn alloy. *Procedia Materials Science*, 3:1828–1833, 2014.
- [117] J. Enz, S. Riekehr, V. Ventzke, and N. Kashaev. Laser weldability of different Al-Zn alloys and its improvement. *Materials Science Forum*, 828-829:389–394, 2015.
- [118] J. Enz, S. Riekehr, V. Ventzke, N. Huber, and N. Kashaev. Laser weldability of high-strength Al-Zn alloys and its improvement by the use of an appropriate filler material. *Metallurgical and Materials Transactions A*, 2016. Accepted for publication.
- [119] S. Kumar, M. Taxak, N. Krishnamurthy, A.K. Suri, and G.P. Tiwari. Terminal solid solubility of hydrogen in V-Al solid solution. *International Journal of Refractory Metals and Hard Metals*, pages 76–81, 2012.

- 
- [120] G. Groma, E. Kovács-Cstényi, I. Kovács, J. Lendvai, and T. Ungár. The composition of Guinier-Preston zones in Al-Zn-Mg alloys. *Philosophical Magazine A*, 40(5):653–665, 1979.
- [121] J.L. Murray. Al-V (Aluminium-Vanadium). *Bulletin of Alloys Phase Diagrams*, 10(4):351–357, 1989.
- [122] J.G. Kaufman. *Fracture resistance of aluminium alloys: Notch toughness, tear resistance and fracture toughness*. ASM International, Materials Park, May 2001.
- [123] K.-H. Schwalbe. *Bruchmechanik metallischer Werkstoffe*. Carl Hanser Verlag, 1980.
- [124] J. dos Santos, G. Çam, F. Torster, A. Insfran, S. Riekehr, V. Ventzke, and M. Koçak. Properties of power beam welded steels, Al- and Ti-alloys: Significance of strength mismatch. *Welding in the World*, 44(6):42–64, 2000.
- [125] E. Cicală, G. Duffet, H. Andrzejewski, D. Grevey, and S. Ignat. Hot cracking in Al-Mg-Si alloy laser welding - operating parameters and their effects. *Materials Science and Engineering A*, 395:1–9, 2005.
- [126] V. Khomenko. Laser beam welding of dissimilar AA2024/AA7050 T-joint. Master's thesis, Bauman Moscow State Technical University, June 2014.
- [127] J. Enz, V. Khomenko, S. Riekehr, V. Ventzke, N. Huber, and N. Kashaev. Single-sided laser beam welding of a dissimilar AA2024-AA7050 T-joint. *Materials and Design*, 76:110–116, 2015.
- [128] J. Enz, S. Riekehr, V. Ventzke, and N. Kashaev. Single-sided laser beam welding of dissimilar T-joints for the aircraft industry. In *Proceedings of the 26<sup>th</sup> Conference on Advanced Aerospace Materials and Processes*. American Society of Material (ASM), May 2015.
- [129] J.L. Murray. Al-Zn (Aluminium-Zinc). *Bulletin of Alloys Phase Diagrams*, 4(1):55–73, 1983.
- [130] J.L. Murray. A-Mg (Aluminium-Magnesium). *Bulletin of Alloys Phase Diagrams*, 3(1):60–74, 1982.
- [131] J.L. Murray. Al-Cu (Aluminium-Copper). *International Metals Reviews*, 30(1):211–234, 1985.



# A. Appendix

## A.1. Temperature distribution during laser beam welding

In this section the calculation methodology for the temperature distribution during laser beam welding of the sheet material - used in Section 4.3 will be described. Further details concerning the calculation can be found in the work of Beyer [51].

During laser beam welding the laser beam - which represents the heat source  $Q$  - will move with a constant welding speed  $v$  through the sheet material with a thickness  $t_s$ . The coordinate system  $(x,y,z)$  - at which the temperature field is observed - is moving along with the heat source. For the purpose of simplification, the finite laser beam with a power of  $P_l$  is represented by a moving line heat source, which is neglecting the real dimensions of the laser beam. As a result, this is resulting in a constant temperature distribution in thickness direction. By this means, it is possible to simulate a fully penetrating keyhole. Here, the keyhole is bordered by the isothermal line of the vaporisation temperature  $T_v$ , whereas the melt pool is bordered by the isothermal line of the melting temperature  $T_m$ . The simplified model is illustrated in Fig. A.1.

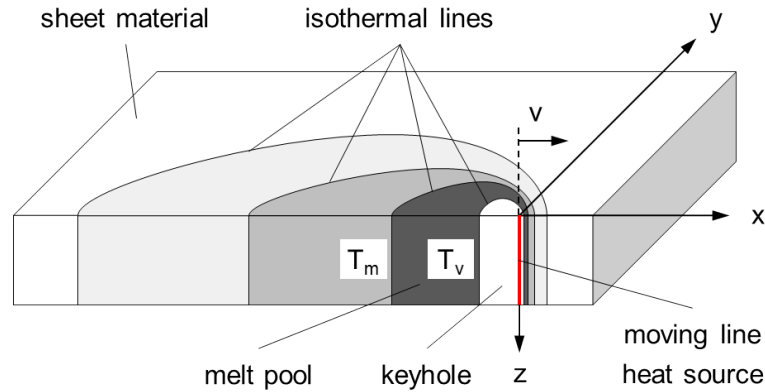


Figure A.1.: Simplified model for the calculation of the temperature distribution during laser beam welding.

The heat of a line source  $Q$  - representing the laser beam - at position  $(x,y)$  and time  $t$  depends on the laser power  $P_l$ , the sheet thickness  $t_s$  and material properties such density  $\rho$  and specific heat capacity  $c_p$ .

$$Q(x, y, z, t) = \frac{P_l}{t_s} \frac{1}{\rho c_p} \delta(x) \delta(y) \tau(t) \quad (\text{A.1})$$

From Eq. A.1 the resulting temperature  $T$  at position  $(x,y)$  and a welding speed of  $v$  for the stationary case  $t \rightarrow \infty$  can be derived, in relation to the ambient temperature  $T_0$ .

$$T(x, y) - T_0 = \frac{P_l}{t_s} \frac{1}{\rho c_p 2\pi\alpha} K_0 \left( \frac{vr}{2\alpha} \right) \exp \left( -\frac{vx}{2\alpha} \right) \quad (\text{A.2})$$

The thermal diffusivity  $\alpha$  of the material can be calculated with the help of the thermal conductivity  $k$ .

$$\alpha = \frac{k}{\rho c_p} \quad (\text{A.3})$$

The modified Bessel function  $K_0$  of the second kind and zero order  $n = 0$  is the solution to Bessel's differential function shown in Eq. A.4.

$$x^2 \ddot{y} + x \dot{y} + (x^2 - n^2)y = 0 \quad (\text{A.4})$$

For the calculation of the temperature the cylindrical coordinates are used, which are defined as followed:

$$\begin{aligned} x &= r \cos \phi \\ y &= r \sin \phi \\ z &= z \\ r &= \sqrt{x^2 + y^2} \end{aligned} \quad (\text{A.5})$$

## A.2. Laser beam parameters

In this section the crucial parameters describing the laser beam are presented (Fig. A.2).

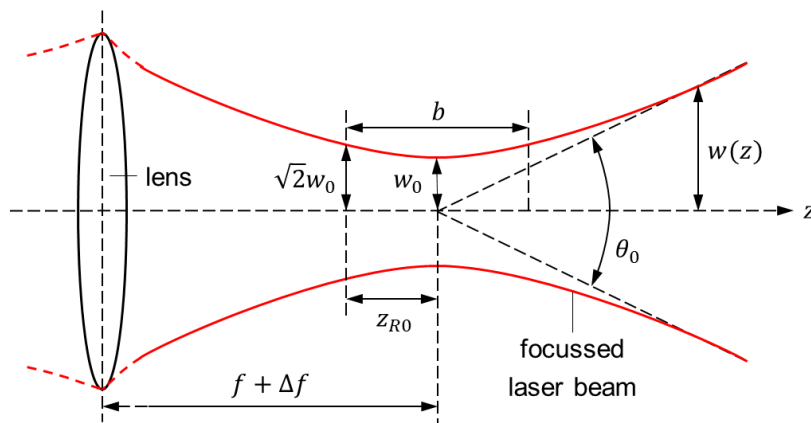


Figure A.2.: Crucial laser beam parameters.

The Rayleigh length  $z_{R0}$  is the distance along the propagation direction  $z$  of the laser beam from the waist - with a radius of  $w_0$  to the position where the area of the cross section is doubled. For an ideal (Gaussian) beam - with a wavelength  $\lambda$  and a total angular spread of  $\Theta_0$  - it is given by:

$$z_{R0} = \frac{\pi w_0^2}{\lambda} \cong \frac{2w_0}{\Theta_0} \quad (\text{A.6})$$

And for a real beam - with a beam quality factor  $M^2$  - it is given by:

$$z_{R0} = \frac{\pi w_0^2}{\lambda M^2} \quad (\text{A.7})$$

Within the confocal parameter  $b$  only marginal changes of the beam diameter and hence also of the power density occur. The advantage of a large confocal parameter is the improved process stability, since small focal changes - e.g. by asperities - do not have a significant effect.

The beam parameter product (BPP) is used for the quantification of the laser beam quality. For an ideal (Gaussian) beam it is given by:

$$BPP = 1 \quad (\text{A.8})$$

And for a real beam it is given by:

$$BPP = \frac{\Theta_0}{2} w_0 = M^2 \frac{\lambda}{\pi} \quad (\text{A.9})$$

### A.3. Laser beam welding parameters

In Table A.1 the used laser beam welding parameters for each welding scenario are specified.

Table A.1.: Laser beam welding parameters used in the present thesis.

scenario	laser type	laser power [kW]	focus position [mm]	welding speed [mm/min]	filler wire feed rate [mm/min]
'worst-case'	Nd:YAG	2.0	0	3500	3500
'variation'	Nd:YAG	2.0	0	3500	3500
'enhanced' 1	Nd:YAG	2.0	0	3500	3500
'enhanced' 2A	Yb fibre	6.0	0	10500	3500
'enhanced' 2B	Yb fibre	3.0	+7.5	3500	–

### A.4. JCPDS identification numbers

In Table A.2 the identification numbers of the used reference diffractograms of the Joint Committee on Reference Powder Diffraction Standards (JCPDS) database are specified.

Table A.2.: JCPDS database identification numbers for the used reference diffractograms.

phase	database ID number
<i>Al</i>	96 – 900 – 8461
<i>Zn</i>	96 – 901 – 1600
<i>Mg</i>	00 – 035 – 0821
<i>MgZn<sub>2</sub></i>	01 – 077 – 1177
<i>V</i>	00 – 022 – 1058
<i>Al<sub>10</sub>V</i>	00 – 029 – 0099

### A.5. Binary phase diagrams

In this section the binary phase diagrams of the three main alloying elements of Al-Zn alloys - namely Zn, Mg and Cu - are presented (see Fig. A.3 to A.5). The typical compositional ranges are marked in the diagrams.

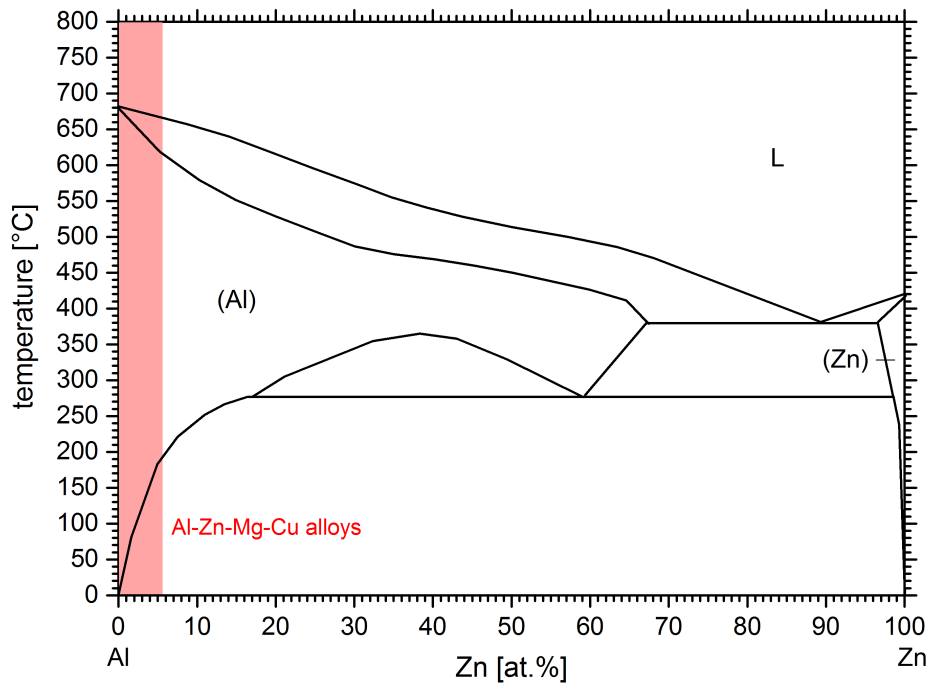


Figure A.3.: Phase diagrams of the binary Al-Zn system (according to Murray [129]).

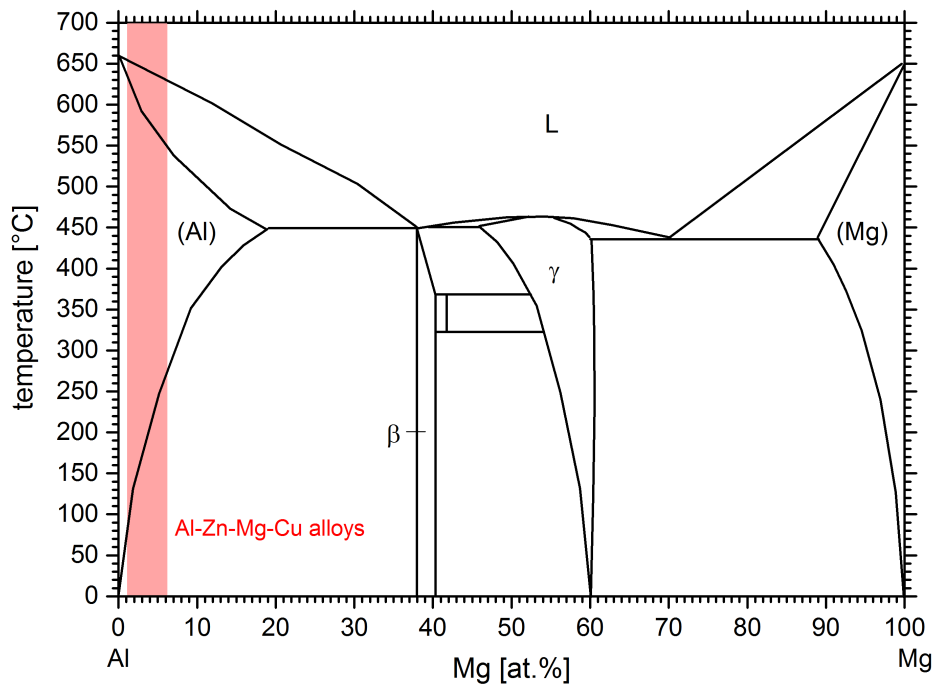


Figure A.4.: Phase diagrams of the binary Al-Mg system (according to Murray [130]).

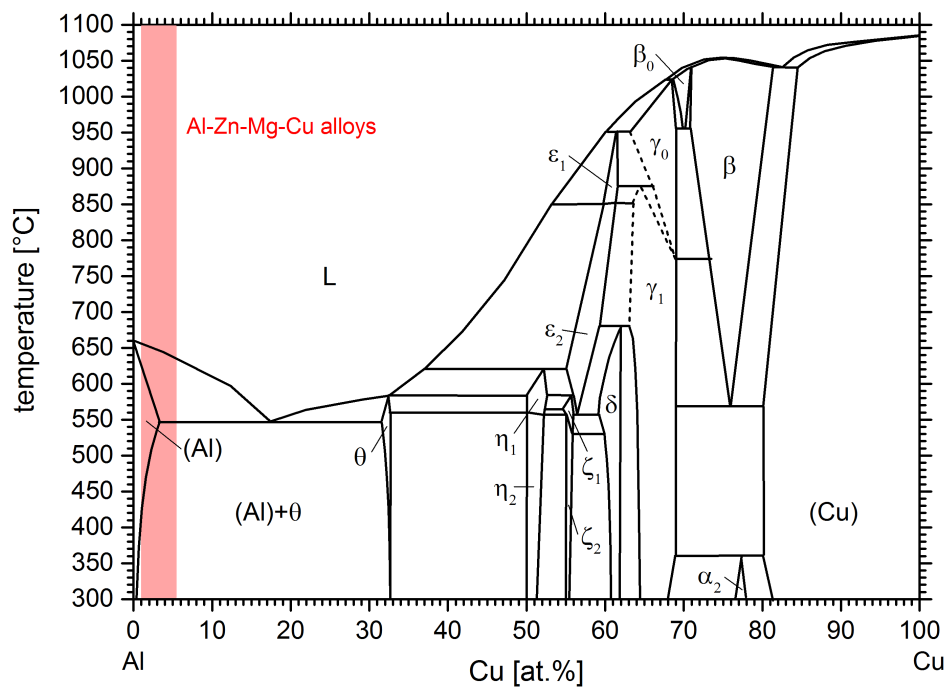


Figure A.5.: Phase diagrams of the binary Al-Cu system (according to Murray [131]).



# Curriculum Vitae

Name	Enz
Vorname	Josephin
Geburtsdatum	21.07.1984
Geburtsort, -land	Berlin, Deutschland
08.1990 – 07.1996	Grundschule am Park in Berlin
08.1996 – 07.2004	Philippe-Cousteau-Oberschule in Berlin Abschluss: Abitur
10.2000 – 03.2012	Hilfskraft bei ENZ Ingenieurbüro für Umweltelektronik & Automatisierung in Berlin
10.2004 – 02.2012	Studium des Maschinenbaus mit Vertiefung Werkstofftechnik an der Technische Universität Hamburg-Harburg in Hamburg Abschluss: Diplom
01.2007 – 05.2007	Grundpraktikum bei Claudius Peters Technologies GmbH in Buxtehude
08.2008 – 08.2009	studentische Hilfskraft am Institut für Logistik und Unternehmensführung der Technischen Universität Hamburg-Harburg in Hamburg
09.2009 – 12.2009	Lehrgang an der Schweißtechnischen Lehr- und Versuchsanstalt Nord gGmbH in Hamburg Abschluss: Internationalen Schweißfachingenieur (DVS-IIW)
02.2010 – 03.2010	Fachpraktikum am GKSS-Forschungszentrum Geesthacht GmbH in Geesthacht
03.2010 – 07.2010	Fachpraktikum bei Blohm + Voss Industries GmbH in Hamburg
03.2012 – 05.2015	Doktorandin am Institut für Werkstoffforschung des Helmholtz-Zentrums Geesthacht GmbH in Geesthacht
08.2012 – 05.2015	Hilfskraft der Öffentlichkeitsarbeit am Helmholtz-Zentrum Geesthacht GmbH in Geesthacht
05.2015 – 12.2016	wissenschaftliche Mitarbeiterin bei der TuTech Innovation GmbH in Hamburg
01.2017 – heute	wissenschaftliche Mitarbeiterin am Institut für Werkstoffforschung des Helmholtz-Zentrums Geesthacht GmbH in Geesthacht